UNIVERSITY OF SOUTHAMPTON

Free and Forced Variability in the North Atlantic Ocean

Alessio Bellucci

Submitted for the degree of Doctor of Philosophy

School of Ocean and Earth Science

March 2004

UNIVERSITY OF SOUTHAMPTON

ABSTRACT

FACULTY OF SCIENCE

SCHOOL OF OCEAN AND EARTH SCIENCE

Doctor of Phylosophy

FREE AND FORCED VARIABILITY IN THE NORTH ATLANTIC OCEAN

by Alessio Bellucci

The internal and forced low frequency variability in an isopycnic coordinate general circulation model of the North Atlantic Ocean is investigated. Numerical experiments performed under climatological buoyancy and momentum fluxes, reveal the existence of a 50 years oscillatory mode, emerging for low levels of internal dissipation and high meridional overturning rates. The oscillation appears to be sustained by a feedback between the poleward propagation of surface thermal anomalies and deep convection in the subpolar gyre. The transition from a steady state to a multidecadal limit cycle solution, occurring for a narrow range of eddy mixing and meridional overturning strengths, suggests the presence of a Hopf bifurcation.

In an additional set of numerical simulations, the ocean response to an idealised North Atlantic Oscillation(NAO)-like windstress is inspected as a function of the atmospheric forcing frequency and the strength of eddy mixing in the ocean. In order to elucidate the relationship between internal and forced variability, the NAO is modulated with two specific timescales, 10 and 50 years, the latter dominating the spectrum of the system's internal variability. Different timescales of atmospheric variability select distinct sea surface temperature (SST) and large scale circulation patterns. When the NAO forcing frequency matches the natural frequency of the ocean, a lagged SST response is excited in the Gulf Stream extension region, which appears to be consistent with the spin-up of the gyre circulation. The thermohaline circulation varies in phase with the NAO and shows a strong sensitivity to the forcing frequency: a dipole mode of the overturning is excited by a 10 years modulation of the NAO, while an enhanced overturning response emerges under a 50 years NAO.

Contents

List of Tables

List of Figures

List of Abbreviations

CVH	*Colin de Verdière and Huck* (1999)
DMS93	*Delworth et al.* (1993)
DWBC	Deep Western Boundary Current
DYNAMO	Dynamics of North Atlantic Models
ECMWF	European Centre for Medium Range Weather Forecasting
EOF	Empirical Orthogonal Function
GFDL	Geophysical Fluid Dynamics Laboratory
GM	Gent and McWilliams (1990) parameterisation
GoC	Gulf of Cadiz
GS	Gulf Stream
IGG	Inter-gyre Gyre
LSW	Labrador Sea Water
MICOM	Miami Isopycnic Coordinate Ocean Model
MO	Mediterranean Outflow
NAC	North Atlantic Current
NADW	North Atlantic Deep Water
NAO	North Atlantic Oscillation
NAOI	North Atlantic Oscillation Index
OGCM	Ocean General Circulation Model
PV	Potential Vorticity
SLP	Sea Level Pressure
SST	Sea Surface Temperature
THC	Thermohaline Circulation
WS91	*Weaver and Sarachik* (1991a,b)

Acknowledgements

The present doctoral research project was funded by a European Community's Marie Curie Grant (Nr ERB4001GT974882) awarded under the Training and Mobility of Researchers programme.

I thank my supervisor, Prof. Kelvin Richards, for granting me guided freedom and allowing me to explore such a fascinating branch of ocean dynamics. I am grateful to Prof. Harry Bryden and Prof. Peter Killworth, respectively chair and member of my advisory panel, for their constructive guidance and encouragement. I wish to express my gratitude to Dr Yanli Jia, for her precious support with MICOM, and Dr Myles Allen and Ms Sarah Murphy, at the Rutherford Appleton Laboratory, for providing the gridded data from the HadAM2b model. Special thanks to Dr Joanna Waniek for her assistance with LaTeX.

A PhD is not only a fundamental stage of a scientist's career. It is also a unique human experience. I am in debt with all the friends I met during my staying at the SOC, for making of this experience an extraordinary and joyful journey. My deepest gratitude to Anita and my family, for sharing the *ups and downs* of a PhD student's life.

Chapter 1

Introduction

1.1 Motivation

A widely accepted picture of the global ocean-atmosphere system identifies the Atlantic Ocean as an essential compartment of the Earth's climate. The Atlantic branch of the thermohaline circulation (THC) - the density-driven component of the ocean circulation - is estimated to be responsible for about 25 % of the total heat transport in the Northern Hemisphere (*Trenberth and Solomon*, 1994). A large fraction of this thermal energy is tranferred to the atmosphere, hence contributing to the anomalously warm air temperatures characterizing the northern North Atlantic and the northwestern Europe. The crucial role played by the ocean large scale circulation in maintaing the current climate in the Atlantic sector, highlights the potentially important climatic consequences that variations in the circulation patterns may have. Proxy and instrumental records show that fluctuations on a broad range of timescales, ranging from millennial (*Weaver*, 1999) to interannual (*Tourre et al.*, 1999), occur in this region of the global ocean. Within the bundle of timescales characterizing the variability of the climate system, the decadal-to-interdecadal timescales occupy a particularly delicate and controversial niche, as over this temporal lengthscale, natural and anthropogenically induced processes are competing factors in shaping the Earth's climate. Recent studies (*Mann et al.*, 1998; *Tourre et al.*, 1999; *Delworth and Mann*, 2000) have shown the existence of an oscillatory pattern of variability characterizing the climate system on a 50-100 years timescale, with a spatial pattern emphasizing the major role played by the Atlantic region. A commonly accepted *null hypothesis* for the oceanic variability is that the atmospheric fluxes act as a white noise on the

ocean, and the large thermal inertia of the upper ocean then contributes to the reddening of the spectrum of the oceanic response (*Hasselmann*, 1976; *Frankignoul and Hasselmann*, 1977). Significant departures from this *climate noise* scenario can be ascribed to a number of causes. Observations and numerical experiments performed with a hierarchy of models point to the instability of the THC as a primary cause of the oceanic decadal and multidecadal fluctuations in the Atlantic (*Rahmstorf*, 1999), although in principle the wind-driven gyre circulation may also play a role, as hypothesized for the North Pacific (*Latif and Barnett*, 1994). Internal variability modes, either stochastically excited and maintained by atmospheric fluxes (*Griffies and Tzipermann*, 1995) or self sustained through non-linear feedbacks (as for the Howard-Malkus loop oscillator; *Welander*, 1967, 1986), are a plausible candidate for the mechanisms behind the long term thermohaline variability.

A major source of oceanic variability on a wide range of timescales, is provided by the intrinsic variability of the troposphere. The leading mode of atmospheric variability in the Atlantic sector, the North Atlantic Oscillation (NAO; *Walker and Bliss*, 1932), displays enhanced variance over narrow frequency bands, with statistically significant spectral peaks centered on quasi-biennial, decadal and multidecadal periods (*Cullen et al.* (2001) and references therein). Basin-scale changes in the atmospheric forcing associated with the NAO induce a local and fast response in the ocean by modulating heat, freshwater and momentum fluxes at the air-sea interface, but there is also growing evidence for a more subtle non-local and delayed response, associated with the adjustment of the slower components of the ocean circulation (*Visbeck et al.*, 2003). More sophisticated dynamical scenarios, invoking an active ocean-atmosphere coupling have also been suggested as a possible source of decadal variability in the extratropics (*Goodman and Marshall*, 1999; *Marshall et al.*, 2001), but convincing observational and modelling evidence of existing feedbacks between the two fluids which may ultimately lead to an ENSO-like mechanism in the extratropical Atlantic region is lacking (*Kushnir et al.*, 2002; *Czaja et al.*, 2003).

The interplay between internal and externally induced ocean variability as a possible source of enhanced variability on specific timescales is an issue which has received relatively little attention. A particularly crucial question is whether preferred timescales exist in the uncoupled ocean system, which may be eventually excited by an atmosphere varying over similar timescales. In other words, if the spectrum of the freely evolving ocean is characterised by intrinsic modes of variability, are these likely to

emerge under an atmospheric forcing matching the characteristic timescale of the ocean internal variability?

Numerical experiments performed with models of varying levels of complexity show that interdecadal oscillations can spontaneously arise within an uncoupled ocean forced with constant surface fluxes of density (*Greatbatch and Zhang*, 1995; *Huck et al.*, 2001). With specific reference to the North Atlantic case, the existence of interdecadal peaks in the NAO spectrum could be instrumental for setting an amplified ocean response over the same timescales. *Visbeck et al.* (1998) and *Krahmann et al.* (2001) investigate the North Atlantic ocean response to an NAO-like wind forcing, as a function of the atmospheric forcing frequency, using an ocean general circulation model (OGCM) coupled to an atmospheric boundary layer. The authors essentially focus on the formation and spreading of surface thermal anomalies, and find enhanced variability in the subpolar gyre for a broadly decadal NAO forcing. However, the relationship between the ocean intrinsic variability and the NAO changes is not investigated. Another unanswered question is whether the dominant variability patterns of the wind-driven gyre circulation and THC are sensitive to the leading timescale of NAO variability. Filling the mentioned gaps in the current knowledge of the ocean-atmosphere interactions occurring in the North Atlantic, is an important step to be performed in order to achieve a better understanding of the observed climate fluctuations in that region.

1.2 Objectives and methodology

The specific objectives of this thesis are outlined below.

• Determining the sensitivity of an OGCM of the North Atlantic ocean to the level of lateral dissipation and the strength of the meridional overtuning circulation, with particular emphasis on the effects on the system's internal variability

Simulations carried out with simplified general circulation models (*Chen and Ghil*, 1995; *te Raa and Dijkstra*, 2002) and planetary geostrophic models (*Huck et al.*, 1999; *Colin de Verdière and Huck*, 1999) show that oscillations with typical interdecadal timescales are likely to occur when critical thresholds are crossed in the parameter

space, suggesting the presence of a Hopf bifurcation. In particular, eddy mixing and the meridional overturning rate (which in turn depends on mixing strength), appear to set the transitions from a stable state to an oscillatory solution. Studying the multi-decadal response of an OGCM to changes in the level of internal mixing while keeping at the same time a reasonable degree of realism in the system representation is a demanding task to be performed under the currently available computational resources. For this reason, exhaustive sensitivity studies are normally carried out with the use of simplified model configurations based on box-shaped domains and highly idealised forcing fields. In the present work the robustness of the above mentioned results will be tested by employing a realistic geometry, approximately 1^{o} resolution OGCM of the North Atlantic, forced with climatological atmospheric fields. The analysis will be carried out in a two-dimensional sub-set of the full parametric space, involving a subgrid scale parameter, representing the unresolved mesoscale baroclinic eddies, and the strength of meridional overturning circulation. The dominant timescales of the internal variability emerging from this sensitivity analysis will be selected to study the ocean response to an (interannually) unsteady atmosphere in an additional set of numerical experiments, illustrated below.

• Determining the response of the extratropical North Atlantic ocean to an NAO-like windstress forcing, under different timescales of the dominant atmospheric variability pattern and varying levels of turbulent mixing in the ocean.

An anomalous NAO-like windstress pattern will be used to perturb the winter windstress climatology, and modulated in time using sinusoidal functions with periods matching the identified timescales of the ocean internal variability.
Finally, the ocean response to an NAO forcing will be assessed for different strengths of the parameterised eddy field. Performing the same experiment under different diffusive regimes will help and clarify whether the ocean response to atmospheric low frequency fluctuations crucially depends on the level of dissipation within the ocean system.
The outlined objectives will be pursued by using an isopycnic coordinate OGCM. Numerical models represent a powerful tool for studying the mechanisms underlying the ocean variability over climatically relevant timescales. Modelling efforts aimed

to improve our uderstanding of the ocean low frequency variability have been mostly carried out within the framework of Cartesian models (i.e., models using geometric height as the vertical coordinate), usually relying on simplified descriptions of subgrid scale effects. Spurious diapycnal fluxes associated with regions of sloping density surfaces represent a well known shortcoming of level models (*Böning et al.*, 1995). In particular, the maximum rate of meridional overturning and northward heat transport in the Atlantic ocean are severely affected by the presence of spurious midlatitude upwelling of deep water, the so called *Veronis effect* (*Veronis*, 1975). Attempts have been made to overcome this problem by introducing more sophisticated eddy transfer parameterisations. *Gent and McWilliams* (1990) (hereafter GM) parameterised the effects of the eddy field on tracers introducing an additional advective term in the tracer transport equation proportional to local gradients of isopycnal layer thickness. The GM parameterisation is based on the assumption that eddies reduce the mean available potential energy by flattening sloping density surfaces, and motion is preferentially adiabatic. A representation of eddy mixing very similar to GM is intrinsically implemented in isopycnic coordinate models (namely, models using density as the vertical coordinate) through a diffusive term in the layer thickness tendency equation. Moreover, isopycnic models do not suffer of the numerical instability problems associated with level models run with low levels of dissipation, and retain their numerical stability under zero thickness diffusivity conditions (*Bleck and Smith*, 1990).
Finally, using a coupled ocean-atmosphere general circulation model, although desirable for the sake of realism, makes it difficult to discern the direction of causality in the air-sea interactions. The strategy, here adopted, of resorting to an uncoupled ocean model is corroborated by the rather scant evidence of an active ocean-atmosphere coupling in the extratropics (*Kushnir et al.*, 2002).
The rest of the thesis is structured as follows. In chapter 2, the observational and modelling evidence of NAO-induced variability in the North Atlantic ocean is surveyed. A gallery of the mechanisms suggested to explain natural extratropical variability, with special focus on the decadal-to-interdecadal range of timescales, is also presented. In chapter 3, the OGCM used to perform the numerical experiments is described in detail, as well as an overview of the general characteristics of isopycnic coordinate models. The sensitivity of model solutions to parameterised mesoscale turbulence and meridional overturning rate (the latter, modulated through a varying Mediterranean outflow) is analysed in chapter 4. A description of the basic states providing the

initial conditions for the NAO-forced experiments is also given. The low frequency variability exhibited by the system under a simple climatological atmospheric forcing, and a possible mechanism behind it, are described in chapter 5. In chapter 6, the forced response of the model ocean to NAO-like fluxes of momentum is described. A final discussion of the main results and concluding remarks are presented in chapter 7.

Chapter 2

Decadal and interdecadal variability in the North Atlantic Ocean: observations and mechanisms

In the present chapter, the obervational evidence of natural decadal and interdecadal variability in the North Atlantic Ocean is reviewed, with specific focus on the role of NAO. Results from dynamical ocean models, forced with NAO-like fluxes are also presented. Finally, a gallery of mechanisms of internal variability (i.e. spontaneously generated within the ocean system) diagnosed with the use of a hierarchy of uncoupled ocean models, is described.

2.1 Forced variability in the North Atlantic Ocean: role of the NAO

The atmospheric variability in the Atlantic sector is dominated by the NAO, a robust feature in the circulation pattern of the atmosphere characterised by a North-South dipole pattern in the sea level pressure (SLP), with centres of action in the Icelandic Low and the Azores High (*Wallace and Gutzler*, 1981). The NAO explains more than 36 % of the variance in winter monthly SLP (*Cayan*, 1992), and its variability index (NAOI), usually measured as the normalised pressure difference between Iceland and Azores, exhibits fluctuations on a broad band of timescales, ranging from interannual

to multidecadal (*Hurrell*, 1995).

The impact of the NAO on the North Atlantic ocean has been analysed in a number of observational and modelling studies. *Bjerknes* (1964) identified two distinct modes of interaction in the Atlantic ocean-atmosphere system: an interannual variability mode, characterised by a local relationship between sea surface temperature (SST) fluctuations and wind-induced sensible and latent heat fluxes, and an interdecadal mode invoking a non local dynamical link between SST anomalies and changes in the ocean circulation. *Deser and Blackmon* (1993) and *Kushnir* (1994), using independent approaches, confirm Bjerknes' results finding that the interdecadal mode of SST variability is associated with an atmospheric circulation pattern resembling the NAO. The corresponding SLP and surface wind patterns are not co-located with respect to the center of action of the SST pattern, placed in the Gulf Stream region. This is suggestive of a non local interaction between the atmosphere and the ocean, involving NAO-induced changes in the large scale ocean circulation.

Molinari et al. (1997) suggest that NAO-driven changes may have affected the upper 400 m temperature fields in the western subtropical North Atlantic, during the 1969-1993 period. The subsurface decadal signal identified by the authors is consistent with the earlier findings of *Levitus* (1989) and *Houghton* (1996), among the others. Observational evidence of NAO-related interannual to interdecadal variability of the North Atlantic gyre circulation is provided by *Curry and McCartney* (2001). The authors define an oceanic analogue of the atmospheric NAO index, through a 2-point baroclinic pressure difference between the subpolar and subtropical gyre. This index (which is also indicative of the magnitude of the geostrophically balanced Gulf Stream(GS)-North Atlantic Current (NAC) system, the oceanic westerlies) is found to significantly covary with the Hurrell's NAO index at 1-2 years lags (the atmosphere leading the ocean). Significant lagged correlation is also found between the NAO and the latitude of the GS northern wall (*Taylor and Stephens*, 1998), the GS displacement lagging the NAO index by approximately two years.

Dickson et al. (1996) relates the coordinated changes recorded in the North Atlantic convective activity to the NAO modulation of the air-sea fluxes. Assuming that the North Atlantic Deep Water (NADW) production process is a major driving factor of the Atlantic density-driven circulation, *Dickson et al.* (1996) suggest that the NAO is a primary forcing of the THC interdecadal variability. Signals of an NAO imprint on the subpolar Labrador Sea Water (LSW) production, with a 2-4 years delay between

the NAOI and the oceanic response, are also revealed by the analysis of *Curry et al.* (1998).

Joyce et al. (2000) inspect the interannual variability of the subtropical mode water, during the 1954-1995 period. The associated potential vorticity (PV) changes appear to be in phase with an NAO index and with the GS position, in contrast with the lagged response found by *Taylor and Stephens* (1998).

Hindcast experiments using time series of surface fluxes data to force state of the art OGCMs (*Häkkinen*, 1999; *Eden and Willebrand*, 2001), show that the bulk of the interannual and decadal variability exhibited by climatically relevant oceanic quantities (meridional heat transport and THC strength, in particular) can be explained by the NAO. *Eden and Jung* (2001) focus on the NAO-induced interdecadal oceanic variability using reconstructed NAO-related surface fluxes for the period 1865-1997. The authors suggest that the NAO multidecadal fluctuations affect the ocean circulation variability through the THC, which is primarily modulated by the NAO-related heat fluxes, whereas momentum and freshwater fluxes play only a minor role.

A fundamental issue underlies the investigation of the relationship linking the NAO to the Atlantic ocean low frequency variability, and that is the constructive and destructive interference between atmospheric and oceanic modes of variability. *Saravanan and McWilliams* (1998) use a one dimensional analytic ocean model coupled to a spatially coherent and stochastic in time atmosphere to inspect the existence of preferred timescales of variability in the coupled system. Within this extremely idealized framework, the authors find that an enhanced reponse is excited in the ocean when the frequency of the atmospheric forcing matches the ocean advection speed divided by the forcing lengthscale, v/L. *Visbeck et al.* (1998) and *Krahmann et al.* (2001) analyze this problem in a more elaborate experimental set-up. *Visbeck et al.* (1998) force an OGCM of the North Atlantic with an NAO-like wind pattern, time varying according to a sine wave law. Experiments performed using NAO periods ranging from interannual to interdecadal timescales, reveal enhanced variability in the subpolar gyre in the 8-24 years interval, whereas the subtropical area exhibits a red spectrum response. *Krahmann et al.* (2001) focus on the mechanisms contributing to the generation and propagation of temperature anomalies along the NAC pathway. The upper ocean thermal response appears to be controlled by two factors: the advection of temperature anomalies along the NAC, occurring in a L/v time length, and the local NAO forcing, varying on a timescale τ. The above mentioned processes

interfere in a constructive or destructive way, depending on the ratio between the related timescales, $R = (L/v)/\tau$. The two processes reinforce each other when $R \sim 1$, leading to constructive interference, whereas cancellation occurs in the $R < 1$ regime.

2.2 Mechanisms of internal variability in the North Atlantic Ocean

Following *Saravanan et al.* (2000), the mechanisms proposed to explain the natural extratropical variability on decadal and multidecadal timescales, based on modeling studies, can be grouped into three broad categories.

- Mechanism A: Damped modes of the uncoupled ocean that are stochastically excited by atmospheric variability (*Griffies and Tzipermann*, 1995; *Saravanan and McWilliams*, 1997, 1998; *Selten et al.*, 1999).
- Mechanism B: Unstable modes of the uncoupled ocean that express themselsves spontaneously (*Weaver and Sarachik*, 1991a,b; *Greatbatch and Zhang*, 1995; *Chen and Ghil*, 1995).
- Mechanism C: Unstable or weakly damped coupled modes of the ocean-atmosphere system (*Latif and Barnett*, 1994; *Goodman and Marshall*, 1999; *Weng and Neelin*, 1998).

The following review focuses on mechanism B, strictly relevant to the present work, and on those coupled model experiments whose detected variability has been suggested to be a mainly oceanic process, with specific focus on the Atlantic basin. The principal mechanisms which have been singled out so far will be shortly described.

Weaver and Sarachik (1991a,b) (hereafter WS91) performed a series of long time integrations using the Bryan-Cox ocean general circulation model (*Cox*, 1984) forced with mixed upper boundary conditions (i.e. a restoring boundary condition for surface temperature, and prescribed fluxes of salinity). The forcing parameters were chosen as typical of the North Atlantic region. A robust feature of all integrations was a decadal oscillation, described as an advective, three-dimensional, high latitude phenomenon. The mechanism proposed by the authors is the following. The presence of a net evaporation region between the subtropical and subpolar gyres in the surface salinity flux is responsible for the generation of positive surface salinity anomalies, which are

advected poleward by the mean flow. Once in the sinking region, they increase the strength of the THC. An intensified THC advects water more rapidly through the net evaporation region, and hence the surface water at the northern boundary, where the deep convection takes place, becomes less saline, slowing down the THC. A weaker meridional overturning produces a longer residence time of the water particles passing through the net evaporation region, which then become more saline, and the cycle starts again. The period of the oscillation is then set by the traveling time of the anomaly along a limited portion of the basin.

Weaver et al. (1991, 1993) analysed the reasons why the numerical experiments performed by *Bryan* (1986) , *Marotzke* (1991) and *Marotzke and Willebrand* (1991) displayed no variability on decadal and interdecadal timescales when compared to the apparently similar simulations of WS91, and found that the discrepancy was caused by the different structure of the surface fresh water fluxes used in the mixed boundary conditions. *Marotzke and Willebrand* (1991), for instance, used a precipitation-evaporation (P-E) forcing field with a meridional gradient weaker than in WS91, and, more importantly, no net evaporation region at midlatitude. This local minimum in the P-E flux was proved to be instrumental in setting the internal variability in the experiments performed by WS91, as already discussed.

Delworth et al. (1993) (hereafter DMS93) provided the first evidence of an interdecadal oscillation in a coupled ocean-atmosphere GCM, using the Geophysical Fluid Dynamics Laboratory (GFDL) coupled model. The irregular oscillation, involving the North Atlantic branch of the THC, had a timescale of 40-50 years, and appeared to be driven by density anomalies in the sinking region of the THC, combined with much smaller density anomalies of opposite sign in the rising region. In spite of the coupled nature of the experiment, DMS93 recognised the variability as a mainly oceanic process, stimulated by random surface buoyancy forcing of heat and water fluxes.

In order to demonstrate the uncoupled character of the oscillation found by DMS93 in the coupled GFDL model, *Greatbatch and Zhang* (1995) performed an ocean-only modelling study using a planetary geostrophic OGCM for a flat-bottomed, 60^o square box of the Northern Hemisphere. With no wind stress, zero salt flux and zonally uniform heat fluxes, they showed that the THC strength was subject to a 50-year regular oscillation, very similar to the one found by DMS93. Including a zonally uniform salt flux yielded a reduced amplitude, 70 years long oscillation. The mechanism proposed

was a negative advective feedback, with high-latitude temperatures controlling the overturning.

Oscillatory behavior was detected by *Huang and Chou* (1994) in a 4^o resolution, single buoyancy variable (constant temperature) version of the Bryan-Cox model, forced by freshwater alone. Using a linear freshwater flux as upper boundary condition, an increase in the forcing amplitude forced the system to evolve from a steady state to a state characterised by periodic oscillations, with frequencies increasing almost linearly with the amplitude of the freshwater flux. The oscillations were also found strongly sensitive to changes in the vertical and horizontal mixing coefficients, and to the model resolution, sometimes switching from a regular periodicity to a chaotic behavior. The period of the salt oscillation was found consistent with the meridional advective time scale.

Chen and Ghil (1995) analysed the decadal, interdecadal and longer term variability in a simplified OGCM of the North Atlantic, using different freshwater flux profiles in a set of mixed boundary condition experiments. When the evaporation minus precipitation flux is positive along the northern boundary, the THC undergoes an interdecadal oscillation, which is produced by a convective-advective feedback mechanism triggered by the high-latitude accumulation of saline water. When the sign of the salinity forcing is reversed (net precipitation in high latitudes, the opposite over the rest of the basin), the system exhibits millennial and decadal-to-interdecadal variability, the latter taking place in the midlatitude upper ocean, where the applied salinity flux is positive. Here destabilization occurs when upper layer waters, due to the constant input of salt at the surface, overlie deep waters which have been warmed by downward diffusion of heat.

Yin and Sarachik (1995) studied the interdecadal thermohaline oscillations exhibited by a single-hemisphere coarse resolution version of the GFDL Modular Ocean Model, under steady forcing, and proposed the following advective-convective mechanism to explain the oscillatory solutions. A strong convective phase in the subpolar region is started by the subsurface advective warming induced by the northeastward currents transporting heat and salt poleward from the subtropical gyre. The vertical homogenization makes the surface water saltier and warmer and the subsurface water colder and fresher. The downward vertical velocity anomaly associated with convection induces a cyclonic flow, through vortex stretching, which advects polar fresh water into the convective region. Surface freshening, progressively weakens convection, which

eventually ceases once the vertical density stratification becomes stable. The cycle repeats itself when the constant subsurface advection of warm water sets conditions favourable to vertical instability. The period of the self-sustained oscillation is then given by the time between two consecutive strong convective phases, which is in turn dependent on the surface freshening and the subsurface heating rate.

Winton (1996) and *Greatbatch and Peterson* (1996) examined the interdecadal variability in the context of the thermohaline overturning adjustment process, associated with frictional boundary waves (the analogue of Kelvin waves in planetary geostrophic ocean models where the time derivative of momentum is neglected). *Winton* (1996) showed that baroclinic Rossby waves based on the β-effect were not essential for the interdecadal oscillations, managing to reproduce these oscillatory solutions on the f-plane. He instead related the interdecadal variability featured by a coarse resolution frictional geostrophic model, to the propagation of boundary-trapped waves, triggered by the impinging of thermal wind currents to weakly stratified coasts. He suggested that the high-latitude weak stratification induced by convection, could strongly impede the Kelvin wave propagation, which would then take place on an interdecadal timescale. *Greatbatch and Peterson* (1996), by alternatively suppressing wave propagation along each of the model boundaries, showed that only the western boundary was crucial to the existence of interdecadal oscillations, which were suggested to be self-sustained by southward propagating boundary waves, perturbing the western boundary current. *Winton* (1996) also pointed out the three-dimensional character of self-sustained decadal scale oscillations showing that the variability does not occur in a two-dimensional frictional model forced with fixed buoyancy fluxes. *Winton* (1997) and *Greatbatch et al.* (1997) investigated the sensitivity of the THC interdecadal mode to bottom topography.

The results of *Winton* (1996) and *Greatbatch and Peterson* (1996) have been revised by *Huck et al.* (1999) and *Colin de Verdière and Huck* (1999) (hereafter CVH), who suggest that PV waves of interdecadal period can play a role in establishing the low frequency variability in a coarse resolution ocean model, under constant surface heat fluxes. These waves can still exist on f-planes whenever a PV gradient is maintained by the mean stratification and circulation. CVH suggest that the baroclinic instability of the western boundary current region, supposed to be active at planetary scales (*Colin de Verdière*, 1986) provides the energy source for the oscillations to be sustained in the face of dissipation.

Delworth and Greatbatch (2000) extended the work of DMS93, forcing the oceanic component of the GFDL coupled model with time series of surface fluxes taken from the coupled model and from a separate extended integration of the only atmospheric component of the coupled model. The authors, after performing several experiments with high- and low-pass filtered heat fluxes, suggest that the variability of the THC detected by DMS93 is driven by the low-frequency portion of the atmospheric flux forcing, without involving any coupled ENSO-like air-sea mode, as previously suggested by *Weaver and Valcke* (1998).

Chapter 3

The Model

The model used to perform the numerical experiments described in the present work is MICOM (Miami Isopycnic Coordinate Ocean Model). MICOM is an isopycnic coordinate primitive equation OGCM, extensively documented in a number of papers (*Bleck et al.*, 1992; *Bleck*, 1998). In this chapter the main chatacteristics of isopycnic coordinate models will be reviewed, with specific focus on MICOM. The model configuration used in the numerical simulations will also be described.

3.1 Isopycnic models

Isopycnic models differ from the traditional Cartesian models (i.e., models adopting the geometric height as vertical coordinate) by the use of potential density ρ as vertical coordinate. The use of an (x,y,ρ) coordinate system is an alternative formulation to the more familiar (x,y,z) frame, and it has strong implications on the way we represent physical processes in the ocean. Cartesian models are solved in a framework where density and depth are dependent and independent variables, respectively. Isopycnic models, on the other hand, solve the equations of motion and tracer transport on constant density surfaces, whose depth changes with time.

A fundamental advantage deriving from the use of isopycnic models is the reduced impact of numerical diffusion on the model solution, when comparison is made with z-coordinate models. A well known Achille's heel of level models is the production of spurious diapycnal fluxes, particularly in regions characterised by steeply sloping density surfaces, due to the rather artificial split of transport terms into horizontal and vertical components. These fluxes have been shown to affect large scale features of the

modelled circulation, such as the meridional overturning and heat transport (*Böning et al.*, 1995). As suggested by *Iselin* (1939) and *Montgomery* (1940), turbulent mixing of tracers in a stably stratified ocean is an essentially adiabatic process, with the eddy-induced spreading of material properties taking place preferentially along isopycnal surfaces, whereas diabatic processes are weaker by several orders of magnitude. The implementation of isopycnal mixing in a Cartesian model, either by resorting to a rotated mixing tensor locally tangent to an isopycnal surface (*Redi*, 1982) or via the introduction of *bolus velocity* terms in the tracer transport equation (*Gent and McWilliams*, 1990), is computationally demanding, and does not completely remove the spurious diapycnal fluxes as the numerical stability of the model still requires the use of a background diffusive term. Isopycnic coordinate models, on the other hand, provide a natural representation of the adiabatic eddy fluxes taking place in a stably stratified fluid. The use of an (x,y,ρ) reference system allows for a more realistic decomposition of the mixing terms into isopycnal and diapycnal components. Numerical diffusion due to truncation errors associated with the advection schemes can only occur along isopycnal sufaces, and can be possibly overshadowed by the isopycnic mixing. Unless specifically parameterised, diapycnal mixing is absent from the system. This allows the strength of diapycnic fluxes and their effects on the model solution to be controlled.

The switch from depth to density as vertical coordinate also represents an improvement with regard to the resolution of the ocean vertical structure. Isopycnic models describe the ocean as a stack of shallow water systems, or in other words homogeneous density layers, whose thickness varies in space and time. As the depth of a layer interface changes in response to water mass formation/dissipation processes, the stratification of the water column is always reproduced within the accuracy of the set of density classes chosen to be represented by the model. This *adjustable* vertical resolution is capable of resolving density structures where it is most needed and overcomes the poor resolution problems inherent in the use of a Cartesian vertical discretization.

As a given water mass, ideally represented by an isopycnal layer, is not necessarily defined over the entire domain due to the presence of water mass sources and sinks, constant density layers have to be allowed to become massless. The calculation of mass flux divergences in the neighbourhood of massless gridpoints represents a major challenge in isopycnal modelling, as the approach to the zero thickness limit may

result in unphysical overshootings, producing negative thickness values. The development of a class of transport schemes designed to conserve the positive-definiteness of the advected properties made it possible to overcome this problem and set the transition from a hybrid, quasi-isopycnic model (*Bleck and Boudra*, 1981), resorting to the Cartesian frame whenever the layer thickness reaches a minimum value, to a purely isopycnic system (*Bleck and Boudra*, 1986). The Flux Corrected Transport scheme (*Zalesak*, 1979), currently implemented in MICOM, uses a low order forward-upstream scheme to advect thickness without jeopardizing the positive-definiteness of the transported field. A higher order advection scheme is then used to correct the diffusive effects introduced in the previous step and regenerate the gradients, without producing new minima or maxima.

Isopycnic coordinate models were also the first to have a free surface, as an alternative to the rigid-lid approximation (*Bryan*, 1969). In MICOM the rigid-lid is replaced by a more efficient split-explicit scheme, based on the mode decomposition of pressure and velocity fields into barotropic and baroclinic components (*Bleck and Smith*, 1990). The mode splitting increases the computational efficiency by allowing the use of different timesteps to advance separately the barotropic and baroclinic equations.

One of the difficulties encountered during the development of ρ-coordinate models was the introduction of a planetary boundary layer at the top of the layered ocean. The addition of a mixed layer, whose density is vertically constant but varies horizontally, allows buoyancy fluxes to take place at the upper boundary. Merging the non-isopycnic mixed layer to the internal isopycnal ocean is problematic, as changes in the upper layer density induced by heat and salinity fluxes at the air-sea interface do not necessarily match the interior density values. In MICOM a bulk mixed layer sub-model based on the vertically integrated turbulent kinetic energy equation (*Kraus and Turner*, 1967) is used to simulate the seasonal entrainment/detrainment cycle (*Bleck et al.*, 1989). During the detrainment phase, the water which is no longer in the mixed layer is temporarily stored into a buffer area (the *fossil* mixed layer). The pumping of the detrained water into the layered ocean, takes place at the end of a vertical redistribution of the thermal energy within the mixed layer, aimed to produce the matching between buoyancies of the newly formed water and an existing coordinate layer. The representation of the mixed layer through an *integral model* of the Kraus-Turner type, although successful under many aspects, is not immune to undesired side effects. The absence of vertical resolution in the uppermost layer

causes unrealistic vertical homogeneity of both momentum and tracers over large depths, particularly in the subpolar regions where the mixed layer deepening reaches its maximum. This problem is intrinsic to purely isopycnic models, and cannot be overcome unless a more flexible vertical coordinate is introduced. The need for a better representation of the mixed layer vertical structure is one of the reasons which led to the development of HYCOM (Hybrid Coordinate Ocean Model; *Bleck*, 2002), a hybrid-coordinate general circulation model adopting the Cartesian framework in the upper ocean, the isopycnic reference system in the internal stratified ocean and a σ-coordinate in the coastal areas.

The preservation of water masses characteristics over century timescales is a peculiarity of isopyncal models. This feature makes them the most appropriate tool to investigate the low frequency ocean variability. As this is one of the main subjects of the present work, the use of MICOM as the numerical model was a natural choice.

3.2 Model description

The model adopted for the present work is MICOM, in the particular configuration of DYNAMO (Dynamics of North Atlantic Models) inter-comparison project (*DYNAMO Group*, 1997). The essential characteristics of the model are detailed in *Bleck et al.* (1992). In the following sections the dynamic equations, along with the details of the model configuration, will be outlined.

3.2.1 The equations of motion

The model prognostic equations describe the horizontal velocity vector, mass continuity and the transport of a buoyancy variable on surfaces of constant potential density referenced to the surface (σ_0). In order to extend the applicability of the equations to the non-isopycnic mixed layer, a generalized vertical coordinate s is used.

The equations of momentum, mass conservation and buoyancy transport in the (x,y,s) space, are respectively:

$$\frac{\partial \mathbf{v}}{\partial t_s} + \nabla_s \frac{\mathbf{v}^2}{2} + (\zeta + f)\mathbf{k} \times \mathbf{u} + \left(\dot{s}\frac{\partial p}{\partial s}\right)\frac{\partial \mathbf{v}}{\partial p} + \nabla_s M = -g\frac{\partial \tau}{\partial p} + \left(\frac{\partial p}{\partial s}\right)^{-1} \nabla_s \cdot \left(\nu \frac{\partial p}{\partial s}\nabla_s \mathbf{v}\right) \tag{3.1}$$

$$\frac{\partial}{\partial t_s}\left(\frac{\partial p}{\partial s}\right) + \nabla_s \cdot \left(\mathbf{v}\frac{\partial p}{\partial s}\right) + \frac{\partial}{\partial s}\left(\dot{s}\frac{\partial p}{\partial s}\right) = 0 \tag{3.2}$$

$$\frac{\partial}{\partial t_s}\left(\frac{\partial p}{\partial s}\theta\right) + \nabla_s \cdot \left(\mathbf{v}\frac{\partial p}{\partial s}\theta\right) + \frac{\partial}{\partial s}\left(\dot{s}\frac{\partial p}{\partial s}\theta\right) = \nabla_s \cdot \left(\kappa\frac{\partial p}{\partial s}\nabla_s\theta\right) + \mathcal{H}_\theta \tag{3.3}$$

where $\mathbf{v}=(u,v)$ is the horizontal velocity vector, p is pressure, θ is a generic thermodynamic variable, $\zeta=(\frac{\partial v}{\partial x_s} - \frac{\partial u}{\partial y_s})$ is the relative vorticity, $M = \phi + p\alpha$ is the Montgomery potential, $\phi = gz$ is the geopotential, $\alpha = \rho^{-1}$ is the specific volume, f is the Coriolis parameter, $\mathbf{k}$ is the vertical unit vector, ν and κ are the isopycnic viscosity and diffusivity, respectively, and τ is the wind- and bottom-drag induced horizontal shear stress vector. $\mathcal{H}_\theta$ includes all the diabatic processes acting on the buoyancy variable θ in the layered domain. In the present configuration, the thermodynamic variable is salinity. Potential temperature is inferred from salinity and potential density through the equation of state. The subscript s indicates that partial differentiation is carried out over constant-s surfaces. The slope of s surfaces introduces metric terms in the equations. These terms are removed by applying the convention of measuring distances and velocities in the x,y direction on the projection of coordinate surfaces over the horizontal plane.

Consistent with the description of the ocean as a vertical stack of constant density layers, the equations are reformulated in a layer-averaged form. After integration over a layer bounded by two coordinate surfaces s_{bot},s_{top}, the mass conservation equation (3.2) turns into a tendency equation for the layer weight per unit area $\Delta p = p(s_{bot}) - p(s_{top})$:

$$\frac{\partial}{\partial t_s}\Delta p + \nabla_s \cdot (\mathbf{v}\Delta p) + \left(\dot{s}\frac{\partial p}{\partial s}\right)_{bot} - \left(\dot{s}\frac{\partial p}{\partial s}\right)_{top} = 0 \tag{3.4}$$

The term $(\dot{s}\partial p/\partial s)$ represents the interlayer mass flux, taken positive along the downward direction. Fluxes across s-surfaces are prescribed as the entrainment and detrainment at the base of the mixed layer and as diapycnal mixing occurring at the interfaces separating density layers. In (3.4) $\mathbf{v}$ is a layer-averaged quantity. By applying the Reynolds decomposition of velocity and pressure fields into a time mean and a residual component, the nonlinear flux term $\nabla_s \cdot (\mathbf{v}\Delta p)$, after time-averaging, breaks into

$$\overline{\nabla\cdot(\mathbf{v}\Delta p)} = \nabla\cdot(\overline{\mathbf{v}}\overline{\Delta p}) + \nabla\cdot(\overline{\mathbf{v}'\Delta p'})$$

where the overbar indicates the time average and primed variables are the residual time-varying components. The second term on the right hand side, represents the turbulent thickness diffusion, and is parameterised, similar to the subgrid scale fluxes of momentum, as $-\nabla\cdot(\nu\nabla\Delta p)$, where ν is a thickness diffusivity coefficient.

Upon layer-averaging, the momentum equation (3.1) retains its form, except for the shear stress and the lateral mixing terms on the right-hand side, which change into

$$\tfrac{g}{\Delta p}(\tau_{top} - \tau_{bot})$$

and

$$(\Delta p^{-1})\nabla_s\cdot(\nu\Delta p\nabla_s\mathbf{v})$$

respectively. The wind stress is assumed to be zero at the base of the mixed layer. Hence, the Ekman layer is not allowed to become shallower than the mixed layer. A quadratic law for the bottom stress is applied, and a linear profile is assumed so that the stress decreases from $-\rho C_d|\mathbf{v}|\mathbf{v}$ at the sea floor to zero in a ten meter thick bottom boundary layer. The layer-integrated form of (3.3) is:

$$\frac{\partial}{\partial t_s}\theta\Delta p + \nabla_s\cdot(\mathbf{v}\theta\Delta p) + \left(\dot{s}\frac{\partial p}{\partial s}\theta\right)_{bot} - \left(\dot{s}\frac{\partial p}{\partial s}\theta\right)_{top} = \nabla_s\cdot(\nu\Delta p\nabla_s\theta) + \mathcal{H}_\theta \qquad (3.5)$$

Two diagnostic equations complete the system. The hydrostatic equation

$$\frac{\partial M}{\partial\alpha} = p \qquad (3.6)$$

and an equation of state linking salinity to potential temperature and density.

3.2.2 Model configuration

The model domain covers the Atlantic region from approximately 100°W to 20°E and 20°S to 70°N, with closed northern and southern boundaries. The equations, reformulated in finite difference form, are solved on a staggered Arakawa 'C' grid (*Mesinger and Arakawa*, 1976), with an horizontal resolution of $\frac{4}{3}^o$ in longitude and $\frac{4}{3}^o\cos\varphi$ in latitude. The scale factor $\cos\varphi$ yields an isotropic grid (i.e., the grid size in

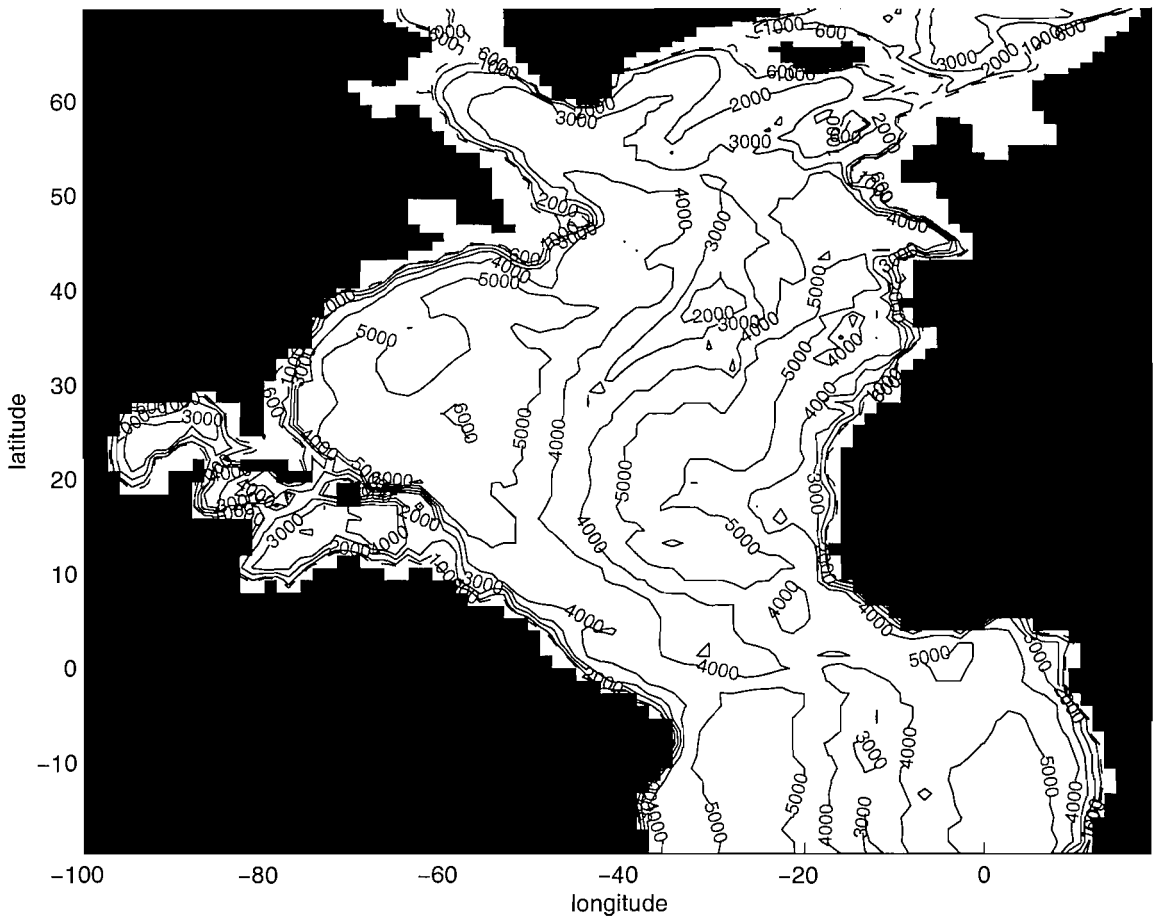

Figure 3.1: Model bathymetry in meters on a longitude-latitude grid. Contours are at 1000-m intervals with the 600-m contour also shown (dashed line).

independent on direction). There are 19 constant density layers in the vertical capped by a Kraus-Turner type mixed layer (*Kraus and Turner*, 1967). This layer is vertically homogeneous but varies in density in the horizontal. The vertical discretization is given in Table 3.1. Bathymetry is provided by the ETOPO5 database from the National Geophysical Data Center. The basin boundaries and topography are shown in figure 3.1.

Except for the numerical experiments performed under an NAO-like wind stress (see chapter 6), the model is forced at the upper boundary with monthly climatological forcing fields for wind stress and heat fluxes, derived from three years of the European Centre for Medium-range Weather Forecasts (ECMWF) analyses (1986-1988). Wind stress is applied using the formulation proposed by *Kondo* (1975). Monthly means of the third power of the friction velocity $u_* = (\frac{|\tau^{\mathbf{w}}|}{\rho})^{1/2}$ (where $\tau^{\mathbf{w}}$ is the wind stress vector), required in the turbulent kinetic energy equation for the mixed layer sub-

Layer	σ_0
1	variable
2	24.70
3	25.28
4	25.77
5	26.18
6	26.52
7	26.80
8	27.03
9	27.22
10	27.38
11	27.52
12	27.64
13	27.74
14	27.82
15	27.88
16	27.92
17	28.00
18	28.06
19	28.09
20	28.12

Table 3.1: Surface-referenced potential density (σ_0) of the layers defining the vertical discretization of the model.

model, have also been determined from 6-hourly ECMWF analyses. The surface heat fluxes are applied through a Haney-type (*Haney*, 1971) boundary condition, stemming from the linearization of the bulk formulae parametrizing surface heat flux components (*Barnier et al.*, 1995):

$$Q_{net}(T_s) = Q_1 + Q_2(T_s{}^{clim} - T_s)$$

where Q_{net} is the net heat flux, T_s is the model surface temperature, $T_s{}^{clim}$ is the climatological sea surface temperature, Q_1 is the climatological net heat flux $Q_{net}(T_s^{clim})$ and $Q_2 = -(\frac{\partial Q_{net}}{\partial T})_{T_s^{clim}}$. The thermal upper boundary condition is reformulated as a relaxation of the model ocean surface temperature toward an apparent air temper-

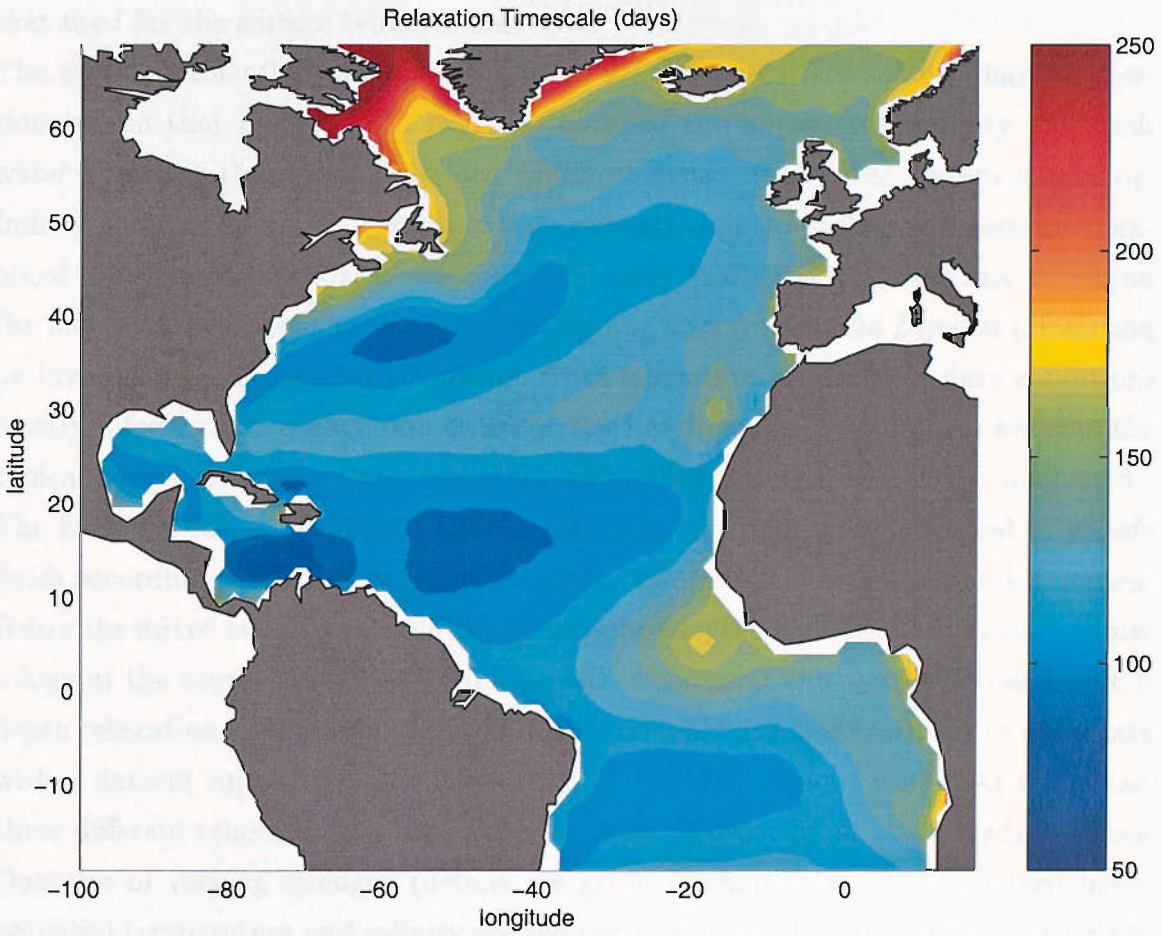

Figure 3.2: Annually averaged distribution of the sea surface temperature relaxation timescale (in days), for a typical mixed layer depth of 100 m.

ature T_a:

$$Q_{net}(T_s) = Q_2(T_a - T_s)$$

where $T_a = T_s^{clim} + \frac{Q_1}{Q_2}$.

The newtonian damping of the sea surface temperature is governed by a relaxation timescale $T_R = (\frac{Q_2}{\rho c_p h})^{-1}$, where c_p is the specific heat of sea water (set equal to 3.99 J/g/^{o}C) and h is the mixed layer depth. Since Q_2 and h vary both in time and horizontally, the implied relaxation timescale will be not constant. In figure 3.2 the annually averaged distribution of T_R is shown, for a typical mixed layer depth of 100 m. The map shows that over most of the model domain, the restoring timescale is, on average, shorter than 150 days.

The fresh water forcing is a relaxation of the model surface salinity to the Levitus climatology (*Levitus*, 1982), with the restoring timescale chosen to be identical to

that used for the surface temperature.
The use of a relaxation boundary condition for the sea surface salinity may be questionable, in that it assumes a feedback between the upper layer salinity and fresh water fluxes at the air-sea interface whose evidence in the real system is lacking. Indeed, a *mixed* boundary condition (i.e., relaxation of sea surface temperature combined with fresh water fluxes) is usually preferred. As the main focus of this work is on the low frequency behavior of the ocean, results from *te Raa and Dijkstra* (2002) can be invoked, suggesting that the switch from relaxation to flux boundary conditions mostly affects the stability properties of the low frequency variability, whereas the typical period and space structure of the variability modes are basically unaffected.
The ECMWF forcing fields and Levitus sea surface salinity were converted to *pseudo fields* according to *Killworth* (1996), in order to obtain the correct monthly means. Below the mixed layer, layer salinity and interface depths are relaxed to Levitus climatology at the southern boundary (full depth), whereas at the northern boundary full depth relaxation applies to an improved hydrographic database merging Levitus data with a dataset supplied by the Kiel group (*DYNAMO Group*, 1997). At Gibraltar, three different relaxation depths have been used, in order to simulate Mediterranean Outflows of varying strength (details are given in chapter 4). In the mixed layer, potential temperature and salinity are relaxed to Levitus data (or Kiel data near the northern boundary) averaged over the depth of the mixed layer. A zero order ice model is also included, simulating ice cover by setting the heat flux to zero whenever the surface temperature falls below the freezing temperature for sea ice (-1.8^oC). No-slip conditions apply at the lateral boundaries.

Sub-grid scale processes are parameterised using harmonic mixing. There are three mixing coefficients for isopycnic diffusion of momentum, layer thickness and tracers. They are written in the form of velocities, representing the ratio of the diffusion coefficients to the model grid spacing, and are constant. Since the mesh size decreases with the latitude, according to the scale-factor $\cos\varphi$, keeping the diffusion velocity constant is equivalent to a decrease in the diffusivity towards the poles. In this way the internal Rossby radius dependence on the Coriolis parameter is mimicked. The magnitudes of the diffusion velocities for the performed experiments, are 0.5 for temperature, salinity and passive tracers and 1.0 cm/s for momentum, whereas for the thickness diffusion velocity a range of values has been used in order to perform a sensitivity analysis (see chapter 4). This configuration includes a small amount of

diapycnal mixing, with the diffusion coefficient inversely proportional to the Brunt-Väisälä frequency (N): a_0/N, where a_0 is set to $10^{-3}cm^2s^{-2}$.

Chapter 4

Sensitivity experiments under a climatological forcing

In this chapter the sensitivity of the ocean intrinsic viariability to changes in the level of internal dissipation and the strength of the meridional overturning rate (the latter, modulated by varying the Mediterranean outflow (MO) strength) under a climatological forcing, is analysed.

4.1 Introduction

The aim of this chapter is to document the model sensitivity with respect to a specific turbulence closure parameter, the thickness diffusion, and the strength of the MO. The underlying goal is to identify the regions of the unforced system[1] parametric space whereby decadal and longer term variability spontaneously occurs. In order to identify both the regions of the phase space where low frequency behaviour takes place and the dominant timescales characterising the spectrum of the ocean natural variability, a set of climatological numerical experiments has been designed. The dynamical system under investigation features a multi-dimensional parametric space and a thorough sensitivity study (with the adopted resolution and the currently available computational resources) is infeasible, particularly if decadal scale phenomena are to be resolved. Thus, the sensitivity analysis needs to focus on a specific subset of the full parametric space. Subgrid scale parameters, setting the strength of unre-

[1] The term *unforced* refers to a system which is forced with fluxes containing no variability apart from the seasonal cycle.

solved physical processes, are a natural candidate for both theoretical and practical reasons.

Firstly, there is growing evidence supporting the idea that the level of dissipation in the ocean may set the transition from a stable state to an oscillatory solution. Simulations carried out with simplified general circulation models (*Huang and Chou*, 1994; *Marotzke*, 1997; *te Raa and Dijkstra*, 2002) and planetary geostrophic models (*Huck et al.*, 1999; *Colin de Verdière and Huck*, 1999) show that interdecadal oscillations, associated with the instability of the THC, are likely to occur when critical thresholds are crossed in the phase space defined by the turbulence closure parameters, suggesting the presence of a Hopf bifurcation (*Drazin*, 1992). The highly simplified nature of the above mentioned experiments raises an obvious issue: do the revealed features withstand a more realistic experimental setting (higher resolution, realistic bottom topography and surface fluxes, etc.)? Experiments performed with relatively sophisticated models are needed in order to test the robustness of some of the low complexity models results.

A number of subgrid scale parameters governs the turbulent mixing processes in an OGCM. In the real system, mesoscale baroclinic eddies (the most energetic component of the eddy field) are considered to be responsible for converting the available potential energy into eddy kinetic energy, by flattening the sloping isopycnal surfaces. This is an essentially adiabatic process, naturally implemented in isopycnic coordinate models through a downgradient diffusion term in the layer thickness tendency equation. Hence, thickness diffusion well represents the physics of the eddy field and is the turbulent mixing parameter selected to perform the sensitivity analysis.

It must also be emphasized that sensitivity studies of OGCMs to turbulence closure parameters have been mostly performed within the framework of z-coordinate models, which are notoriously unable to clearly separate isopycnal from diapycnal mixing. Vertical (horizontal) mixing can be identified with diapycnal (isopycnal) mixing only when constant density surfaces are coincident with geopotential surfaces. Hence, in the presence of sloping isopycnic surfaces both vertical and horizontal mixing coefficients induce some degree of isopycnal and diapycnal diffusion. Isopycnic coordinate models, on the other hand, allow a clear separation between diapycnal and isopycnal mixing.

The former plan of analysing the model sensitivity to eddy mixing only was revised following the (rather incidental) discovery of the important role played by the param-

eterised MO on the low frequency variability of the system under investigation. This led to an extension of the initially planned set of experiments, and a dimension to the phase space to be analysed in the sensitivity study, was added. Bearing in mind the deficiencies of the MO representation in the present model configuration (detailed in the next section) caution is needed in the interpretation of this particular subset of experiments. In fact, it would be hazardous to infer from this set of results any sound conclusion regarding the impact of the Mediterranean Sea on the large scale circulation of the Atlantic Ocean. However, as it will be shown in section 4.3, changes in the parameterised MO affect the amplitude of the meridional overturning cell. The same effect, but for different dynamical causes, is achieved by modulating the diapycnal diffusivity, as shown in other sensitivity studies (*Bryan*, 1987; *Marotzke*, 1997; *Zhang et al.*, 1999). The latter methodology is in fact a more orthodox procedure, commonly used to modify the mean state of the meridional overturning circulation. Nonetheless, the chance discovery of an effective equivalence between the MO and diapycnal mixing with respect to the amplitude of the meridional overturning (complementary to thickness diffusion, representing an isopycnal process) corroborated the decision of including the MO dependency experiments in the sensitivity analysis. Indeed, here the focus is on the effect of the meridional overturning circulation strength on the system low frequency variability, regardless of the specific methodology followed to modulate the overturning cell amplitude.

4.2 Experimental setup

As stressed in the previous section, the sensitivity analysis is carried out in a two-dimensional parametric space, defined by the thickness diffusivity and the MO strength.

As the Mediterranean Sea is not explicitly included in the model domain, the input of Levantine Intermediate Water (*Wüst*, 1961) into the Atlantic is simulated through a relaxation boundary condition applied to the layer interface depths in a buffer zone located in the model Gulf of Cadiz (GoC). Salinity relaxation to climatology is also applied, but has no effect on the model dynamics as the vertical density distribution remains unchanged. The water mass exchange between the Atlantic and the Mediterranean system can be estimated from the volume changes induced on each layer as a net effect of the restoring boundary condition in the GoC. Negative (positive) volume

changes in a given layer represent a sink (source) of mass for that layer, or equivalently an eastward flow entering (westward flow outcoming from) the Mediterranean Sea. As stressed by *Jia* (2000), this lateral boundary condition acts as a water mass transformation device, simulating the diapycnal flows taking place in ocean regions external to the model domain. The same restoring condition, applied to buffer zones at the northern and southern boundaries, provides the parameterization of the water exchange with the Nordic Seas and the South Atlantic, respectively, closing the meridional overturning circulation. Depending on the deepest layer interface to be restored, MOs of different strength and density structure can be obtained. *Jia* (2000) showed that the restoring condition as implemented in the present study, tends to act as a sink (source) for the layers below (above) the deepest interface being relaxed.
Three different boundary conditions in the GoC are used: a full depth relaxation, where the relaxation is extended down to the deepest layer interface, an intermediate depth relaxation, where the relaxation is applied down to the upper interface of layer 15 ($\sigma_0 = 27.88$), and a no relaxation boundary condition. Accordingly, the experiments are grouped in as many ensembles, identified as HMED, IMED and NOMED, respectively. For each ensemble, thickness diffusion velocity u_d (the ratio between the thickness diffusion coefficient and the mesh size) is varied over a wide range of values, with the extremes differing by one order of magnitude.
The experiments are summarized in Table 4.1, as a function of thickness diffusion velocity and the type of boundary condition in the GoC.

The annually averaged layer-by-layer volume change generated in the GoC buffer zone by the relaxation, converted to transport values, is shown in figure 4.1, for the experiments I01 and H01, representing the classes of experiments IMED and HMED, respectively. For both of these experiments a diffusion velocity of 0.1 cm/s was used. *Jia* (2000) performed a numerical experiment identical to I01 except that thickness diffusion velocity was set equal to $0.5cm/s$. The resulting MO pattern (figure 9b in *Jia* (2000)) shows no substantial differences with respect to the case $u_d = 0.1cm/s$, which will be described below.

For experiment I01 the MO signature is confined on model layer 15 ($\sigma_0 = 27.88$) with a total transport of 7.5 Sv (1 Sv= $10^6 m^3 s^{-1}$). As the relaxation is extended to the upper 15 layer interfaces, there is a tendency for the upper 14 layers (interface 15 is the lower bound of layer 14) to act as a sink of water, which has to be compensated by a westward flow in the layers below. Experiment H01 exhibits a deeper MO,

Experiment	Thickness Diffusion at the Equator (m^2/s)	u_d (cm/s)	Mediterranean Outflow (Sv)	B.C. in the GoC
H0	0	0.0	9.5	
H005	75	0.05	9.5	
H01	150	0.1	9.5	HMED
H02	300	0.2	9.5	
H1	1500	1.0	9.5	
I01	150	0.1	7.5	
I02	300	0.2	7.5	IMED
I05	750	0.5	7.5	
I1	1500	1.0	7.5	
N005	75	0.05	0.0	NOMED
N01	150	0.1	0.0	

Table 4.1: Summary of parameter values used in the sensitivity experiments. Experiments are labelled in a self explanatory way, the first letter identifying the experimental ensemble, followed by the corresponding diffusion velocity.

mostly occurring on layer 16 ($\sigma_0 = 27.92$) with a smaller contribution from layer 15. The combined transport is 9.5 Sv. The downward displacement of the outflow core,

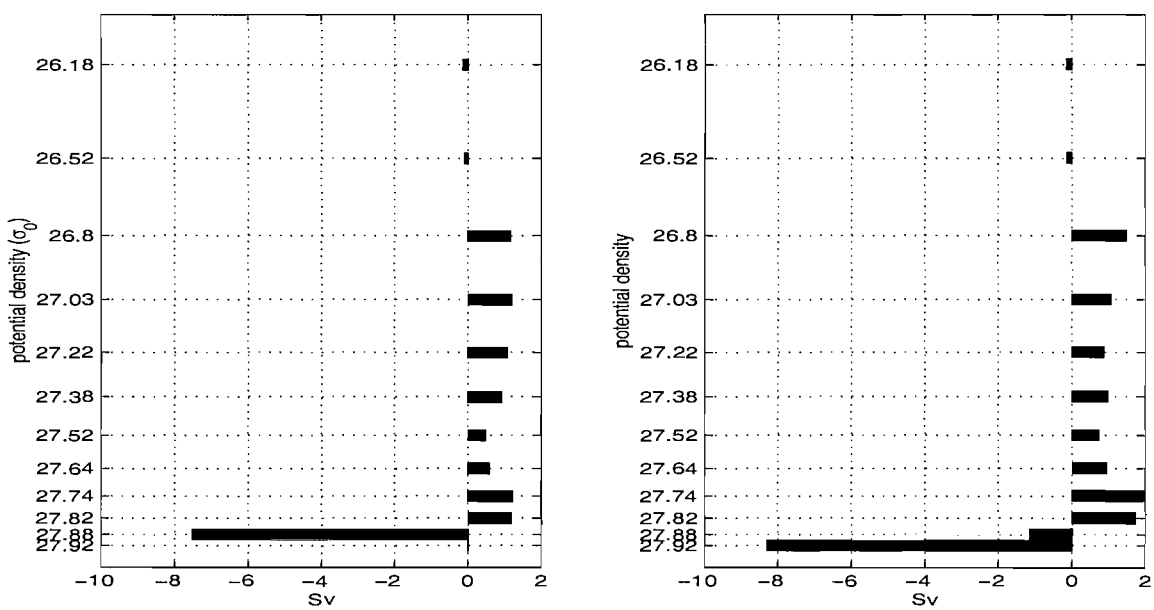

Figure 4.1: Transport induced by the restoring condition in the GoC for experiments I01 (left) and H01 (right).

with respect to the I01 case, stems from the use of a full depth relaxation, which tends to induce most of the outflow in the deepest layer. Layers with a density lighter than $\sigma_0 = 26.18$ have transports close to zero, as they outcrop south of the GoC, during most part of the year, whereas density classes heavier than 27.92 are mostly massless in the GoC, and their transports are also negligible. For this reason, only model layers 5 to 16 have been included in figure 4.1.

It must be emphasized that the representation of the MO obtained with the presented experiments, is far from being realistic, as can be inferred from a direct comparison with observations. A recent estimate of the MO transport in the GoC (*Baringer and Price*, 1997) provides a value of about 1.9 Sv in the density range of 27.3-28.0. Both the amplitude and the density structure of the model MOs deviate considerably from the observations. The strength of the MO differ from the observed value by a factor of 4 (5) for experiment I01 (H01) whereas both the numerical experiments exhibit a too dense overflow compared to the observations. Many factors concur to create the above mentioned discrepancies. *Jia* (2000) shows that a considerable reduction in the MO strength is achieved when a higher resolution ($\frac{1}{3}^o$) version of the presently used model is employed. The use of surface referenced potential density as a vertical coordinate may also play a role.

The no relaxation boundary condition experiments (NOMED ensemble) exclude the effect of the Mediterranean Sea by setting the overflow to zero, so providing a lower bound to the range of MO values being used in the sensitivity study.

As we are interested in the variability due to the internal dynamics, no interannual variations have been introduced in the fluxes of buoyancy and momentum, and a simple climatological forcing (described in chapter 3) has been used. The performed numerical experiments provide a *patchy* sampling of the phase space. The incompatible needs of a thorough exploration of the parametric space and the study of the ocean variability on interdecadal timescales (requiring multi-century model integrations) led to a partial undersampling of the phase space. Nonetheless, the major features of the model sensitivity with respect to the selected parameters, have been captured (as it will be shown in the next section). The occurrence of self-sustained oscillations of the meridional overturning circulation in the low diffusivity-high MO portion of the parametric space, led to increase the number of experiments in that region. In particular, a zero diffusivity experiment was performed aimed to clarify whether the use of low diffusivities may affect the numerical solutions by introducing

a computational mode.
For all the performed experiments the model is initialized with a state of rest, with potential temperature and salinity fields given by *Levitus* (1982) September climatology. All the numerical simulations have been run for a minimum time length of one century. Experiments showing a higher degree of variability, notably the low diffusivity ones, have been integrated for a longer time, in order to better resolve the processes occurring over decadal and interdecadal timescales.

4.3 Spinup and equilibrium states of the meridional overturning

The meridional overturning (quantified through the meridional overturning streamfunction; see below) is an integral descriptor of the large scale ocean motion, commonly identified with the thermohaline circulation, and it will be used here to diagnose the evolution of the model spin-up. The meridional overturning streamfunction is defined as the zonally integrated meridional mass transport above the isopycnic surface σ_θ:

$$\Psi(\phi, \sigma_\theta) = \int d\lambda a cos\phi \int_{h(\lambda,\phi,\sigma_\theta)}^{0} dz' v(\lambda, \phi, z') \tag{4.1}$$

where ϕ is the latitude, λ is the longitude, z is the depth, a is the earth radius and $h(\lambda, \phi, \sigma_\theta)$ is the interface depth of the constant potential density surface σ_θ.
In figure 4.2, the time series of the annually averaged maximum meridional overturning stream function for the full set of experiments, are shown. Two distinct types of transient behaviour can be identified. Experiments performed with high diffusivity values ($u_d \geq 0.2 cm/s$) and all the IMED experiments, are characterised by a three phases spinup: a very rapid decay, occurring in about 10 years, followed by a slower adjustment in the successive decade, and a slow convergence towards a (statistically) steady state, which extends until year 50, approximately. The low diffusivity experiments ($u_d \leq 0.1 cm/s$), for HMED and NOMED lateral boundary conditions, show decadal and multidecadal fluctuations, starting on year 17, and persisting through the entire model integration, with an amplitude of up to 5 % of the mean. A synoptic view of the mean states reached by the model meridional overturning in the selected two-dimensional parametric space, is shown in figure 4.3. The mean states are calculated from the time series of the maximum annually averaged meridional

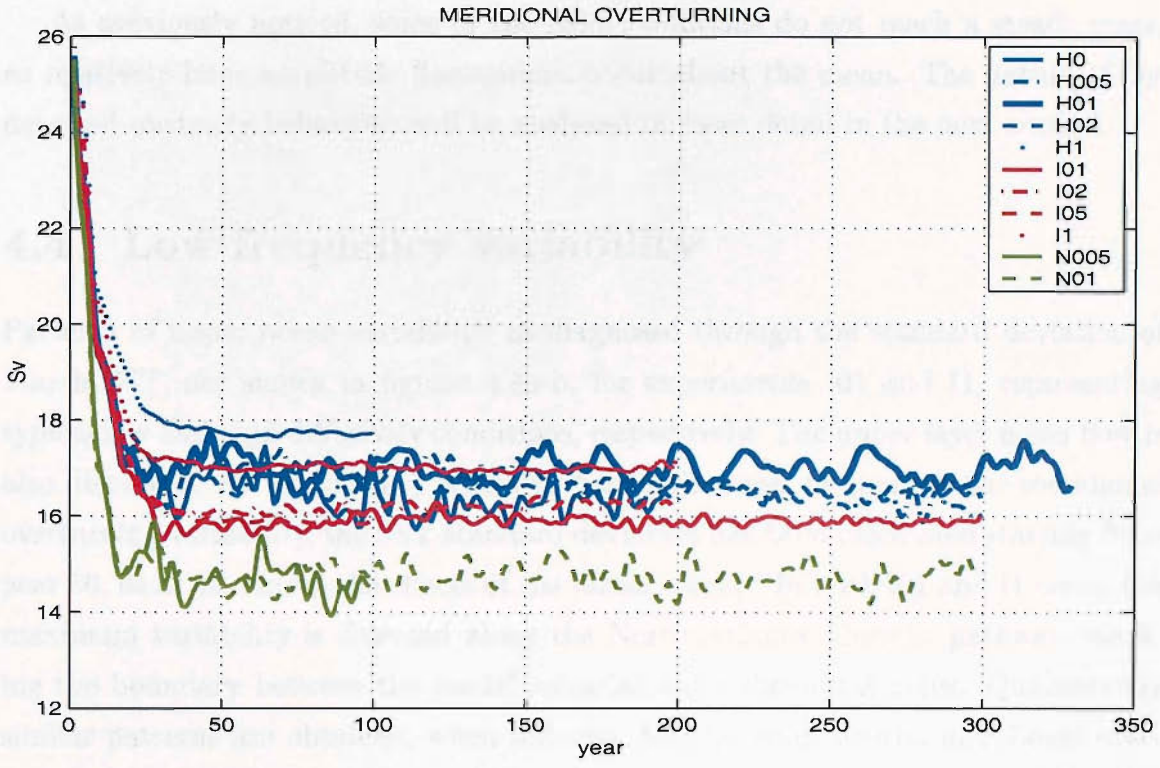

Figure 4.2: Time series of the maximum annually averaged meridional overturning streamfunction (Sv) over the Northern Hemisphere as a function of thickness diffusivity and Mediterranean outflow. Colors refer to the diffent MO strength: HMED (blue), IMED (red) and NOMED (green). See the legend for further details.

overturning streamfunction in the Northern Hemisphere, after removal of the initial 50 years, strongly affected by the spinup. The level of variability around the mean state, computed as ± 1 standard deviation, is also shown.

The overturning exhibits an overall increasing trend as the diffusivity and the MO are enhanced. Changes in the thickness diffusivity by one order of magnitude result in a 1 Sv increase of the meridional mass transport for both the intermediate and high MO cases, which is about 6 % of the mean overturning. An approximately 10 Sv increment in the MO (i.e.,from NOMED to HMED) induces a 10-15 % enhancement of the meridional overturning cell. Analysing the causes of the ocean response sensitivity to isopycnal mixing is outside the scopes of this thesis. However, it is interesting to notice the relatively modest impact of thickness diffusivity on the meridional overturning strength, compared to analogous sensitivity experiments performed by changing lateral diffusion, in z-coordinate models. The rigorous split between isopycnal and diapycnal mixing, implicit in isopycnal models formulation, rules out any possible spurious diapycnal mixing effect associated with the eddy mixing parameterization.

As previously noticed, some of the model solutions do not reach a steady state, as relatively large amplitude fluctuations occur about the mean. The nature of the detected unsteady behaviour will be analysed in more detail in the next section.

4.4 Low frequency variability

Patterns of upper ocean variability, as diagnosed through the standard deviation of March SST, are shown in figures 4.4a-b, for experiments I01 and I1, representing typical low and high diffusivity conditions, respectively. The upper layer mean flow is also displayed. For consistency with the diagnostics used to quantify the meridional overturning variability, the SST standard deviation has been calculated starting from year 50, so as to remove the effects of the initial spinup. In both I01 and I1 cases, the maximum variability is detected along the North Atlantic Current pathway, marking the boundary between the model subpolar and subtropical gyres. Qualitatively similar patterns are obtained, when different MO (or equivalently, meridional overturning) strengths are used (not shown). As the thickness diffusion is increased, the mean position of the NAC, east of 40°W , swings to the north, the intensity of the

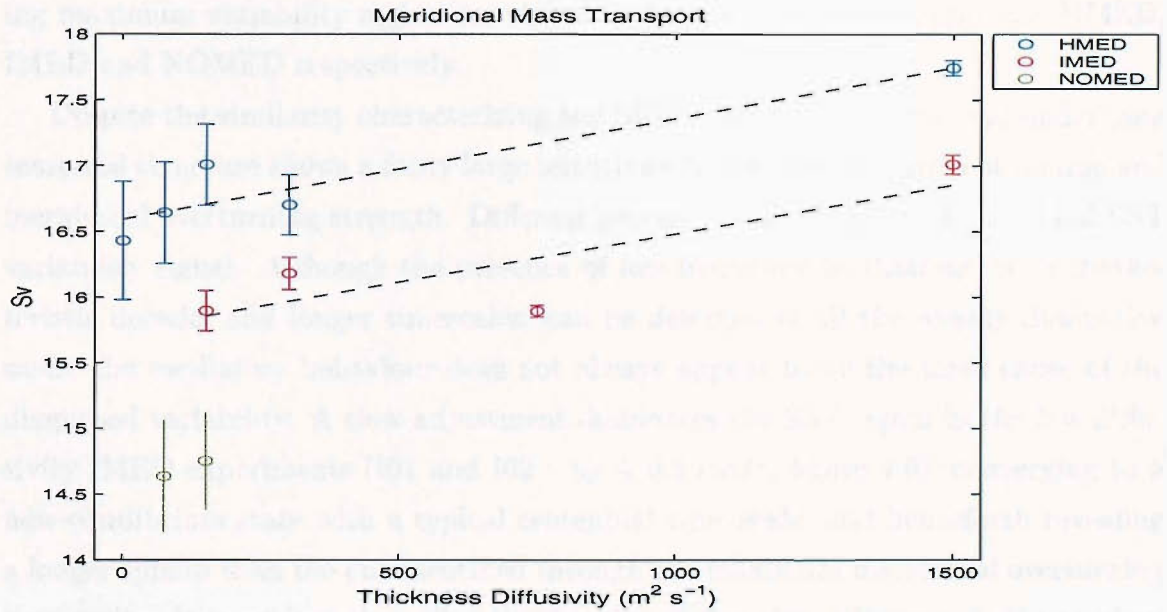

Figure 4.3: Time mean of the maximum annually averaged meridional overturning streamfunction (Sv) over the Northern Hemisphere as a function of thickness diffusivity and Mediterranean outflow. The bars around the mean are computed as ±1 standard deviation of the meridional overturning. The first order polynomial fit for HMED and IMED experiments is also shown (dashed lines). Diffusivity values are evaluated at the equator.

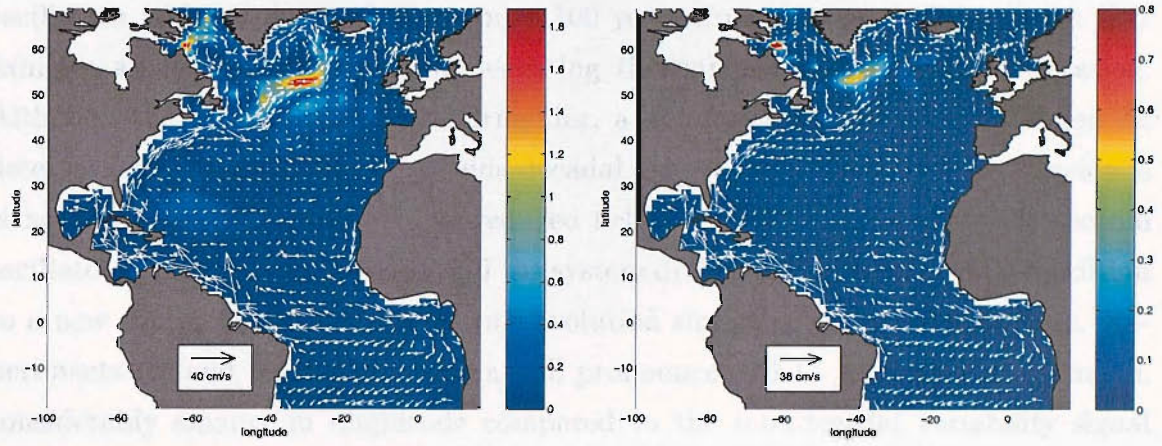

(a) (b)

Figure 4.4: Standard deviation of March SST for experiment (a) I01 and (b) I1 (^{o}C; shaded contours). The upper layer mean flow is also shown (vectors).

upper layer variability signal diminishes, and the area of the maximum SST variability region, located along the subpolar front, undergoes a sensible reduction.
Time series of the SST in single gridpoints selected within the core of the corresponding maximum variability region are shown in figures 4.5-7, for experiments HMED, IMED and NOMED respectively.

Despite the similarity characterizing the SST variability patterns, the underlying temporal structure shows a fairly large sensitivity to the level of turbulent mixing and meridional overturning strength. Different processes contribute to the detected SST variability signal. Although the presence of low frequency oscillations, with characteristic decadal and longer timescales, can be detected in all the weakly dissipative cases, the oscillatory behaviour does not always appear to be the main cause of the diagnosed variability. A slow adjustment dominates the SST signal in the low diffusivity IMED experiments (I01 and I02 : $u_d \leq 0.2\ cm/s$; figure 4.6), converging to a new equilibrium state with a typical centennial time scale, and henceforth revealing a longer spinup than the one identified through the maximum meridional overturning time series. It is evident that after the removal of this slow adjustment, the residual variability would have a marginal amplitude. High diffusivity IMED simulations (I05 and I1), on the other hand, do not show any significant variability on the decadal timescale.
Large amplitude oscillations appear in a narrow range of diffusivity values for the

HMED experiments (figure 4.5). In particular, experiment H005 reveals a 40 years oscillation which is damped after about 100 years from the onset. Experiment H01 exhibits an oscillatory behaviour persisting through the whole model integration. Although the oscillation is rather irregular, a dominant 50 years timescale can be detected, along with minor amplitude decadal fluctuations. As thickness diffusion is either increased above $u_d = 0.1$ or reduced below $u_d = 0.05\ cm/s$, the multidecadal oscillatory behaviour disappears, and the system drifts away from the initial condition to a new equilibrium state with a time evolution similar to IMED experiments. Experiments H0 and H005 also reveal a well pronounced 10-15 years oscillatory mode, considerably smaller in amplitude compared to the interdecadal variability signal found in experiment H01. Decadal scale variability is also detectable in the NOMED experiments (figure 4.7). The intercomparison between experiments N01, I01 and H01 (characterised by the same diffusion velocity, $u_d = 0.1\ cm/s$, but different MO) shows the impact of the MO on the low frequency response of the analysed system. Although decadal and multidecadal fluctuations are present in all of the compared experiments, it is only when the meridional overturning exceeds an amplitude of approximately 16 Sv (see figure 4.3) that an energetic multidecadal oscillation emerges. Similar considerations apply to experiments N005 and H005, showing a switch from

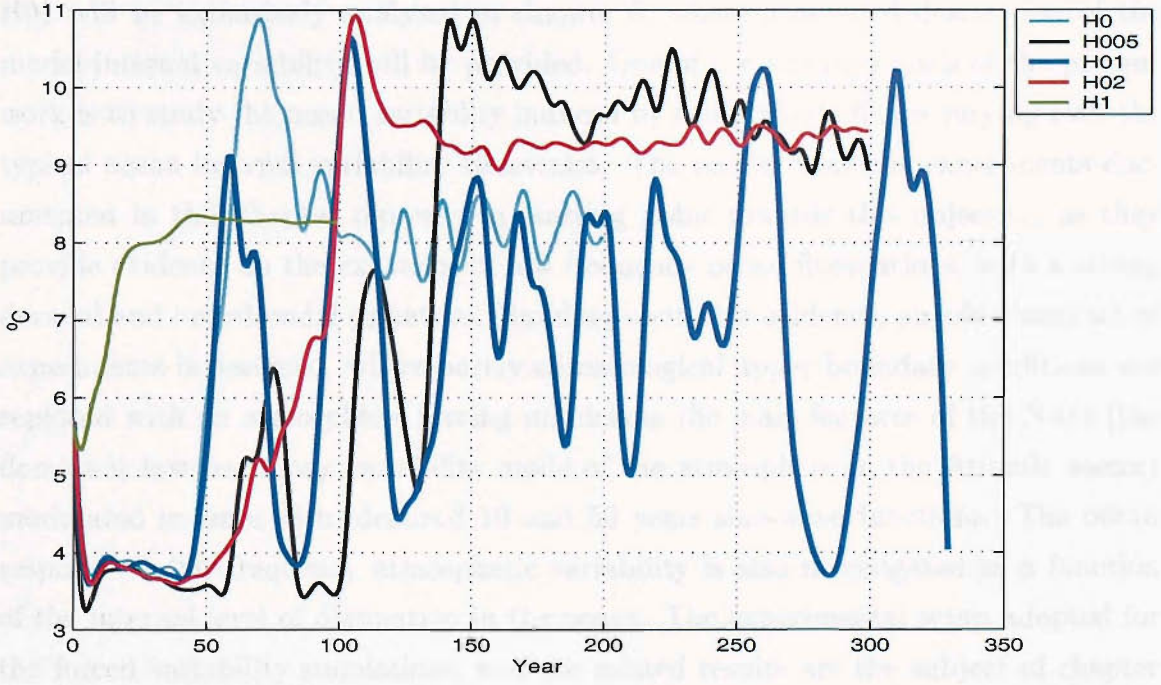

Figure 4.5: Time series of March SST (°C) in the NAC, for experiment ensemble HMED. Colours identify different diffusivity values.

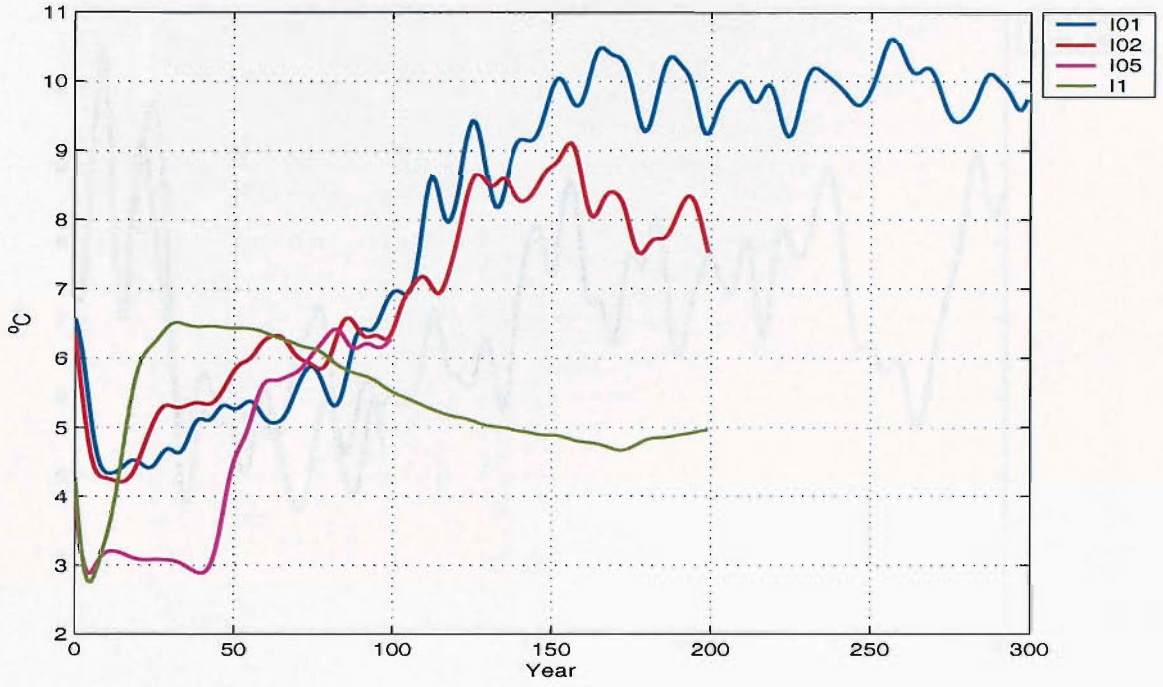

Figure 4.6: Time series of March SST (°C) in the NAC, for experiment ensemble IMED. Colours identify different diffusivity values.

a decadal scale variability to a multidecadal damped mode, excited under enhanced meridional overturning. The structure of the oscillatory mode found in experiment H01 will be extensively analysed in chapter 5, where a detailed description of the model internal variability will be provided. One of the ultimate goals of the present work is to study the ocean variablity induced by atmospheric fluxes varying over the typical ocean internal variability timescales. The results from the experiments documented in this chapter represent a starting point towards this objective, as they provide evidence on the existence of low frequency ocean fluctuations, with a strong decadal and interdecadal signature. Building upon this evidence, an additional set of experiments is designed, where purely climatological upper boundary conditions are replaced with an atmospheric forcing mimicking the main features of the NAO (the dominant low frequency variability mode of the atmosphere in the Atlantic sector) modulated in time with idealized 10 and 50 years sine-wave functions. The ocean response to low frequency atmospheric variability is also investigated as a function of the internal level of dissipation in the ocean. The experimental setup adopted for the forced variability simulations, and the related results are the subject of chapter 6. The model configuration corresponding to experiments I01 and I1 (IMED lateral boundary conditions at Gibraltar) is selected to perform the forced variability (NAO)

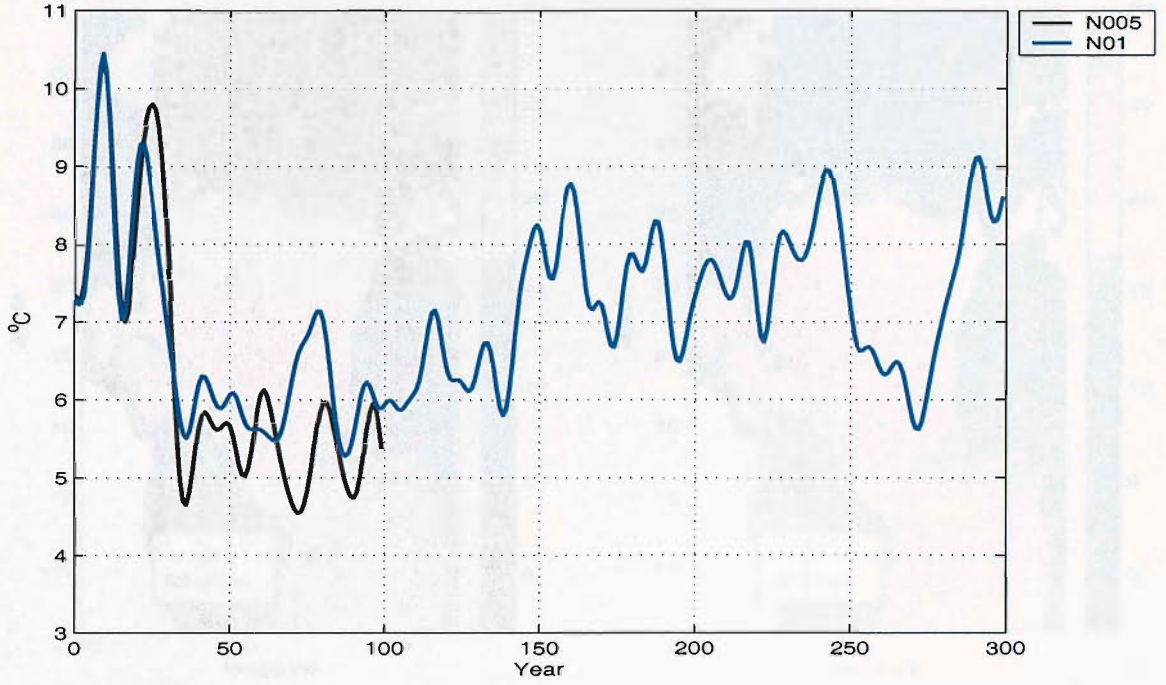

Figure 4.7: Time series of March SST (°C) in the NAC, for experiment ensemble NOMED. Colours identify different diffusivity values.

experiments, under typical low and high diffusivity conditions, respectively. This choice is motivated by the desire to have some representation of the MO in the system. The IMED boundary conditions provide the closest representation of the MO to observations, among the available experiments. The characteristics of I01 and I1 mean general circulation are described in the following section.

4.5 I01 and I1 experiments: mean states

In figure 4.8 patterns of the mean circulation and temperature in the upper layer are shown. Overall, the major features of the North Atlantic Ocean circulation are captured by the model. The main current systems, including the Florida Current, the Gulf Stream and the NAC, are reasonably well reproduced. A major model deficiency is represented by the Gulf Stream separation latitude, located north of 40°N, and hence far too north compared to observations, which provide an estimate of 35°N. This a well known limitation shared by similar resolution state-of-the-art OGCMs. The most pronounced differences between low and high diffusion solutions can be detected in the NAC pathway and strength. The jet-like structure featured by the low diffusivity NAC, is replaced in the high diffusion experiment, by a smoother current,

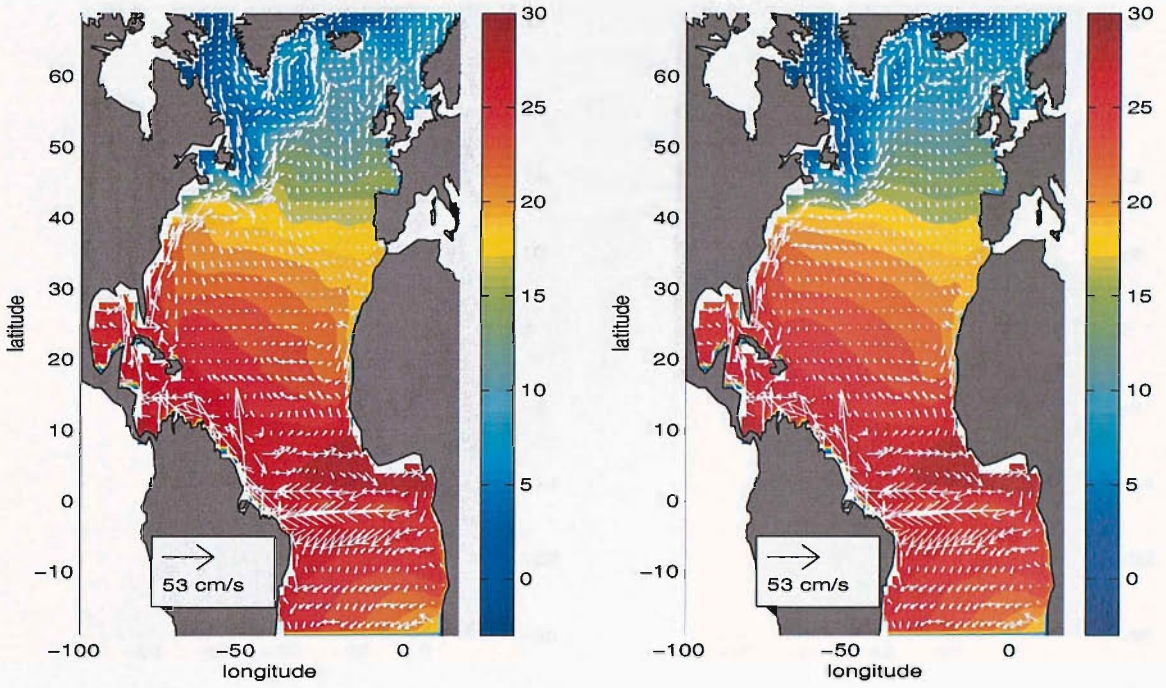

Figure 4.8: Mean upper layer velocity and temperature for experiments I01 (left) and I1 (right). Mean fields have been computed over the last 10 years of the model integration.

having a stronger meridional component.

The mean barotropic streamfunction is shown in figure 4.9. Both experiments show the characteristic North Atlantic double gyre circulation. The subtropical gyre strength is about 36 (35) Sv, for the low (high) diffusivity case. The most evident effect induced on the barotropic circulation by varying the level of mixing can be detected in the subpolar gyre strength and geometry. The subpolar gyre exhibits a 28 (20) Sv strength for the low (high) diffusivity experiment. Also, the related cyclonic circulation exhibits a reduced zonal extent as diffusivity is increased, consistent with the results from the upper layer mean flow pattern intercomparison. A cyclonic vortex, with a 1000 Km diameter, can be detected in the GoC. This structure represents a considerably unrealistic departure from a Sverdrup balance, in a region where there are no significant factors (e.g.,topographic features) to justify this discrepancy. This is a known model deficiency, related to the relaxation boundary conditions applied at Gibraltar to simulate the MO, also connected to the use of surface referenced potential density. A thorough discussion of this issue can be found in *Jia* (2000).

Figure 4.10 shows the mean meridional overturning streamfunction, in the potential density-latitude space. Buoyancy fluxes at the surface and relaxation conditions at the open boundaries and off Gibraltar appear to be the main factors concurring to

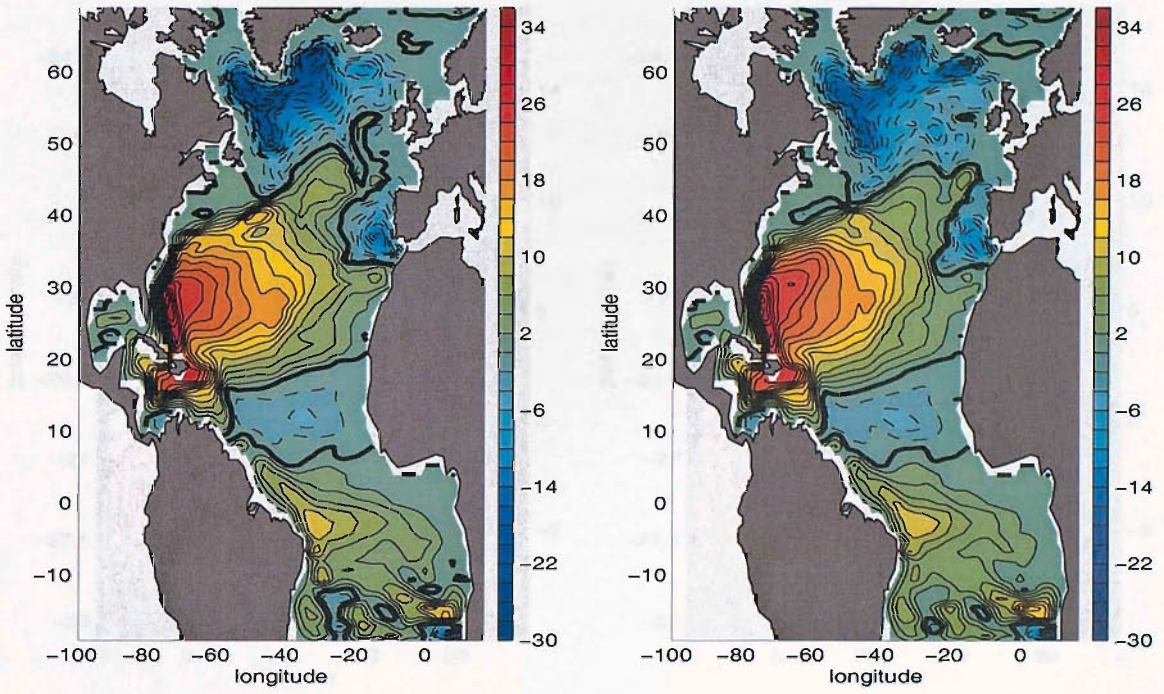

Figure 4.9: Mean barotropic streamfunction (Sv) for experiments I01 (left) and I1 (right). The contour interval is 2 Sv. The solid (dashed) line denotes positive (negative) values, whilst the thick solid line indicates the 0 contour. Mean fields have been computed over the last 10 years of the model integrations.

shape the model thermohaline circulation. The lower limb of the thermohaline cell (the model NADW) gradually increases while flowing southward. The strong diapycnal flow occurring at 35°N is clearly caused by the restoring boundary condition applied at Gibraltar, as already discussed in section 3.1. The strength of the overturning cell is about 16 (17) Sv for the low (high) diffusion case, and is consistent with the observational estimate provided by *Römmich and Wunsch* (1985).

4.6 Summary

Results from a sensitivity analysis of the ocean response with respect to eddy mixing and MO have been presented in this chapter. The analysed results strongly suggest that there are critical thresholds in the system, marking the transition from a stable solution (fluctuations occur about a well defined mean state) to an unstable behaviour, featuring large amplitude multidecadal oscillations. Both thickness diffusion and the strength of meridional overturning contribute to set the characteristics of the long term response of the upper ocean. In particular, an energetic overturn-

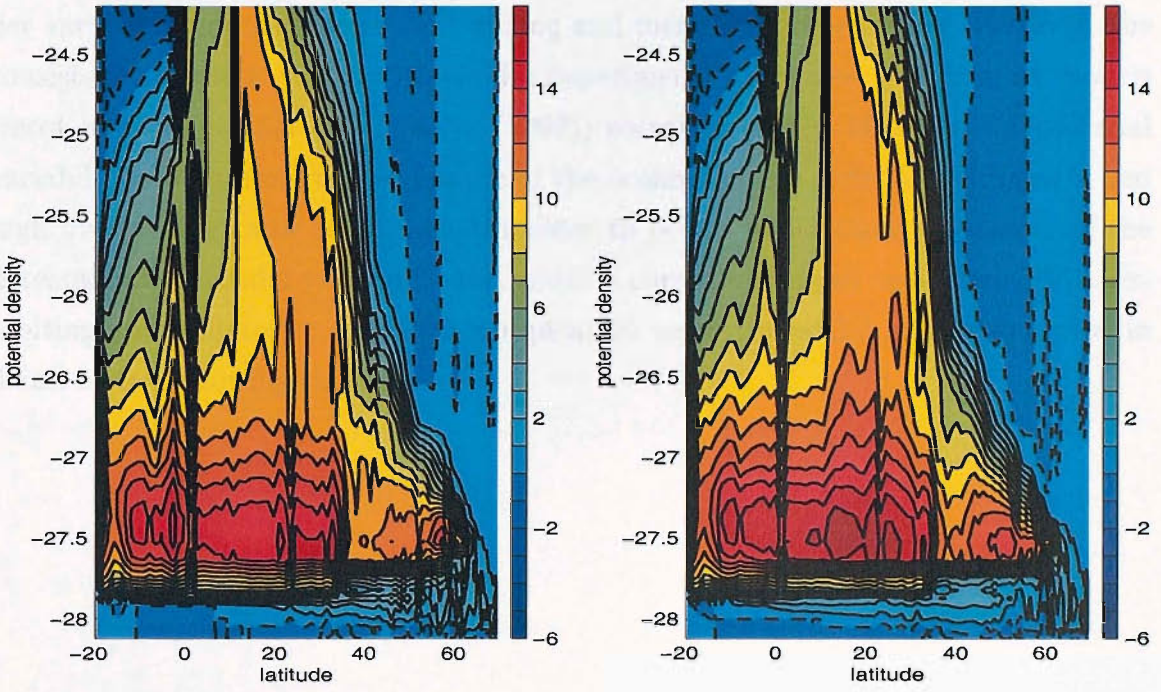

Figure 4.10: Mean meridional overturning streamfunction (Sv) for experiments I01 (left) and I1 (right). The contour interval is 1 Sv. The solid (dashed) line denotes positive (negative) values. Mean fields have been computed over the last 10 years of the model integrations.

ing combined with a weakly dissipative ocean provide favourable conditions to the existence of low frequency variability. The low frequency tail of the ocean response spectrum appears to be dominated by two timescales: a quasi-decadal 10-15 years timescale, insensitive to the overturning strength but damped at high diffusion, and a multidecadal 50 years timescale, which only emerges when the overturning exceeds a 16 Sv amplitude, and for a narrow range of internal dissipation levels. The existence of such a narrow interval of parameters whereby interdecadal variability occurs, may be explained as follows. High diffusivity works against the establishment of variability at any scale in the system. By reducing diffusion, low frequency modes appear more energetic. However, by reducing diffusion, the meridional overturning becomes weaker (on average), which in turn conteracts the onset of low frequency oscillations. Hence, there is an optimal interval of eddy mixing values which favours the existence of long term fluctuations. This may explain why, in the HMED group of experiments, setting the diffusivity to zero causes the multidecadal oscillatory mode to disappear. The undersampling of the parametric space (i.e., the absence of a full coverage of the phase space) and the lack of multicentury integrations for some of the numerical experiments, conspire against a clear understanding of the system behaviour, un-

der varying strengths of turbulent mixing and meridional overturning. However, the consistency of these results with similar experiments performed with simpler models (most notably, *te Raa and Dijkstra* (2002)) corroborates the idea that interdecadal variability modes are a robust feature of the ocean system, under low diffusivity and high overturning rates conditions. In order to better understand the nature of the detected multidecadal variability, the solution corresponding to experiment H01 (exhibiting an oscillatory mode with a typical 50 years timescale) will be analysed in detail in the following chapter.

Chapter 5

Interdecadal variability

In the previous chapter the sensitivity of the model equilibria to changes in the level of internal dissipation and the strength of the Mediterranean overflow was analysed. For a narrow interval of parameters, and specifically when the thickness diffusivity is lower than 300 $m^2 s^{-1}$ and the MO is higher than 7.5 Sv (IMED ensemble), it emerged that the model cannot reach an equilibrium state. In one of these experiments (labelled as H01) the meridional overturning undergoes an irregular oscillation exhibiting variability on interdecadal timescales. In this chapter the interdecadal mode is described in detail, along with the underlying mechanism. Unless otherwise specified, all the results described in this chapter refer to the experiment H01.

5.1 Sea surface temperature variability

The spatial structure of sea surface temperature variability for the experiment H01 is diagnosed through the SST standard deviation (figure 5.1). Only March temperature fields are accounted for in the calculation of the standard deviation so that the seasonal cycle signal is filtered out. Variability is mostly confined north of 45°N, and the maximum amplitude is detected in the eastern subpolar gyre. A minor amplitude feature is observed along an approximately zonal belt, centered at 23°N. Hovmüller plots show that this structure is related to a westward propagating wave-like disturbance with a period of approximately 2 years (not shown). The time series of March SST in 35°W,55°N, where the highest variability is detected, reveals the presence of a self-sustained irregular oscillation, spontaneously arising after 40 years from the model initialization (figure 5.2a). In order to emphasize the low frequency compo-

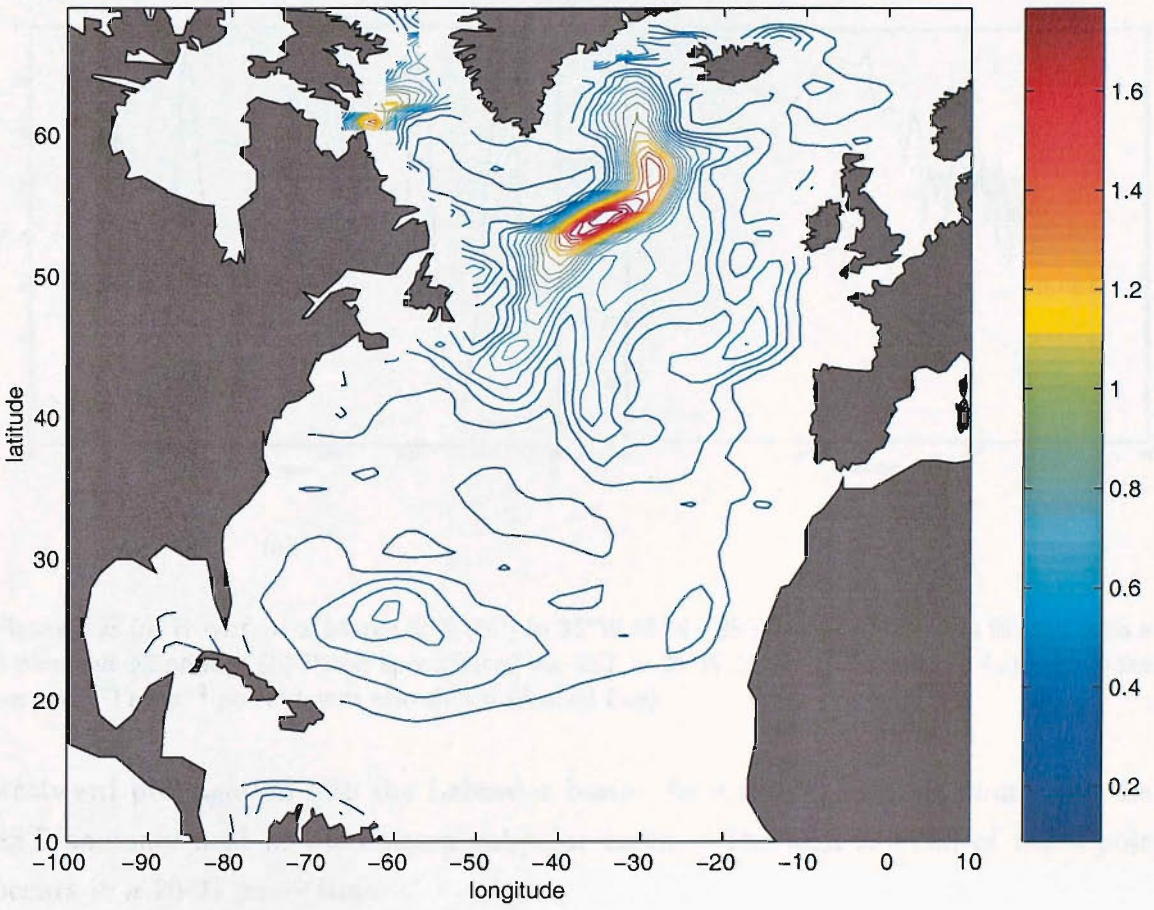

Figure 5.1: Standard deviation of March SST (°C) computed for experiment H01

nents of the signal, the time series has been low-pass filtered using a Butterworth filter with a 5 years cut-off period. A simple visual inspection of the time series reveals an approximately 50-years cycle emerging at the beginning and at the end of the oscillation. The power spectrum of the SST (figure 5.2b) conforms to an ω^{-2} power-law at high frequencies, and exhibits enhanced energy around the timescale of 50 years (0.02 cycles per year) in contrast with a red noise spectrum.

Figure 5.3 shows snapshots of March SST anomalies for a single 55 years long cycle of the thermal oscillation, in the northern part of the domain. Anomalies are computed by removing March climatology from istantaneous snapshots. The selected time interval corresponds to a particularly regular phase of the oscillation. Sub-basin scale SST anomalies with a magnitude of 2-3 ^{o}C drift poleward following the cyclonic circulation of the subpolar gyre. Anomalies propagate with an average speed of about 150 m/day, one order of magnitude smaller than the typical velocities in the subpolar gyre, and are ultimately dissipated in the Irminger Sea, with no further

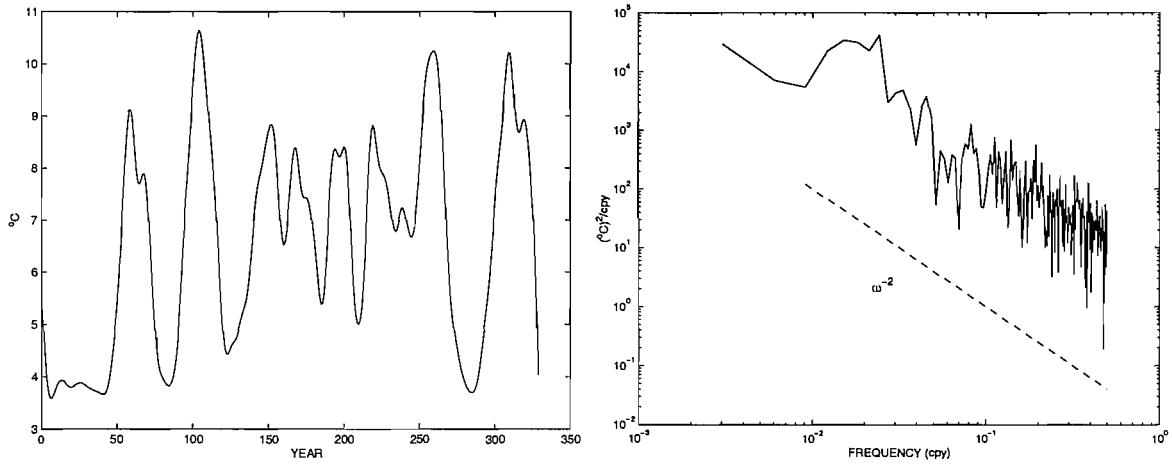

(a) (b)

Figure 5.2: (a) Evolution of March SST (^oC) in 35°W,55°N . SST has been low-pass filtered with a 5 years cut-off period. (b) Power spectrum of the SST in 35°W,55°N. The frequency (ω) is in cycles per year. The ω^{-2} power-law is also shown (dashed line).

westward propagation into the Labrador basin. As a result, a dipole dominates the SST anomaly field in the eastern subpolar basin . The sign reversal of the dipole occurs in a 20-25 years time.

In order to establish whether the described SST oscillation drives a similar variability in the density field, and to quantify the relative role of surface salinity, the density anomaly averaged over the Irminger Sea (where the maximum variability is detected) is calculated, along with the temperature and salinity contributions to the anomalous density field in that area (figure 5.4). The region designated for the calculation of the anomalous fields is bounded by 55.3 °N and 65.7 °N, 38.6 °W and 28 °W. SST and surface salinity anomalies are multiplied by their respective expansion coefficient values, $\alpha = 1.668 \times 10^{-4} K^{-1}$ and $\beta = 7.61 \times 10^{-4} psu^{-1}$, to provide the thermal and salinity components of the density anomaly. The latter is estimated by means of the linear relationship, $\Delta\rho_{lin} = \rho_0[\beta\Delta S - \alpha\Delta T]$, with $\rho_0 = 1027 Kgm^{-3}$. The density anomaly as diagnosed by the model equation of state ($\Delta\rho_{mod}$) is also shown, for comparison. Both $\Delta\rho_{lin}$ and $\Delta\rho_{mod}$ exhibit multidecadal fluctuations, coherent with the SST signal which dominates over salinity throughout the oscillation. Discrepancies between the linear and the model density anomalies can be traced back to the non linear terms in the equation of state employed by the model. Lateral advection of temperature and salinity in the mixed layer, along with the buoyancy fluxes at the

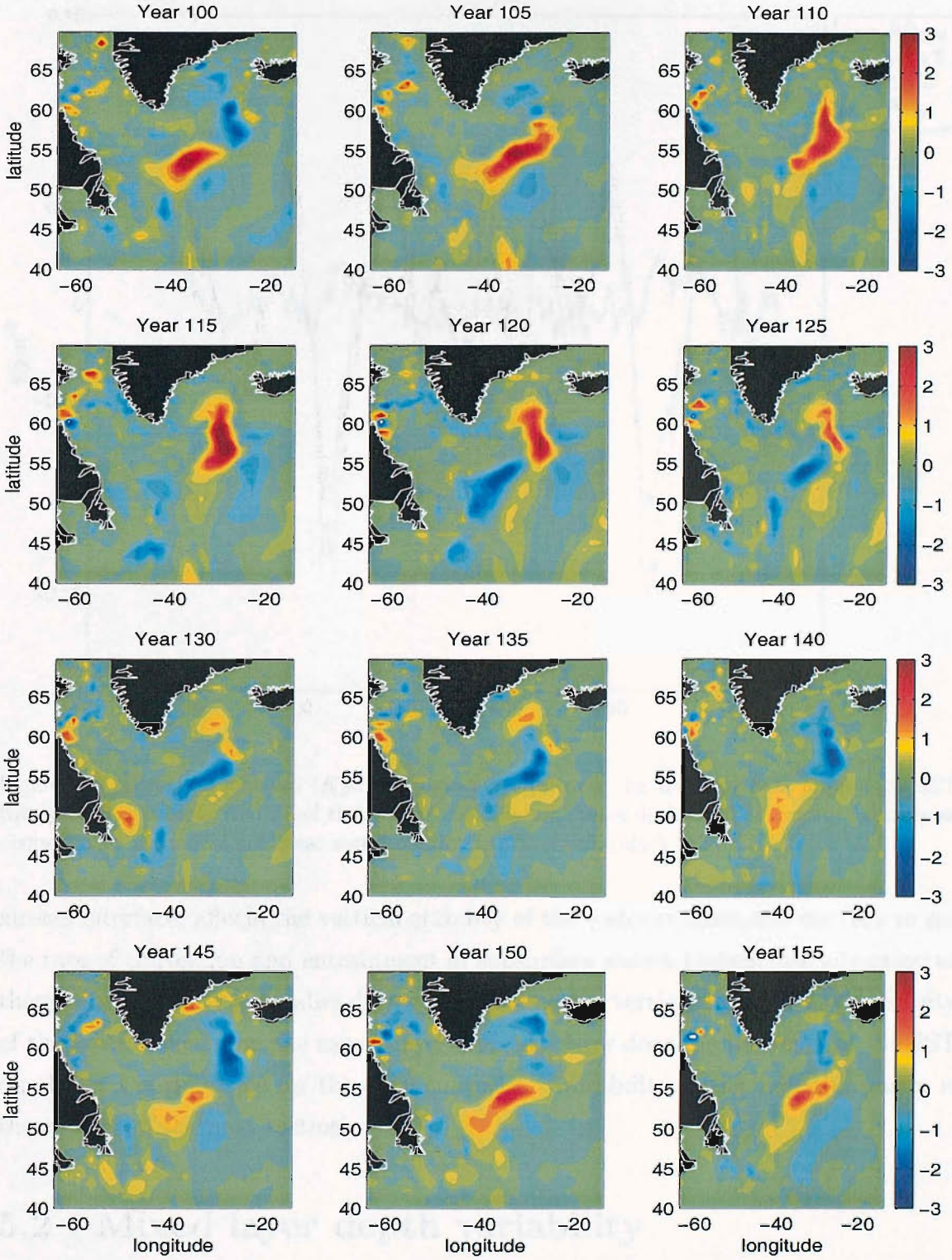

Figure 5.3: Anomalies of March SST (^{o}C; March climatology has been removed) for the time interval ranging from year 100 to year 155. The time spacing of each snapshot is 5 years.

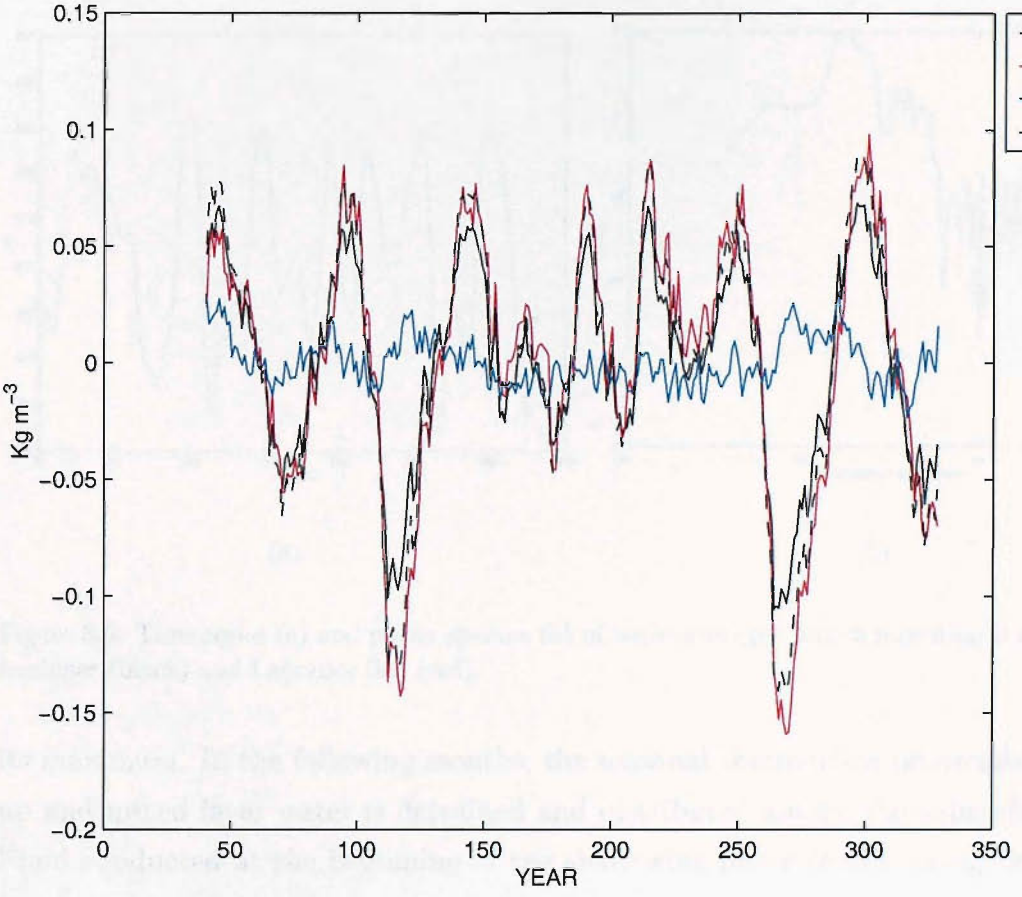

Figure 5.4: Density anomalies (Kgm^{-3}) basin-averaged over the Irminger Sea, implied by SST (blue), surface salinity (red), and their linear combination (black dashed). The density anomaly as diagnosed by the model nonlinear state equation is also shown (black solid)

air-sea interface, affects the vertical stability of the water column and concurs to set the rate of convection and entrainment of subsurface waters (subsurface advection of thermal and salinity anomalies does not impact on the vertical stability as the density of the layers other than the mixed layer is fixed). How does the inversion of the SST dipole set the timescale for the deep convection variability in the subpolar basin, is the subject of the next section.

5.2 Mixed layer depth variability

March mixed layer depth relates to the water mass formation process, occurring in the model as an effect of permanent subduction, namely the transfer of fluid from the mixed layer to the permanent thermocline. Water is accumulated in the mixed layer during the entrainment phase, culminating in March when the mixed layer depth is at

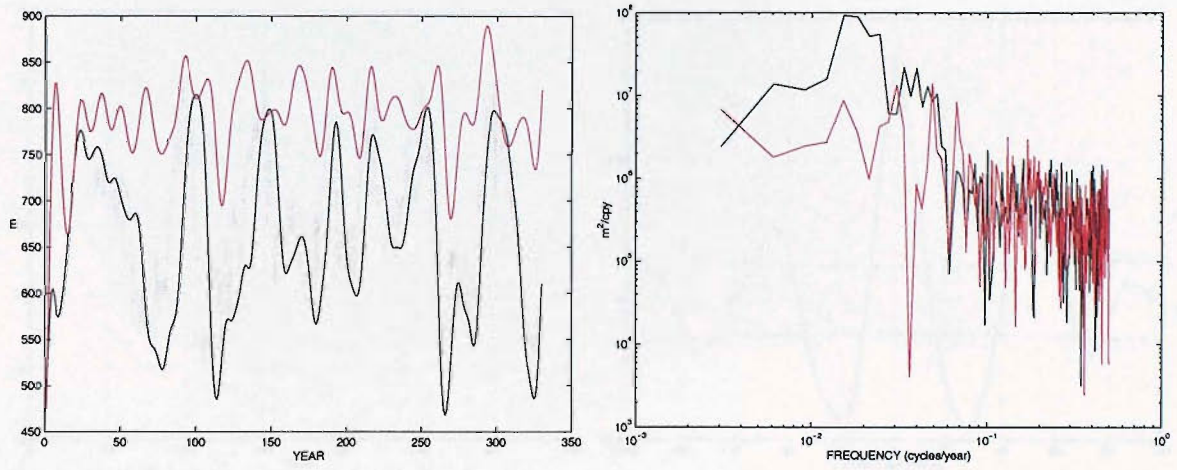

(a) (b)

Figure 5.5: Time series (a) and power spectra (b) of basin-averaged March mixed layer depth in the Irminger (black) and Labrador Sea (red).

its maximum. In the following months, the seasonal thermocline progressively builds up and mixed layer water is detrained and distributed among the subsurface layers. Fluid subducted at the beginning of the shallowing phase (early spring) irreversibly leaves the mixed layer and permanently enters the main thermocline, whereas water detrained from the mixed layer during summer is normally re-entrained the following winter, when the mixed layer deepening starts again. This mechanism, known as *mixed layer demon* (*Stommel*, 1979) produces a bias of the main thermocline properties toward those of winter mixed layer. Hence, the evolution of March mixed layer depth in the subpolar region, can be used as an indicator of the deep water formation process.

The SST variability pattern exhibits a rather strong zonal asymmetry at the northern latitudes, as the temperature anomalies only affect the eastern part of the subpolar basin (figures 5.1 and 5.3). Whether a similar asymmetry holds for the wintertime mixed layer depth is investigated by looking at time series in the eastern and western subpolar gyre. Figure 5.5a shows the time series of basin averaged March mixed layer depth in the Irminger and Labrador Sea basins. The Irminger Sea region employed for the averaging is defined as in the previous section. The Labrador basin is identified as the region bounded by 54.5 ^{o}N and 62.1 ^{o}N, 60 ^{o}W and 46.6 ^{o}W. For both time series, oscillatory components with a timescale shorter than 5-years have been filtered out. Decadal fluctuations are evident in both regions. Variability on interdecadal

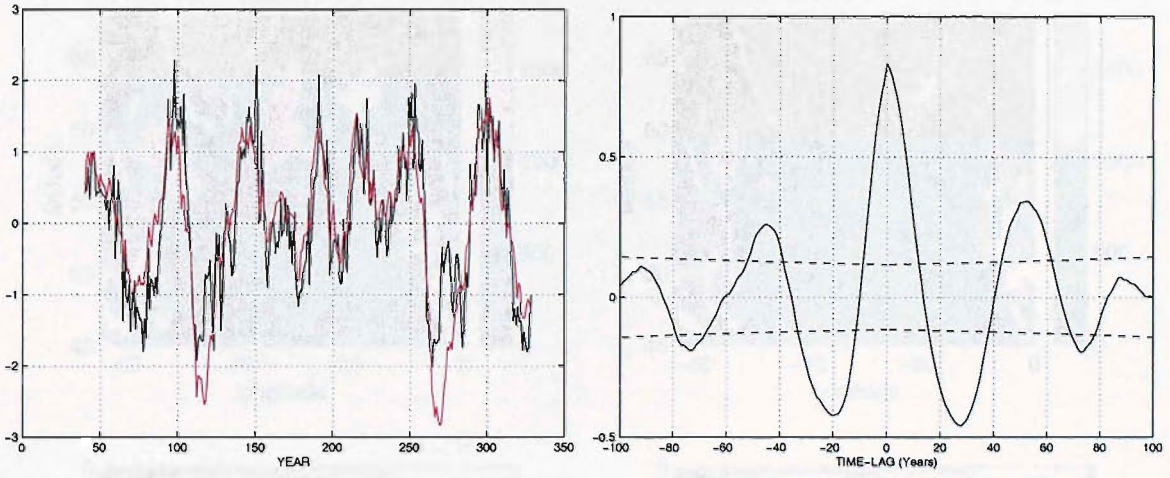

(a) (b)

Figure 5.6: (a)Time series of normalized March SST (red) and mixed layer depth (black) in the Irminger Sea. Normalized SST anomalies are plotted with the reversed sign. (b) Lagged correlation coefficients between March SST and mixed layer depth in the Irminger Sea. The dashed lines are the 95 % confidence limits.

timescales is more energetic in the Irminger Sea as confirmed by the power spectra (figure 5.5b) computed for each of the time series. A spectral peak around 0.02 cpy (50 years) is detected in the Irminger basin, which contrasts with a less energetic signature centered over the same timescales in the Labrador basin.

The time series for the normalized SST and mixed layer depth, basin-averaged over the Irminger Sea, are shown in figure 5.6a. Normalization of the time series is applied by subtracting the mean and dividing by the standard deviation. In order to facilitate the comparison with the mixed layer depth, normalized temperature anomalies are plotted with the reversed sign, so that positive peaks in the SST signal correspond to cold anomalies (implying positive density anomalies). Cold (warm) anomalies appear to be in phase with deep (shallow) mixing. The two signals are significantly correlated at lag 0 (correlation coefficient passes the 95 % confidence limit test of a Student's t-distribution) as shown in figure 5.6b. Statistically significant correlation also appears at both positive and negative time-lags with a roughly 50 years spacing (peak-to-peak), mirroring the quasi-oscillatory component contained in the signals.

The spatial structure of high latitude mixed layer variability is portrayed in figure 5.7 (upper panels). Two snapshots of March mixed layer depth relative to the extreme phases of the interdecadal fluctuation occurring in the Irminger Sea (years 100 and

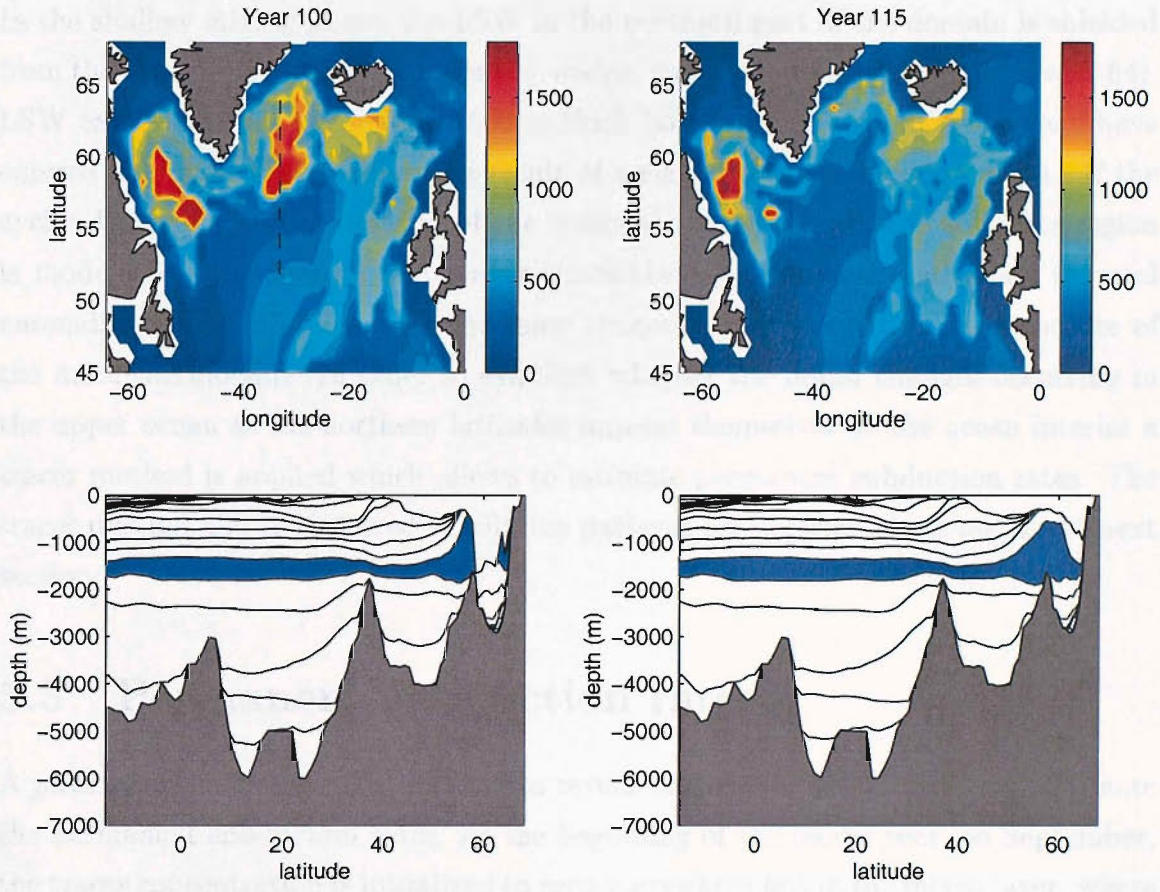

Figure 5.7: Upper panels: snapshots of March mixed layer depth in the subpolar basin on year 100 (left) and 115 (right). Lower panels: meridional-vertical sections at 34 °W (black dashed line in the upper rigth panel) showing the interface depths (black solid line) of isopycnal layers on year 100 (left) and 115 (right). The blue shading in lower panels indicates the layer corresponding to the model LSW (σ_0 = 27.74).

115) are shown. A drastic change in the convection pattern is observed. Mixing in excess of 1500 m takes place over both Labrador and Irminger basin, on year 100. After 15 years, deep mixing only occurs in the Labrador Sea, whereas in the Irminger Sea, mixed layer depths are as shallow as 500 m. The impact of this upper layer transient on the sub-surface layers displacement is illustrated in figure 5.7 (lower panels). Meridional-vertical sections of the isopycnal interface depths are shown for a transect crossing the Irminger basin at 34 °W (black dashed line in the upper left panel). The deep layer undergoing the most dramatic changes during the transient in the eastern subpolar basin, is layer 13 (σ_0=27.74) which will be identified as the model Labrador Sea Water (LSW; blue-shaded in figure 5.7, lower panels). During the deep mixing phase, mixed layer density in the Irminger Sea matches the LSW density, and the corresponding layer outcrops at 56 °N (figure 5.7, bottom left panel).

In the shallow mixing phase, the LSW in the northern part of the domain is shielded from the upper layer by a lighter density wedge, corresponding to layer 12 (σ_0=27.64). LSW exhibits an approximately 1500 m thick bolus-shaped region, which may have entered the main thermocline as a result of an anomalous subduction event. If the cyclic deepening and shallowing of the seasonal thermocline in the subpolar region is modulated over decadal and longer timescales by horizontally advected thermal anomalies, then variability over the same timescales is expected in the structure of the main thermocline. In order to establish whether the major changes occurring in the upper ocean at the northern latitudes imprint themselves on the ocean interior a tracer method is applied which allows to estimate permanent subduction rates. The tracer method and the inferred ventilation patterns are described in detail in the next section.

5.3 Permanent subduction rates

A passive tracer methodology is used to reveal the ventilation patterns and estimate the permanent subduction rates. At the beginning of the model year, on September, the tracer concentration is initialized to zero everywhere but in the mixed layer, where concentration is set to unity. During the mixed layer deepening phase, water from the interior layers is entrained into the mixed layer, and no tracer exchange with the main thermocline occurs. At the end of the winter season, the mixed layer shoaling starts, and the *tagged water* is detrained into the interior layers where it is advected and diffused. The tracer concentration on a constant density layer at a given gridpoint, represents the ventilated fraction of the layer thickness at that location. Therefore, the volume integral of the tracer concentration on an isopycnic layer is the volume of ventilated water on that layer. In figure 5.8 is shown the evolution of the ventilated water volume for the layer corresponding to the model LSW. Two time series are compared, relative to the model years 70 and 100, roughly corresponding to a trough and a peak respectively of the SST cycle shown in figure 5.4. The two series show a qualitatively similar evolution. Detrainment starts on March (month 6), and continues until July (month 9). An entrainment phase follows, characterised by the decrease in the volume of the ventilated water. However, only a fraction of the previously detrained water is reentrained into the mixed layer. When the entrainment reaches its maximum (March), the traced water which escaped the reentrainment represents the

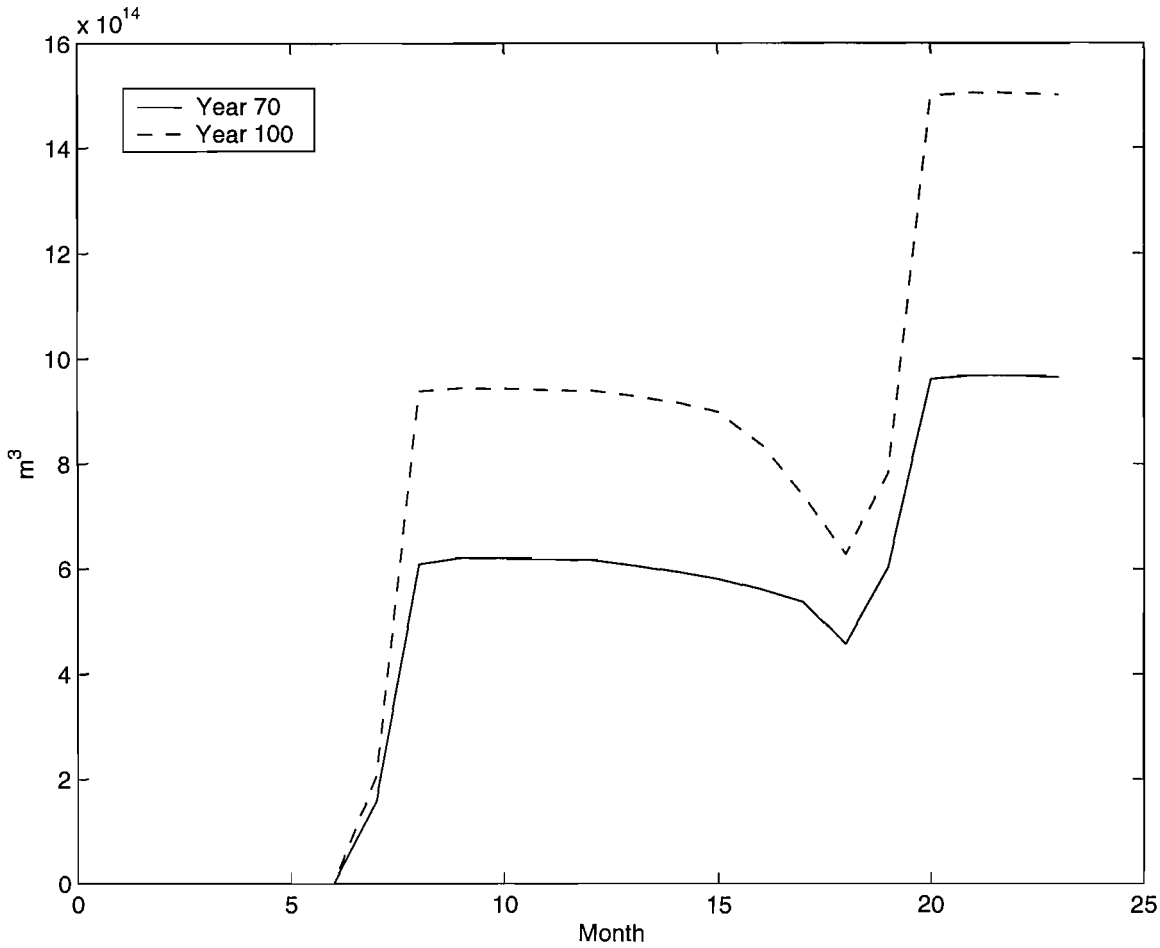

Figure 5.8: Evolution of the ventilated water volume (m^3) for the LSW, starting from yr 70 (solid) and yr 100 (dashed).

permanently subducted water, and its volume is estimated as the difference between two consecutive March values of the ventilated volume. This volume, converted to transport values after dividing by 1 year, provides the mean annual permanent subduction rate. Due to the progressive homogenization of the ventilation tracer over the isopycnal layers, the permanent subduction rate tends to decrease in time. In the present calculation the first March-to-March cycle has been used. The larger detrainment taking place on year 100, combined with an entrainment of equal magnitude for both time series, results into a net increase of the subduction rate for the LSW from year 70 to year 100. This is confirmed in figure 5.9 where layer-by-layer subduction rates, calculated for the time interval ranging from years 50 to 100, are displayed. The selected time interval corresponds to a complete cycle of the SST oscillation shown in figure 5.4. Subduction rates are computed at 5 years intervals. The signatures of

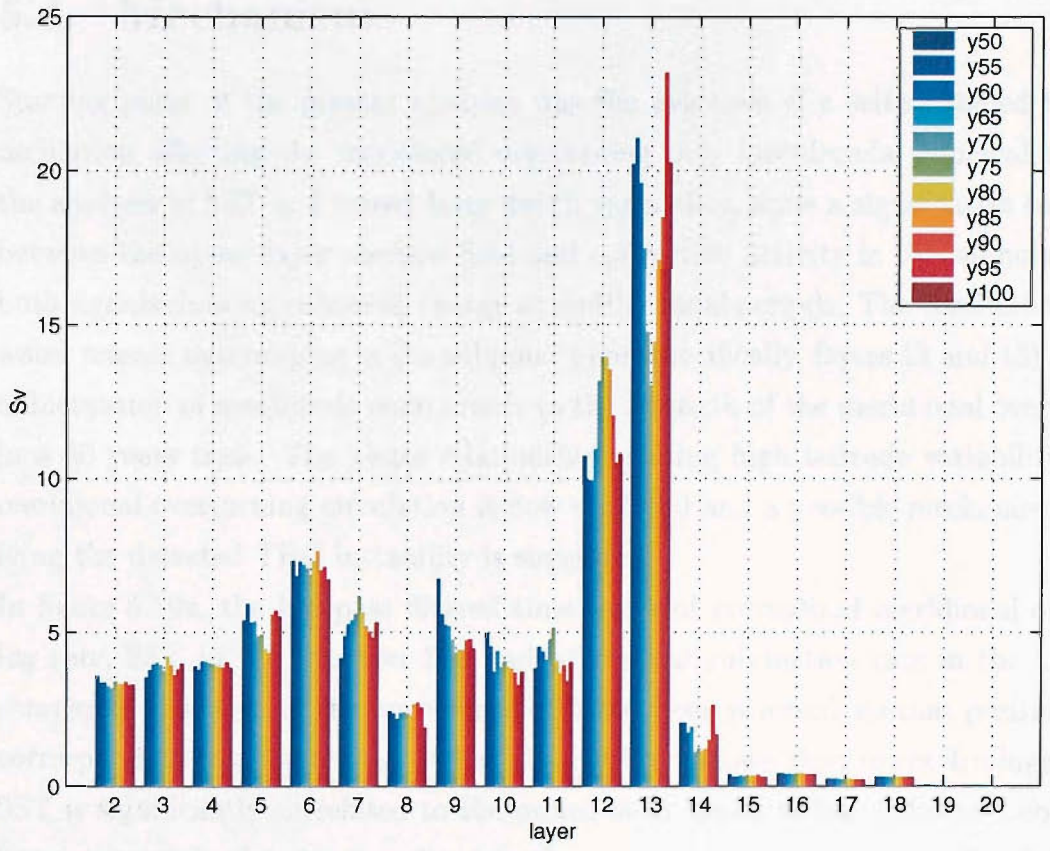

Figure 5.9: Permanent subduction rates (Sv) estimated for years 50 to 100. Values are 5 years spaced

the model Subtropical Mode Water, on layer 6 ($\sigma_0 = 26.52$), and LSW, lend a bimodal structure to the ventilation pattern, mirroring the main water mass formation processes taking place in the subtropical and subpolar basin, respectively. No overall significant variability is observed, except for the LSW, whose ventilation rate varies by as much as 10 Sv, comparable to the magnitude of the meridional overturning circulation. Layer 12 ($\sigma_0 = 27.64$) exhibits a smaller amplitude fluctuation, markedly anticorrelated to the one observed in the LSW. The LSW consitutes the upper limb of the model NADW, feeding the return deep flow of the THC through the Deep Western Boundary Current (DWBC). Whether and how strongly the variability in the LSW formation rate impinges on the strength of the meridional overturning, and what is the phase relationship linking together the identified variability patterns is the subject of the next section.

5.4 Mechanism

Starting point of the present analysis was the evidence of a self-sustained irregular oscillation affecting the meridional overturning over interdecadal timescales. From the analysis of SST and mixed layer depth variability, arose a significative coherency between the upper layer thermal field and convective activity in the subpolar basin, both signals showing enhanced energy at multidecadal periods. The ventilation rate of water masses outcropping in the subpolar gyre (specifically, layers 12 and 13) exhibits a fluctuation of magnitude comparable to the strength of the meridional overturning, in a 50 years time. The phase relationship relating high latitude variability to the meridional overturning circulation is now analysed and a possible mechanism underlying the detected THC instability is suggested.

In figure 5.10a, the low-pass filtered time series of normalized meridional overturning rate, SST in the Irminger Sea and permanent subduction rate in the LSW are compared. The sign of the normalized SST has been reversed, so that positive peaks correspond to cold anomalies. It has already been shown that in the Irminger basin, SST is significantly correlated to the mixed layer depth at lag 0 (figure 5.6b) so the latter time series has been omitted in the comparison as redundant. Subduction in

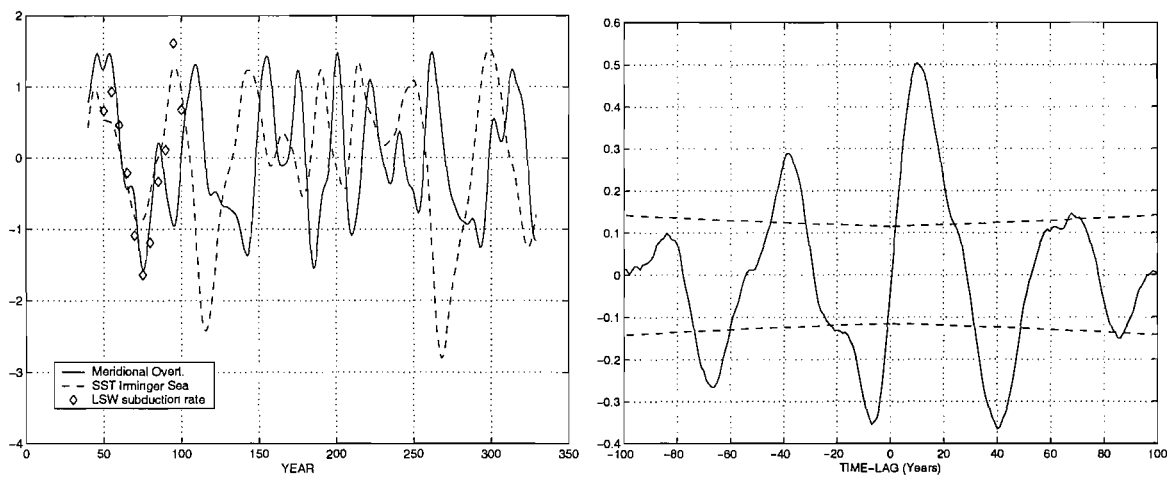

(a) (b)

Figure 5.10: (a)Normalized time series of meridional overturning streamfunction (solid), March SST in the Irminger basin (dashed) and subduction rate in the Labrador Sea Water (dots). The sign of the normalized SST was reversed, so that positive peaks correspond to cold anomalies. (b) Lagged correlation coefficients between SST in the Irminger Sea and meridional overturning rate. The dashed lines indicate the 95 % confidence limits.

the LSW appears to be in phase with the SST cycle, high(low) ventilation rates corresponding to a cold(warm) anomaly in the Irminger Sea SST cycle. Two timescales emerge from the lagged correlation between the high latitude SST and the meridional overturning (figure 5.10b). The SST leads the meridional overturning by 10 years. Significant negative correlation is also found at lag -9, indicating a 9 years delay between an anomolously high overturning and the appearance of a warm SST anomaly in the subpolar basin.

The existence of delays is essential to maintain a self-sustained oscillation. In order to fully understand the nature of the oscillatory behavior, the processes setting the magnitude of the delay need to be identified. The LSW is the isopycnic layer undergoing the largest amplitude subduction rate variability, and it is likely to convey equatorward anomalies associated with changes in the deep water formation rate. The role of advection in the transmission of signals from the convection region to subtropical latitudes along this limb of the THC is investigated by a tracer release experiment.

The ventilation tracer previously used for the estimate of permanent subduction rates, is re-initialised on year 60 and released in the mixed layer, and its age is computed for the following decade. The age of the tracer (τ) is governed by an advection-diffusion equation modified by a source term equal to unity, simulating the monotonic ageing process of a water mass:

$$\frac{\partial \tau}{\partial t} + \mathbf{v} \cdot \nabla \tau = \nabla \cdot (\kappa \nabla \tau) + 1 \tag{5.1}$$

Tracer age in the mixed layer is uniformly set to zero. In figure 5.11 the age of the LSW on year 69 is shown, corresponding to year 9 after the start of the experiment. The sources of LSW can be singled out from the minima in the age distribution, indicating regions of recently occurred ventilation. LSW formation mainly takes place in the Labrador Sea and off the Grand Banks of Newfoundland. Isolated sources can be identified in the Irminger Sea, and in the northeastern corner of the model domain. LSW formed in the western subpolar basin, ventilates the deep ocean via three main pathways: a zonal spreading route, penetrating the Irminger basin south of Cape Farewell (the southernmost tip of Greenland), a cyclonic branch following the deep NAC extension, and an equatorward route, spilling out of the subpolar basin along the western boundary. In a 9 years time, traced water trapped in the DWBC system

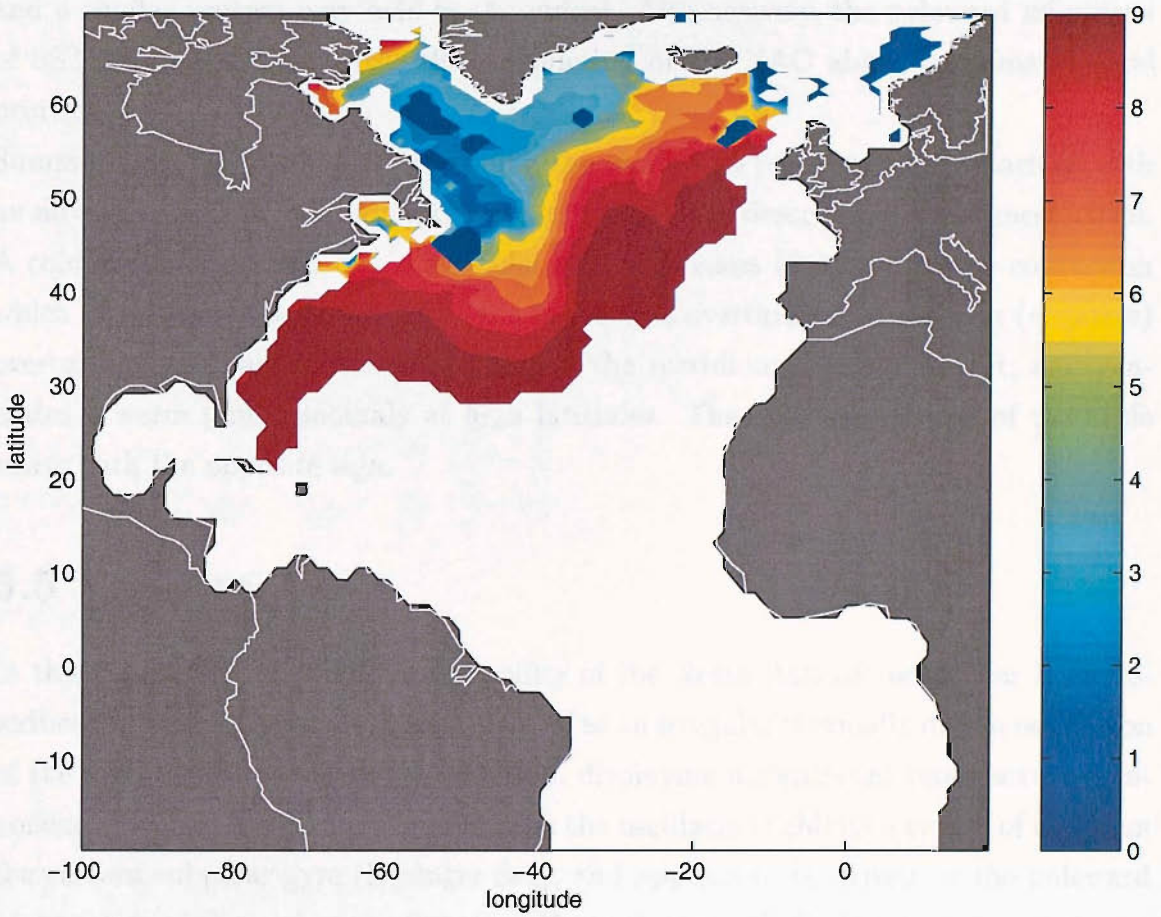

Figure 5.11: Tracer age (years) in the LSW, 9 years after the tracer initialization.

reaches as far as 20°N, whereas a slower diffusive transport ventilates the interior basin. The 10 years time-lag between SST in the subpolar basin and the overturning is consistent with the advective timescale associated with a water particle transported by the DWBC from the convection area (60°N) to the maximum overturning latitude (30°N) with an average velocity of 1 cm/s. The approximately 10 years timescale associated with the delayed response of SST in the deep water formation region to changes in the overturning strength is not consistent with an advective process occurring in the upper layer. As already mentioned, SST anomalies appear to propagate with a mean speed which is about one order of magnitude slower than the NAC flow. However, observations of SST anomalies propagating along the Gulf Stream/NAC path (*Hansen and Bezdek*, 1996) exhibit a similar discrepancy. *Sutton and Allen* (1997) suggest that the propagation speed of the anomalies may be determined by the "*...weaker currents either to one side of the core or at some depth below the core*",

and a similar process may hold in the model. Alternatively, the poleward migration of SST anomalies may reflect the meandering of the NAC about its climatological position.

Summarizing, the mechanism governing the oscillation bears strong similarities with an advective-convective feedback. Here is a schematic description of the mechanism. A cold (warm) anomaly in the subpolar basin increases (decreases) deep convection which in turn increases (decreases) the meridional overturning. A positive (negative) overturning anomaly increases (decreases) the meridional heat transport, and generates a warm (cold) anomaly at high latitudes. Then the second half of the cycle starts with the opposite sign.

5.5 Summary

In this chapter, a free mode of variability of the North Atlantic ocean has been described in detail. The mode manifests itself as an irregular thermally driven oscillation of the meridional overturning circulation, displaying a significant interdecadal component. The SST pattern associated with the oscillation exhibits a center of action in the eastern subpolar gyre (Irminger Sea), and appears to be driven by the poleward propagation of thermal anomalies along the path of the NAC. The coherency between anomalous SST and winter mixed layer depth fields in the Irminger Sea at lag 0 corroborates the idea that the lateral advection of SST anomalies in the subpolar basin modulates the high latitude convective activity. Thus, intermittency in the Irminger basin deep convection on interdecadal timescale appears to be caused by a merely non-local process, involving the large scale circulation. Deep convection variability imprints itself on the LSW subduction rate. The phase relationship between the high latitude upper layer variability and the multidecadal fluctuations of the meridional overturning reveals two delays, controlling the self-sustained oscillation. The first delay, associated with the 10 years time lag between the SST in the convection region and the maximum overturning, is consistent with the advective timescale set by the transport in the DWBC. The approximately 10 years delay between the meridional overturning and the high latitude deep convection is determined by the slow propagation of the SST anomalies across the subtropical/subpolar boundary.

Chapter 6

Forced variability. The ocean response to a NAO-like windstress forcing

In the previous chapter, a variability mode of the THC with a significant interdecadal signature, emerging under climatological forcing, low thickness diffusivity and high overturning conditions, was documented. The mode was found to be entirely due to internal dynamics involving essentially non-local processes. The existence of decadal and interdecadal scale variability in the unforced system motivates a further set of experiments - the subject of the present chapter - aimed to investigate the forced variability of the ocean under different levels of internal dissipation and atmospheric forcing periods. The windstress climatology is perturbed with a pattern reproducing the main features of the NAO, the dominant mode of atmospheric variability in the Atlantic sector.

6.1 Introduction

As pointed out in the introductory chapter, the NAO varies on a wide range of timescales. The ocean response may be more sensitive to those components of the forcing matching the same natural frequency. The presence of autonomous interdecadal oscillations in an ocean forced with climatology raises the interesting question of how such an ocean will respond to an atmosphere which varies at the same frequency of the ocean. A new set of experiments is designed aimed to investigate (i) the interac-

tion between the internal and externally forced variability, and the possible excitation of the natural oscillatory modes of the ocean, and (ii) how the forced ocean response is affected by the strength of eddy mixing, particularly when the natural frequency of the ocean matches that of the forcing. The free interdecadal mode, documented in chapter 5, displays a markedly non local character which is unambiguously revealed by the propagation of SST anomalies along the NAC path. In order to consistently excite the re-emergence of this mode, the windstress forcing is perturbed using an anomalous pattern reproducing the main features of the NAO. The wind stress in the current model configuration does not affect the latent and sensible heat fluxes as these are formulated through a SST relaxation boundary condition. Therefore, the wind stress perturbation does not imprint itself on the SST via the modulation of local air-sea fluxes, but only through the non linear interaction with the velocity field. On the other hand, heat fluxes perturbation has a two-fold effect on the SST: a local effect, related to the forcing/damping of SST anomalies by air-sea fluxes, and a non local one, which actively involves the ocean dynamics through the modulation of the buoyancy-driven circulation. By restricting the NAO-like fluctuations to the wind stress, a clear separation between local and non local forcing mechanisms is effected. The NAO-related synoptic wind stress fluctuations characterised by timescales shorter than a month, which typically influence the mixed layer deepening, have been neglected in this set of experiments. However, the mean impact of this process, parameterised by a climatological annual cycle of the third power of the friction velocity, u_* (defined in chapter 3), has been retained. Only the low frequency (decadal and interdecadal) variability of the NAO wind stress is simulated. The procedures used to extract the NAO-like wind stress perturbation, and to generate the forcing functions simulating the NAO long term variability are detailed in the next section.

6.2 Experimental setup

The atmospheric dataset used to compute the NAO-like windstress forcing was provided by the output of an atmospheric general circulation model, the HadAM2b version of the UK Meteorological Office Unified Model (*Stratton*, 1996), which has been shown to be able to capture much of the multidecadal variability and some interannual changes of the North Atlantic Oscillation, when forced with observed SST and sea-ice extent. Details on the model run which generated the atmospheric

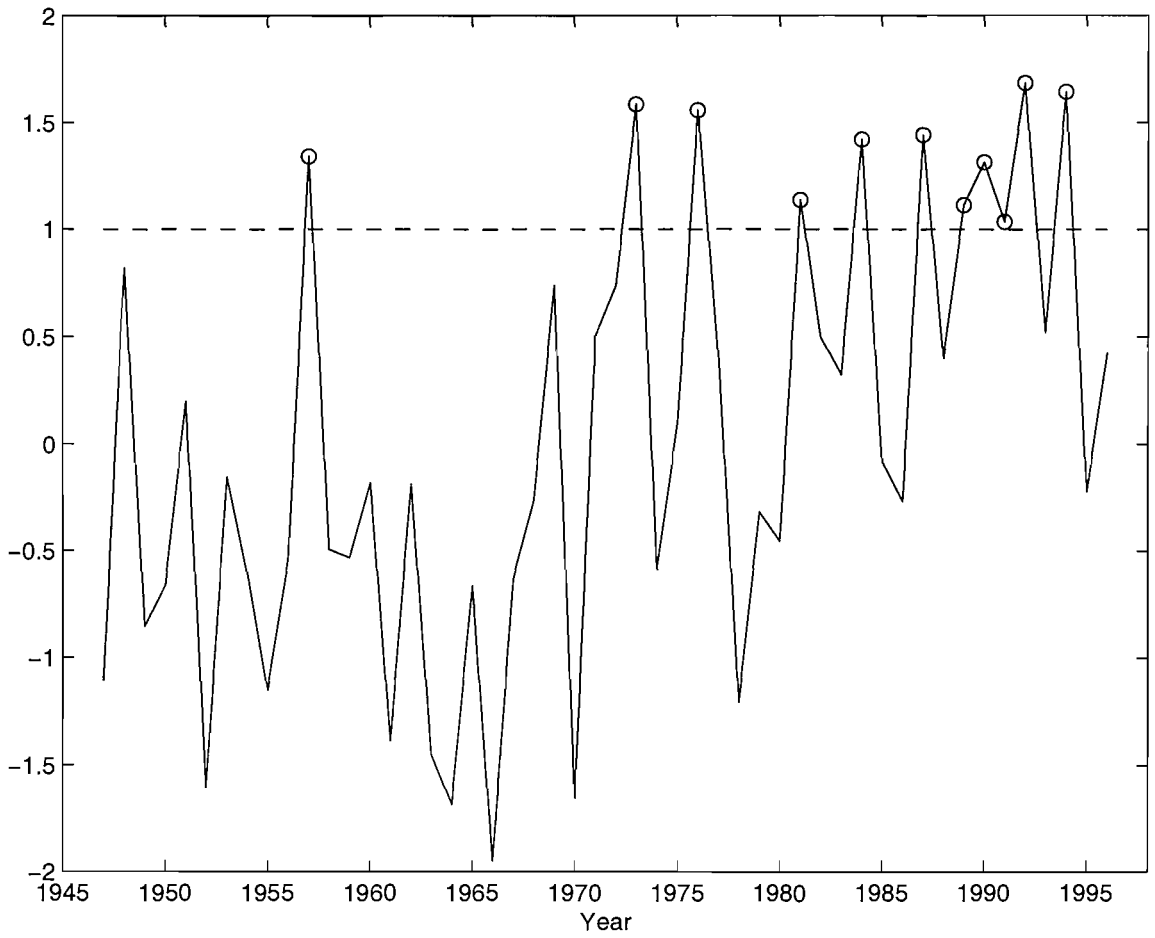

Figure 6.1: Winter (DJFM) NAOI calculated from the HadAM2b normalized SLP differences between Azores and Iceland, for the 1946/47-1995/96 winters. Plotted values refer to the year in which January occurs. Circles denote NAOI > 1 events.

dataset, can be found in *Rodwell et al.* (1999). From this *synthetic* dataset, covering the period from January 1946 to October 1996, the SLP winter (December to March) average was calculated for the period 1946/47 to 1995/96. An NAOI was calculated as the normalised SLP difference between the Azores and Iceland (figure 6.1). Normalization of the SLP difference was obtained by removing the mean and dividing by the standard deviation. A broad agreement with the observed NAOI can be noted. Particularly evident is the initial decreasing trend, turning in the early 70s into a prevailing positive NAO phase, with an associated increased frequency of NAOI > 1 events (*Hurrell*, 1995).

The calculation of the NAO windstress anomaly field was carried out using a composite analysis approach. In order to obtain the wind stress pattern corresponding to the positive phase of the NAO, the DJFM mean fields were averaged over the

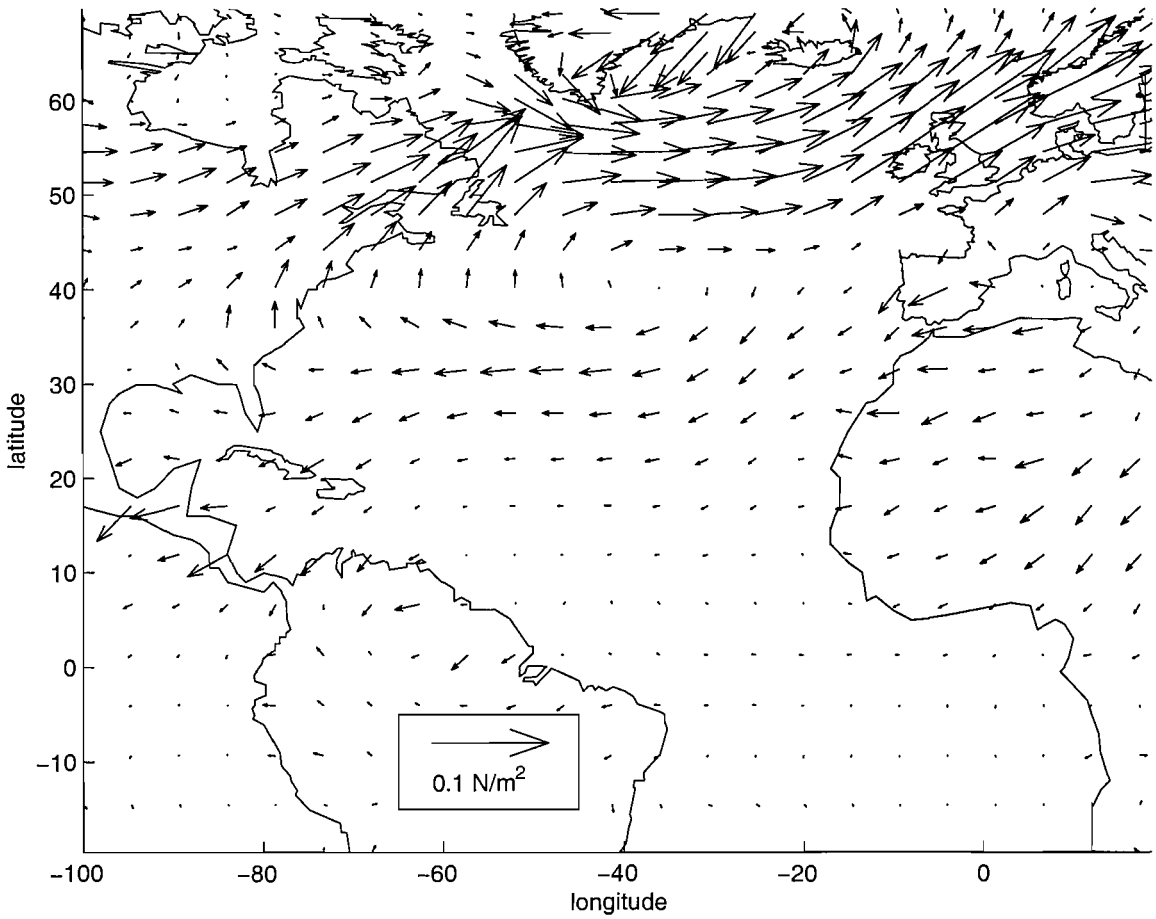

Figure 6.2: Windstress anomaly pattern (NAO positive phase)

years with an NAOI > 1 (highlighted in figure 6.1). The anomaly was then calculated by removing the mean computed over the all winters. The resulting pattern, corresponding to a positive phase of the NAO, is shown in figure 6.2. The westerlies intensification, and the associated weakening of the trade winds, fit relatively well the observational picture of the NAO (*Visbeck et al.*, 2003). The vorticity anomaly associated with the applied perturbation, during the positive (negative) phase, is an anticyclonic (cyclonic) torque, centered around 40°N.

The NAO-like windstress anomaly is added to the climatology only for the winter season, when the strength of the NAO signal achieves its maximum. In order to provide a smooth onset and offset of the NAO perturbation, the anomalous wind is modulated by a squared sine wave during the forcing season. A further sine wave modulation is required to simulate the low frequency (decadal and multidecadal) variability of the NAO. Results from the unforced experiments have shown that spontaneous variability arises in the model on a wide range of timescales. Enhanced energy

emerges at decadal and interdecadal timescales, when sufficiently low diffusivity and high MO (which in turn implies a strong meridional overturning) are used. Within the spectrum of the model internal variability, two timescales, 10 and 50 years long, are selected as forcing periods to simulate the low frequency modulation of the NAO-like perturbation. Enhanced energy in the 10 years range (*Hurrell and van Loon*, 1997) and on multidecadal timescales (*Cook et al.*, 1998) also emerges in the observed NAO power spectra. An example of the forcing function for a 10 years period is shown in figure 6.3. The decadal and interdecadal modulations are separately applied to the NAO anomaly in two distinct experiments, which is equivalent to assume a *monochromatic* NAOI.

In order to assess how the oceanic response to the NAO-like windstress forcing depends on the mixing strength, each experiment has been performed under both low (u_d = 0.1 cm/s) and high (u_d = 1.0 cm/s) thickness diffusivity conditions. Experiments I01 and I1 (IMED ensemble), are selected as the control runs for the low and high diffusion NAO experiments, respectively. The NAO anomalous forcing is applied starting from the ocean state corresponding to the model year 100 of the related control run. The steady states achieved by experiments I01 and I1 have been described in chapter 4. The characteristics of the performed experiments are summarized in table 6.1. From now on, we will refer to this set of numerical integrations as the NAO experiments.

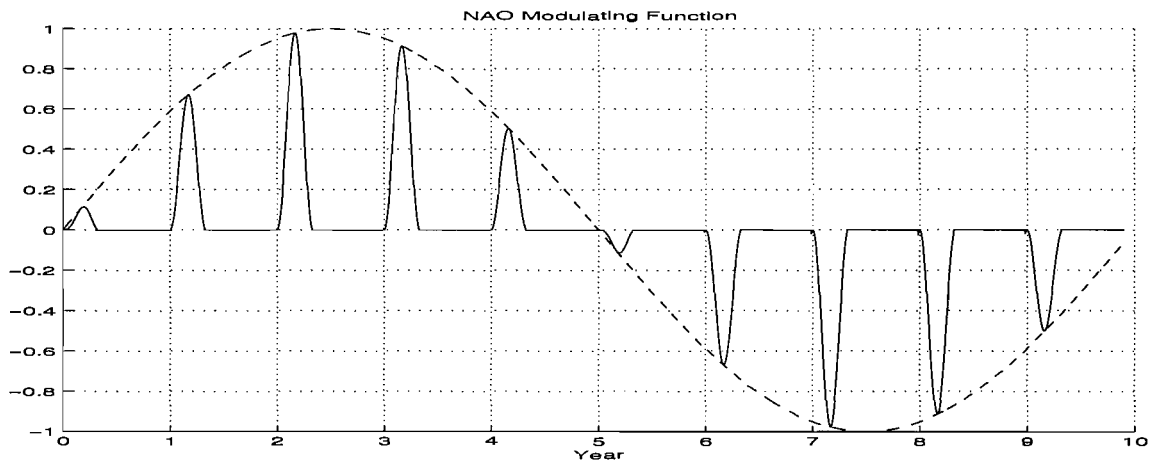

Figure 6.3: Amplitude of the NAO anomaly for a 10 years forcing period. Notice that the time axis has been partitioned into annual intervals starting on the first of December, so as to include the wintertime NAO perturbation into one single year cycle. The dashed line indicates the envelope of the decadal modulation. The NAO perturbation is only applied during the winter season. When the forcing level is zero, only climatology is applied.

Experiment	Thickness Diffusion at the Equator (m^2/s)	NAO Period ($years$)	Mediterranean Outflow (Sv)	Initial Cond. (year 100)
N10LOW	150	10	7.5	I01
N10HIGH	1500	10	7.5	I1
N50LOW	150	50	7.5	I01
N50HIGH	1500	50	7.5	I1

Table 6.1: Summary of parameter values used in the NAO-like windstress experiments.

6.3 Sea surface temperature variability

The spatial structure of sea surface temperature variability for the NAO experiments is diagnosed through the SST standard deviation. The corresponding patterns are shown in figure 6.4. All the experiments show maximum variability in the NAC region, with the centres of action for the weakly diffusive oceans appearing to be located slightly southeast compared to the high diffusion experiments. A smaller amplitude structure is also evident in the western subtropical gyre, with the only exception for the experiment N10HIGH. In order to get a quantitative estimate of the ocean response as a function of diffusivity and forcing period, the average SST standard deviation has been computed over two regions, corresponding to the eastern subpolar gyre/NAC (50°-64°N, 48°-21°W) and western subtropical gyre/Gulf Stream (18°-52°N, 75°-47°W). The selected regions encompass the foci of the upper layer variability (see figure 6.4, upper left panel). In order to remove the spurious variability associated with model drifts, caused by an uncomplete model spin-up, SST values have been linearly detrended prior to the calculation of the standard deviation. The existence of residual drifts in the NAC upper layer temperature, is particularly evident in the control experiment I01 (figure 4.6), and it is likely to affect the low diffusivity NAO experiments. However, caution is needed in the interpretation of detrended data, as detrending may introduce some degree of distortion, particularly due to the somewhat arbitrary a priori assumption of linearity made on the model drift. Table 6.2 summarizes the regional averages of March SST standard deviation for each experiment, with and without detrending.

Enhanced variance is detected in both the subtropical and subpolar areas when a 50 years forcing period is used. The maximum oceanic response is achieved in the subpolar region, when low diffusivity and interdecadal forcing conditions are simulta-

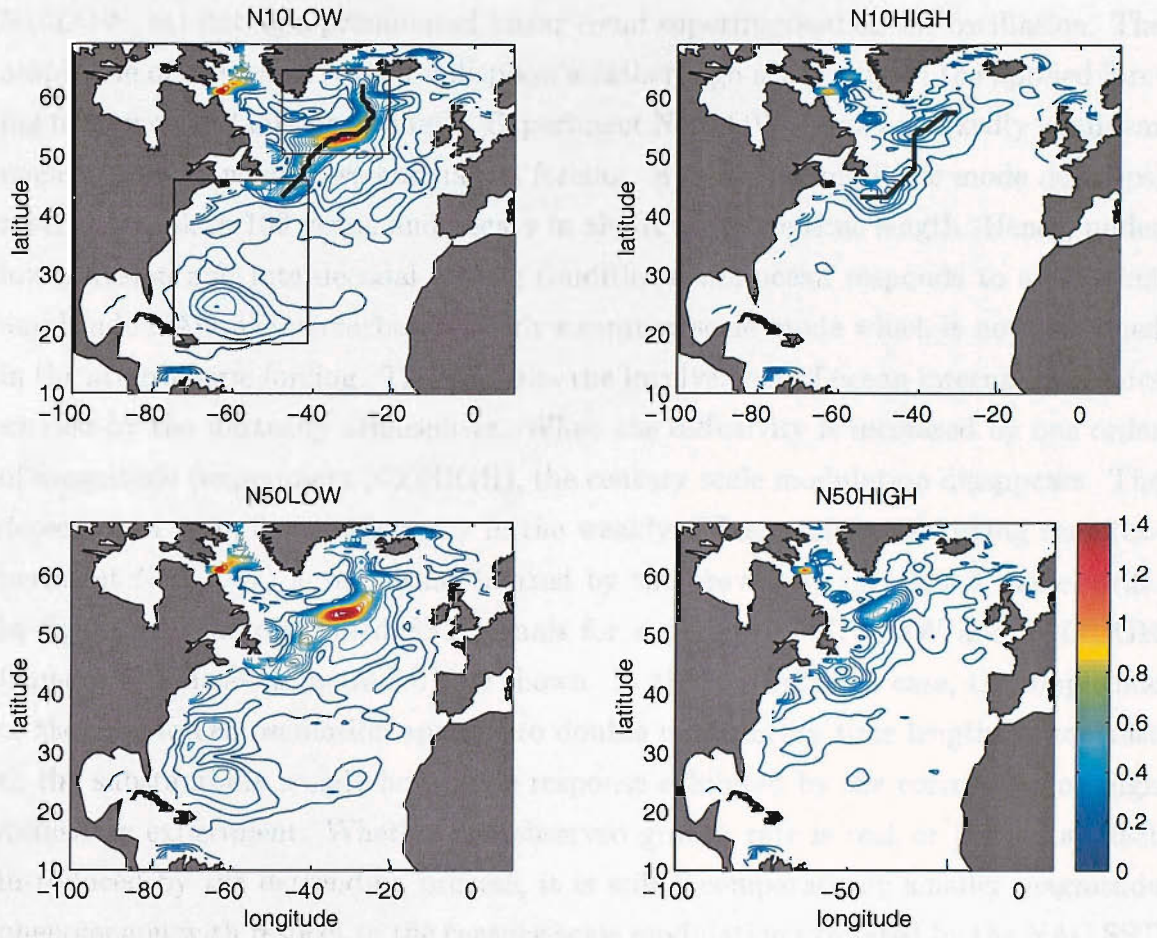

Figure 6.4: Standard deviation of March SST computed for experiments N10LOW (upper left), N10HIGH (upper high), N50LOW (lower left), N50HIGH (lower right). The regions selected for the computation of the basin-averaged SST standard deviation are indicated in the upper left panel. The tracks used for the calculation of SST anomaly Hovmüller diagrams, for the low and high diffusivity experiments are shown in the upper left and right panels, respectively.

neously applied (experiment N50LOW). Increasing the mixing strength by one order of magnitude produces a factor of 2-3 decrease in the SST standard deviation for all the experiments. As expected, detrending mostly affects the SST variability signal in the subpolar region, under low diffusivity conditions, while no sensible changes are detected in the subtropical region, and for high diffusivities. Overall, results appear to be qualitatively unaffected by detrending.

The temporal evolution of SST in locations selected within the maximum variability areas of each experiment (see figure 6.4) are shown in figure 6.5. Time series have been low pass filtered with a 5 year cut-off period, in order to emphasize the decadal and lower frequency components. The SST variability appears to be driven by the NAO periodicity in all the performed experiments, with the only exception of experiment

N10LOW, exhibiting a pronounced linear trend superimposed on the oscillation. The amplitude of the ocean response displays a rather high sensitivity to the applied forcing frequency and mixing strength. Experiment N50LOW shows a markedly nonlinear response to the windstress anomalous forcing. A growing amplitude mode develops, reaches a peak in 150 years, and decays in about the same time length. Hence, under low diffusion and interdecadal forcing conditions, the ocean responds to a constant amplitude NAO-like perturbation, with a century scale mode which is not contained in the atmospheric forcing. This suggests the involvement of ocean internal dynamics excited by the unsteady atmosphere. When the diffusivity is increased by one order of magnitude (experiment N50HIGH), the century scale modulation disappears. The detection of a similar nonlinearity in the weakly diffusive 10 years forcing case (experiment N10LOW) is somewhat blurred by the previously mentioned model drift. In figure 6.6, the detrended SST signals for experiments N10LOW and N10HIGH (same locations as in figure 6.5) are shown. In the low diffusion case, the amplitude of the SST forced oscillation appears to double in a century time length, in contrast to the substantially steady amplitude response exhibited by the corresponding high diffusivity experiment. Whether the observed growth rate is *real*, or just an artifact introduced by the detrending process, it is still a comparatively smaller magnitude phenomenon with respect to the century scale modulation exhibited by the NAC SST in the weakly dissipative interdecadal forcing experiment. The existence of processes occurring over multi-century timescales, however, cannot be established, due to the relatively limited time length of this particular model integration. By comparing the SST time series obtained from the high diffusivity experiments, it emerges that the

Diffusion	Subtropical Gyre/ Gulf Stream	Subpolar Gyre/ NAC	Forcing Period (years)
LOW	0.14 (0.15)	0.29 (0.34)	10
HIGH	0.05 (0.05)	0.09 (0.09)	
LOW	0.18 (0.19)	0.30 (0.36)	50
HIGH	0.08 (0.08)	0.12 (0.13)	

Table 6.2: March SST standard deviation (in ^oC) averaged over the subtropical gyre/GS and the subpolar gyre/NAC regions as a function of thickness diffusivity and forcing period. LOW and HIGH refer to the thickness diffusion velocity (0.1 and 1.0 cm/s, respectively). Data have been detrended prior to the computation of the standard deviation. The corresponding standard deviation for not detrended data is also shown in brackets.

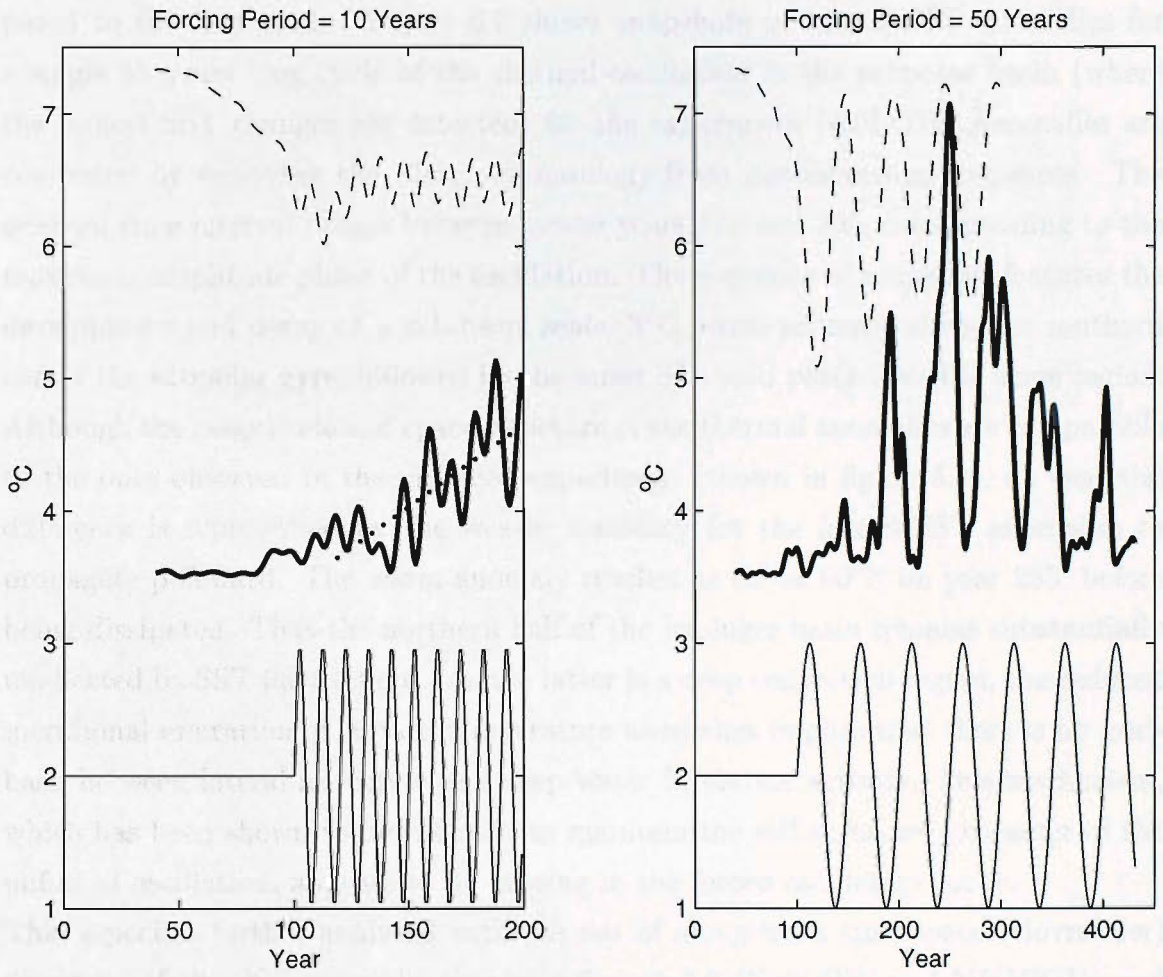

Figure 6.5: Left panel: SST for the experiments I01-N10LOW (solid thick) and I1-N10HIGH (dashed), in 35°W,55°N, and 40°W,54°N respectively. Years 40 to 99 refer to the control runs I01 and I1. The NAO-like perturbation is switched on at year 100. The dots indicate the linear trend computed for the experiment N10LOW. The phase of an arbitrary amplitude NAO forcing (solid thin) is also shown. Right panel: same as in left panel, but for the experiments I01-N50LOW (solid thick) and I1-N50HIGH (dashed).

50-years forcing excites a factor of 4 larger amplitude oscillation with respect to the decadal forcing experiment. Also, the onset of the NAO perturbation appears to rectify a residual trend visible in the control run. The enhanced SST response to an interdecadal forcing, found under both low and high diffusivity conditions, together with the existence of a 50 years cycle in the unforced system, point to this particular period as a preferred timescale of the model ocean. The nature of the high latitude SST variability pattern associated with the free interdecadal mode (figure 5.1) has been traced back to the propagation of thermal anomalies along the path of the NAC (experiment H01, figure 5.3). The forced interdecadal SST oscillation is now com-

pared to the free mode. Figure 6.7 shows snapshots of March SST anomalies for a single 55 years long cycle of the thermal oscillation in the subpolar basin (where the largest SST changes are detected) for the experiment N50LOW. Anomalies are computed by removing the March climatology from instantaneous snapshots. The selected time interval ranges between model years 210 and 265, corresponding to the maximum amplitude phase of the oscillation. The sequence of snapshots features the development and decay of a sub-basin scale, 3^oC warm anomaly along the southern rim of the subpolar gyre, followed by the onset of a cold patch over the same region. Although the magnitude and space structure of the thermal anomalies are comparable to the ones observed in the unforced experiment (shown in figure 5.3), an essential difference is represented by the weaker tendency for the forced SST anomalies to propagate poleward. The warm anomaly reaches as far as 60^oN on year 255, before being dissipated. Thus the northern half of the Irminger basin remains substantially unaffected by SST fluctuations. As the latter is a deep convection region, the reduced meridional migration of surface temperature anomalies implies that there is no feedback between lateral advection and deep water formation activity. This mechanism, which has been shown to be essential to maintain the self-sustained character of the unforced oscillation, appears to be missing in the forced oscillatory mode.

This aspect is further analysed with the use of along-track time-space (Hovmüller) diagrams of the SST anomaly, shown in figures 6.8 (N50LOW and N50HIGH) and 6.9 (N10LOW and N10HIGH). Two distinct tracks have been selected for the low and high diffusion simulations, as the associated variability patterns are considerably

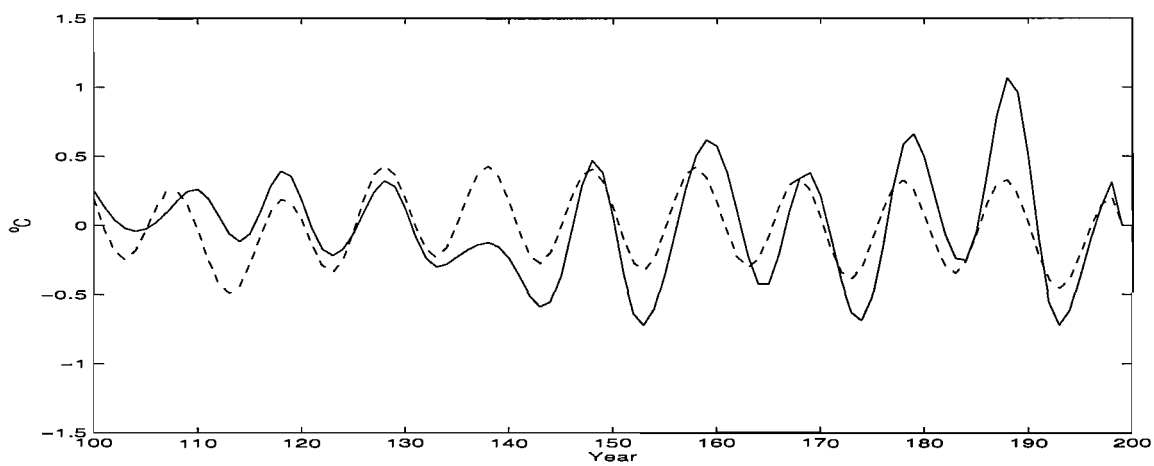

Figure 6.6: Detrended SST for the experiments N10LOW (solid) and N10HIGH (dashed) in 35^oW,55^oN and 40^oW,54^oN respectively.

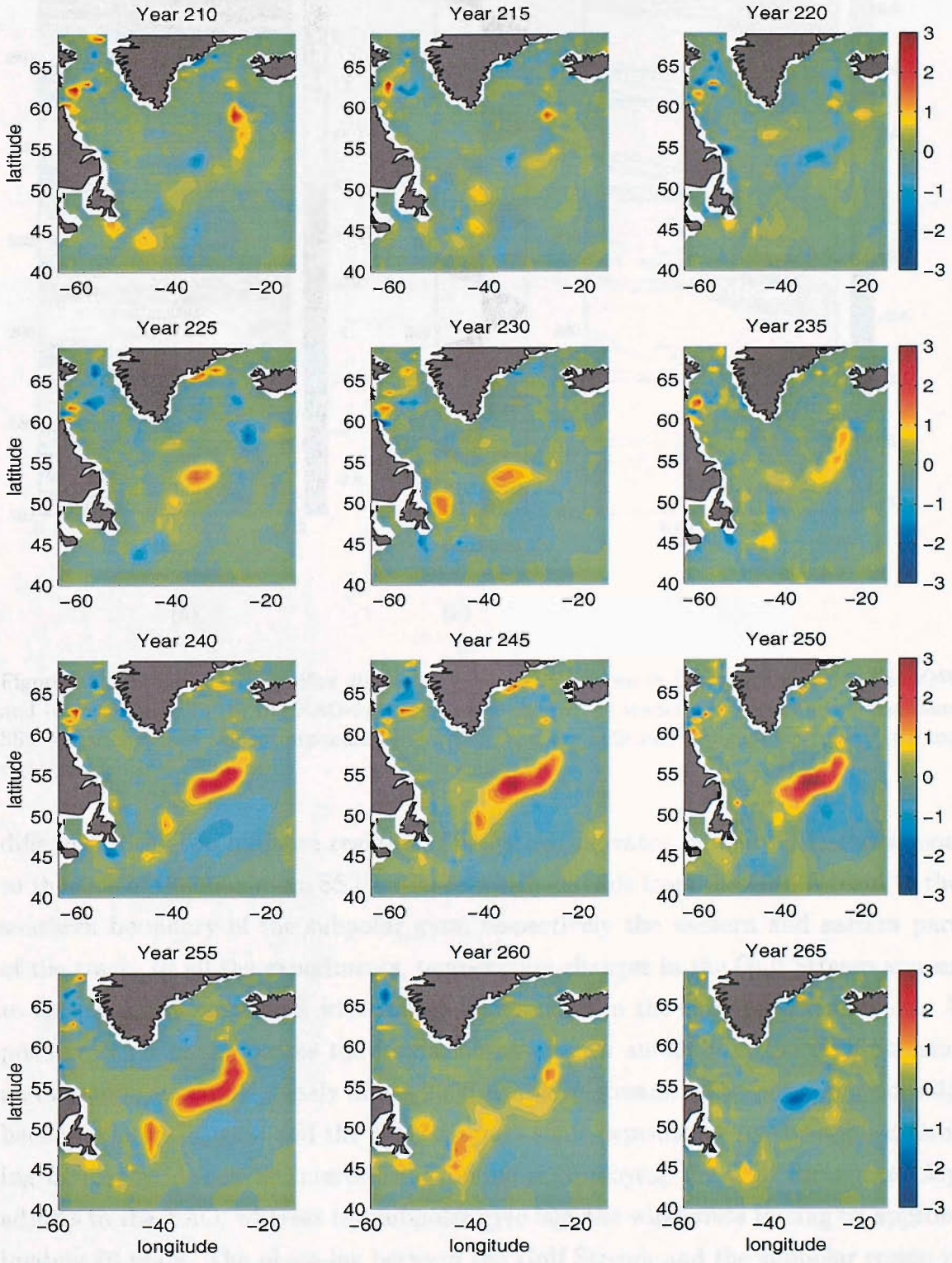

Figure 6.7: Anomalies of March SST (March climatology has been removed) from year 210 to year 265 for the experiment N50LOW. The time spacing between each snapshot is 5 years.

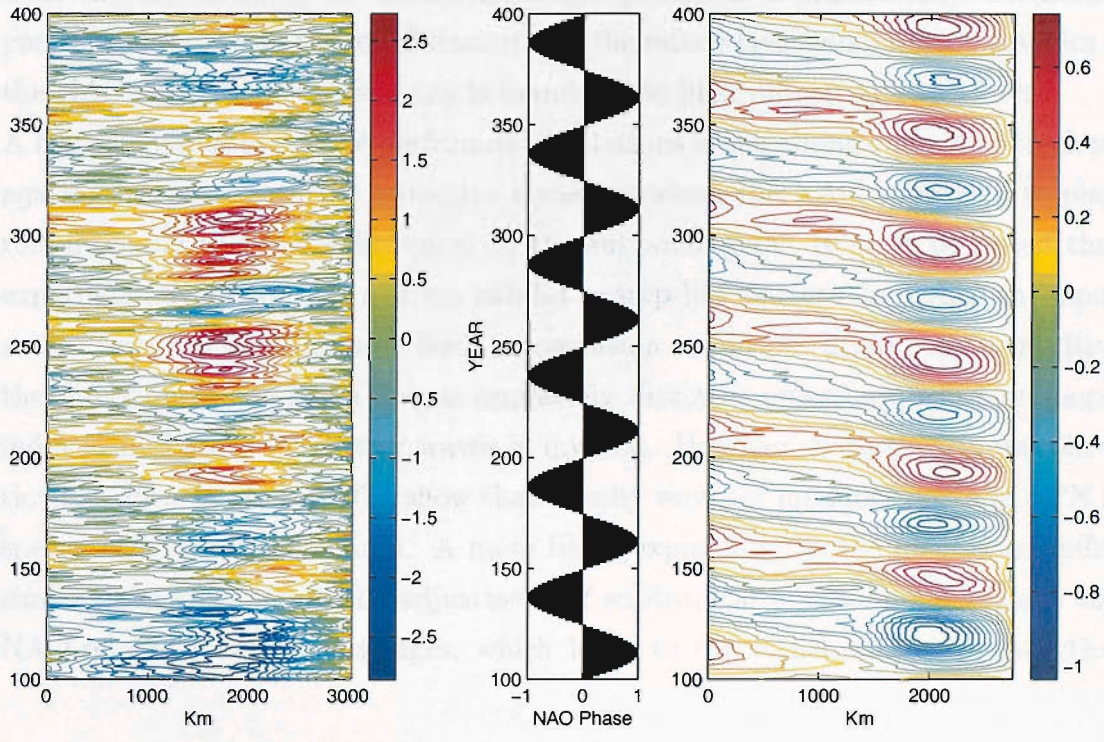

(a) (b) (c)

Figure 6.8: Along-track Hovmüller diagrams of March SST anomaly for experiments (a) N50LOW and (c) N50HIGH. In (b) the NAO-forcing phase is shown.The tracks coincide with the maximum SST variance axis of the corresponding simulation, and are indicated in figure 6.4 (upper left and right panels).

different in the two diffusive regimes. The paths (indicated in figure 6.4) correspond to the axis of the maximum SST variance which extends from the Gulf Stream to the southern boundary of the subpolar gyre, respectively the western and eastern part of the track. In all the experiments, temperature changes in the Gulf Stream appear to be negatively correlated with the SST anomalies in the subpolar gyre region. A positive NAO phase excites the formation of a warm anomaly in the Gulf Stream, and an opposite sign anomaly about 2000 Km downstream. The phase relationship between the SST signal and the NAO displays some dependence on the applied forcing frequency. When an interdecadal forcing is employed, the Gulf Stream quickly adjusts to the NAO, whereas the subpolar gyre lags the windstress forcing by approximately 10 years. The phase-lag between the Gulf Stream and the subpolar region is particularly evident in the high diffusivity simulation. Under a decadal forcing, the southern and northern halves of the track are almost in anti-phase as can be inferred

from the alignment of the isotherms, which generates a characteristic checkerboard pattern. However, in the low diffusion case the mixed layer temperature covaries with the NAO, whereas a 1 year delay is found in the high diffusivity experiment.

A feature shared by all the performed simulations is the absence of along-track propagating features, with the advective transport along the NAC appearing to play no role in connecting the subtropical to the subpolar gyre. It must be noted that in experiment N50HIGH, isotherms exhibit a step-like pattern implying an apparent south-westward propagation. Such a conclusion would be rather counterintuitive as the direction of the mean flow is oppositely directed, unless westward propagation induced by baroclinic Rossby waves is invoked. However, both theory and observations (*Killworth et al.*, 1997), show that Rossby waves at latitudes north of 50°N have speeds close to the zero limit. A more likely explanation is the mentioned different timescale characterising the adjustment of subtropical and subpolar regions to the NAO-related windstress changes, which leads to the rather artificial connection of

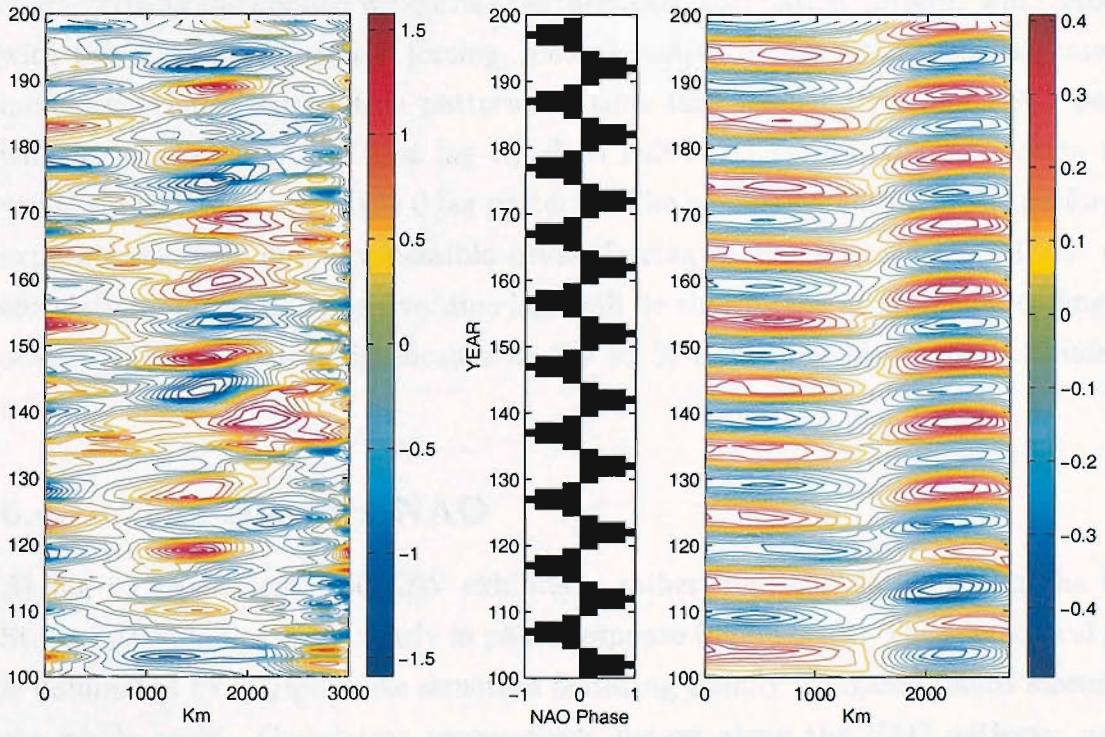

Figure 6.9: Same as in figure 6.8 but for experiments (a) N10LOW and (c) N10HIGH. In (b) the NAO-forcing phase is shown. Detrending has been applied to N10LOW data.

the isotherms in the Hovmüller diagram.
In the next section, a correlation analysis is used to evaluate the phase relationship between the NAO forcing and the upper ocean temperature.

6.4 Correlation analysis

Along-track SST anomaly patterns reveal a clear NAO signature in the upper ocean, with thermal anomalies having typical magnitudes of 1^oC. The NAC-subpolar gyre response appears to be delayed with respect to the Gulf Stream-subtropical gyre, when a 50 years NAO forcing is applied, whereas no phase shift is detected under a 10 years NAO forcing. In order to better illustrate how the atmosphere forces the ocean and eliminate any dependency on the selected track, correlation maps are calculated of the SST with the NAOI, which in these idealized experiments is a simple sine wave. The correlation analysis will identify the spatial patterns excited by the imposed atmospheric forcing at different time lags (in years). Due to the strong autocorrelation characterizing the applied windstress perturbation, correlation patterns will reemerge with the same period of the forcing, loosing statistical significance as the time lag increases. Hence, correlation patterns at time lags smaller than half NAO period will be considered (for a time lag equal to half NAO period, the correlation map yields a negative image of the 0 lag pattern). The uncoupled nature of the performed experiments rules out any possible ocean forcing of the atmosphere. Thus, only correlation patterns at positive time lags will be shown (the atmosphere leading the ocean). The statistical significance at the 99 % level is verified using a Student's t-test.

6.4.1 The 50-years NAO

At lag 0, experiment N50LOW exhibits a rather high correlation along the Gulf Stream path, indicating a nearly in phase response (figure 6.10). The subtropical gyre is dominated by a tripole-like structure featuring zonally elongated bands stretching the whole basin. Correlation progressively decays along the NAC pathway, and a considerably weaker correlation characterizes the subpolar gyre area. No significant correlation is found in the zonal belt centered around 20°N. The equatorial region displays a response in phase with the anomalous windstress forcing. This feature, indicating the rapid adjustment of the equatorial region to a windstress change, is

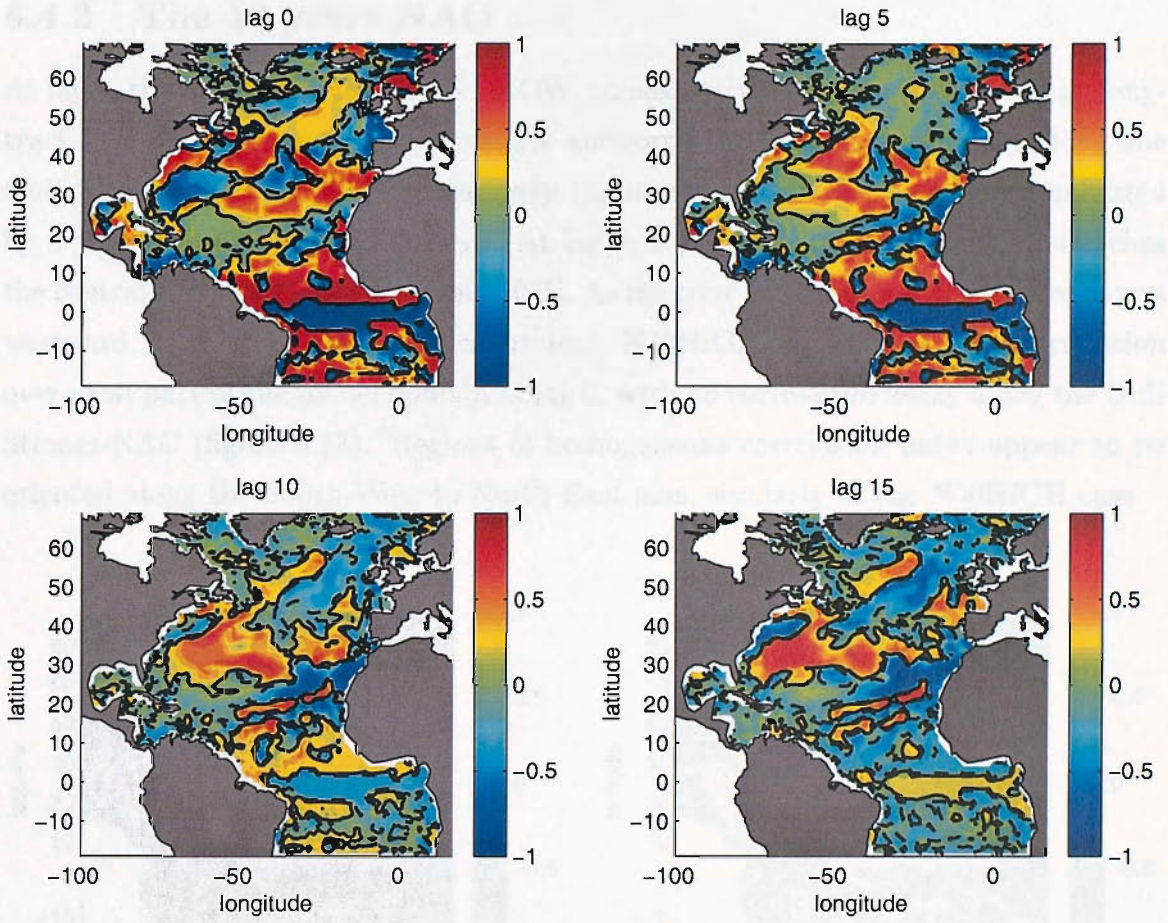

Figure 6.10: Local correlations between the NAOI and march SST for the experiment N50LOW at different time lags (in years). Correlations significant at the 99 % confidence level are enclosed by a black solid (dashed) line for positively (negatively) correlated regions.

shared by all the experiments and it will not be analysed further. At lag 10 a correlation pattern connecting the NAC with the inner subtropical gyre begins to emerge, reaching a peak at lag 15. This result confirms the existence of a phase shift between the Gulf Stream and the NAC, previously detected in the corresponding along-track SSTA diagram. The higher diffusivity case, N50HIGH, reveals at the 0 lag a pattern bearing strong similarities with the low diffusion twin experiment (figure 6.11). As in this latter case, the correlation index gradually decays along the Gulf Stream-NAC path, and a tripole structure dominates the subtropical region. At lag 10, a high latitude correlation pattern characterized by a zonal dipole in the subpolar basin emerges. This feature reaches a maximum amplitude at lag 15, when simultaneous high correlation in the subtropical basin also appears.

6.4.2 The 10 years NAO

At lag 0, the low diffusivity case N10LOW, consistently with the corresponding along-track SST anomalous pattern, exhibits anticorrelated changes occurring along the Gulf Stream and the NAC, respectively (figure 6.12). Mid-latitudes are dominated by a westward propagating pattern. At lag 0, a positive correlation signal stretches the central subtropical basin around 30°N. As the time lag increases this feature moves westward. The high diffusivity experiment, N10HIGH, shows very high correlation over most part of the model domain at lag 0, with no correlation decay along the Gulf Stream-NAC (figure 6.13). Regions of homogeneous correlation index appear to be oriented along the South-West to North-East axis, similarly to the N50HIGH case.

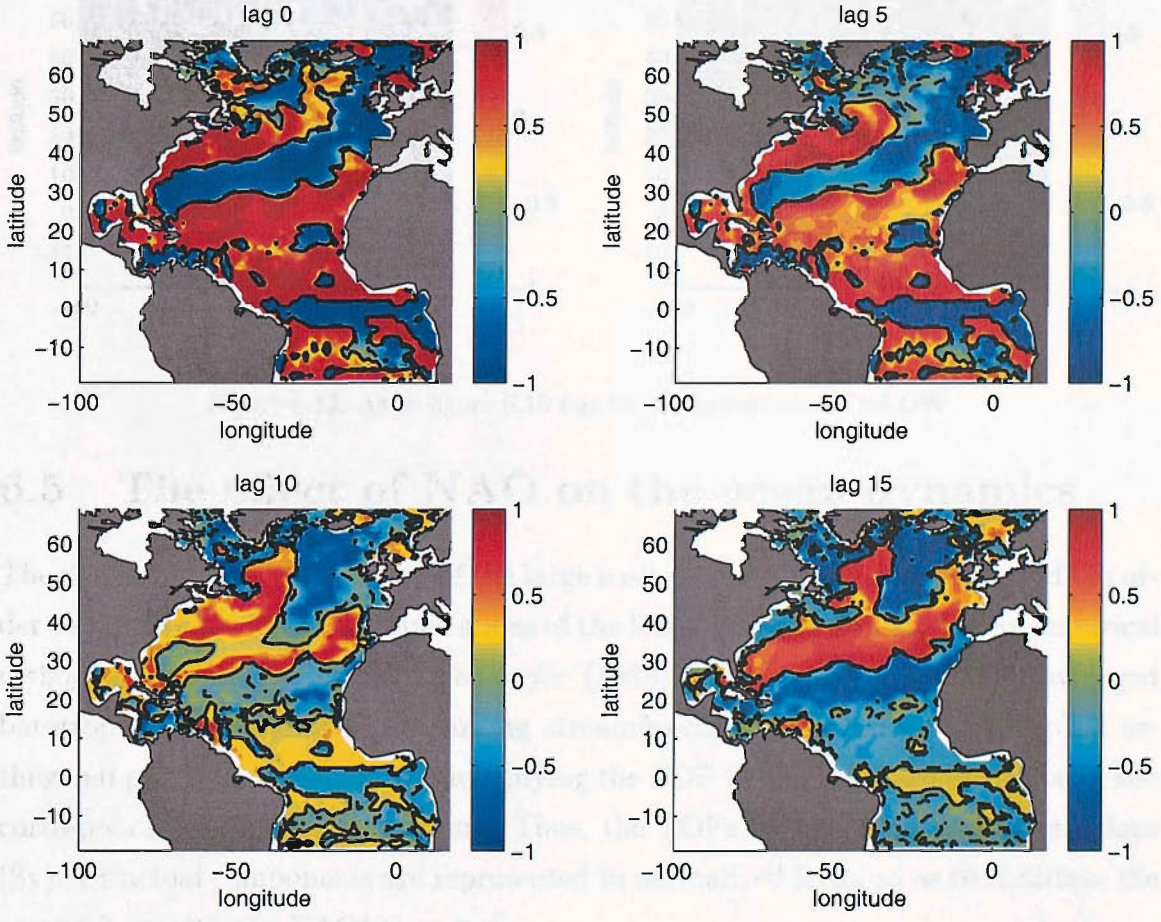

Figure 6.11: As in figure 6.10 but for the experiment N50HIGH.

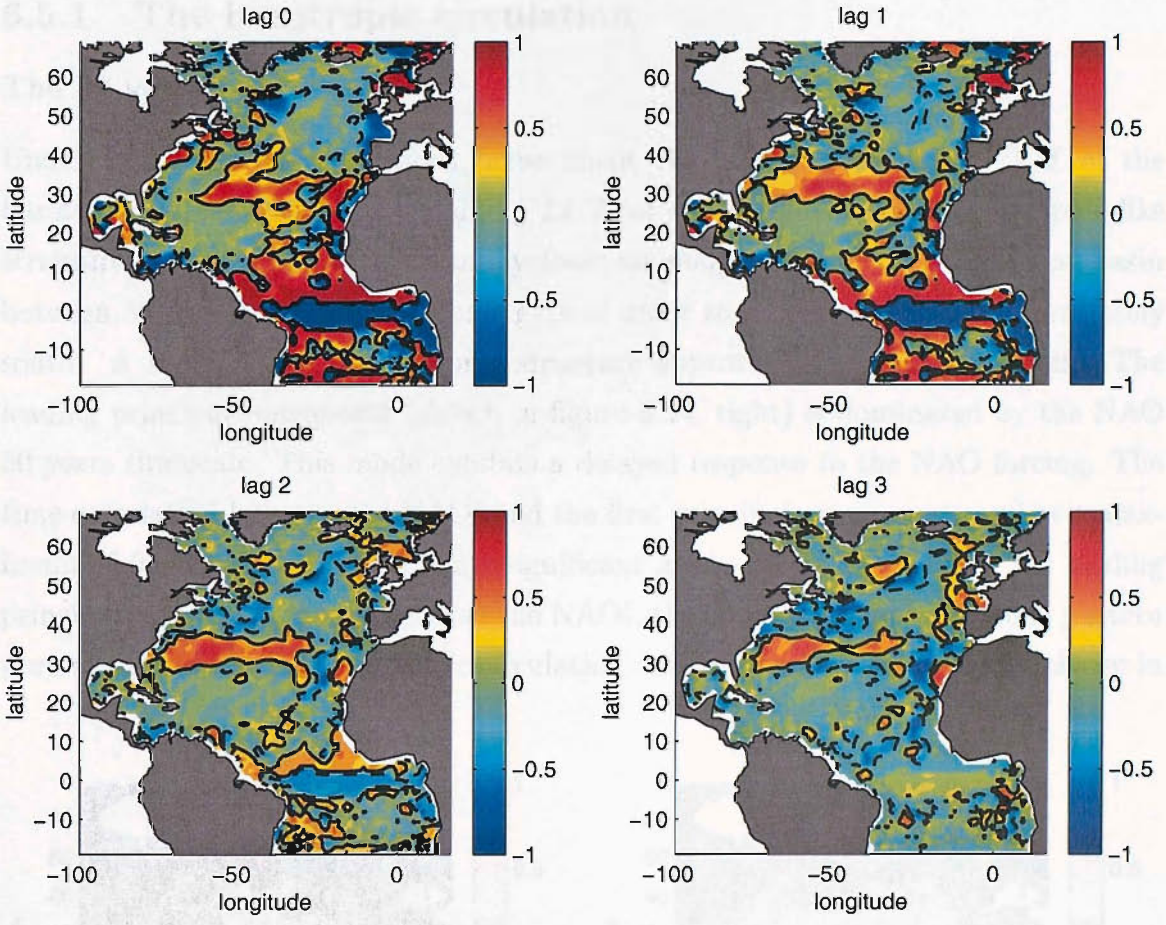

Figure 6.12: As in figure 6.10 but for the experiment N10LOW.

6.5 The effect of NAO on the ocean dynamics

The dominant variability modes of the large scale circulation are now inspected. In order to identify the space and time scales of the leading circulation modes, an empirical orthogonal function (EOF; *Preisendorfer* (1988)) analysis of the annually averaged barotropic and meridional overturning streamfunction is performed . A typical orthogonal pattern is obtained by multiplying the EOF by the standard deviation of the corresponding principal component. Thus, the EOFs will have physical dimensions (Sv). Principal components are represented in normalized form, so as to facilitate the comparison with the NAOI time series.

6.5.1 The barotropic circulation

The 50 years NAO

Under low diffusivity conditions (experiment N50LOW), the leading EOF of the barotropic streamfunction, explaining 24 % of the variance, features a tripole-like structure (figure 6.14, left). An anticyclonic anomaly stretches the subtropical basin between 30 and 50°N, and a cyclonic gyre of lesser zonal extent appears immediately south. A minor amplitude cyclonic structure appears in the subpolar basin. The leading principal component (shown in figure 6.14, right) is dominated by the NAO 50 years timescale. This mode exhibits a delayed response to the NAO forcing. The time correlation between the NAOI and the first principal component reaches a maximum of 0.9 for a 4 years time-lag, significant at the 99 % level. Since the leading principal component closely mirrors the NAOI, the corresponding orthogonal pattern portrays the anomalous barotropic circulation during a positive NAO phase (shown in

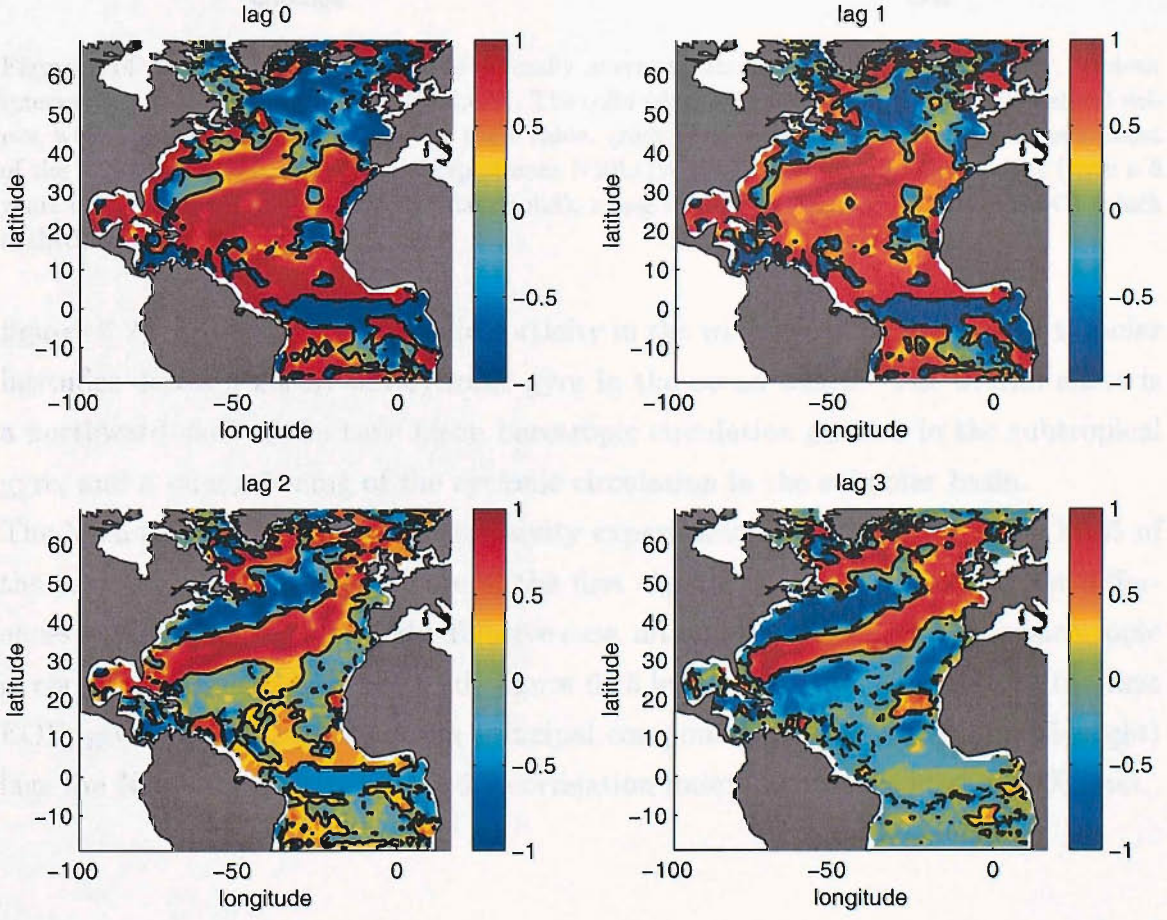

Figure 6.13: As in figure 6.10 but for experiment N10HIGH.

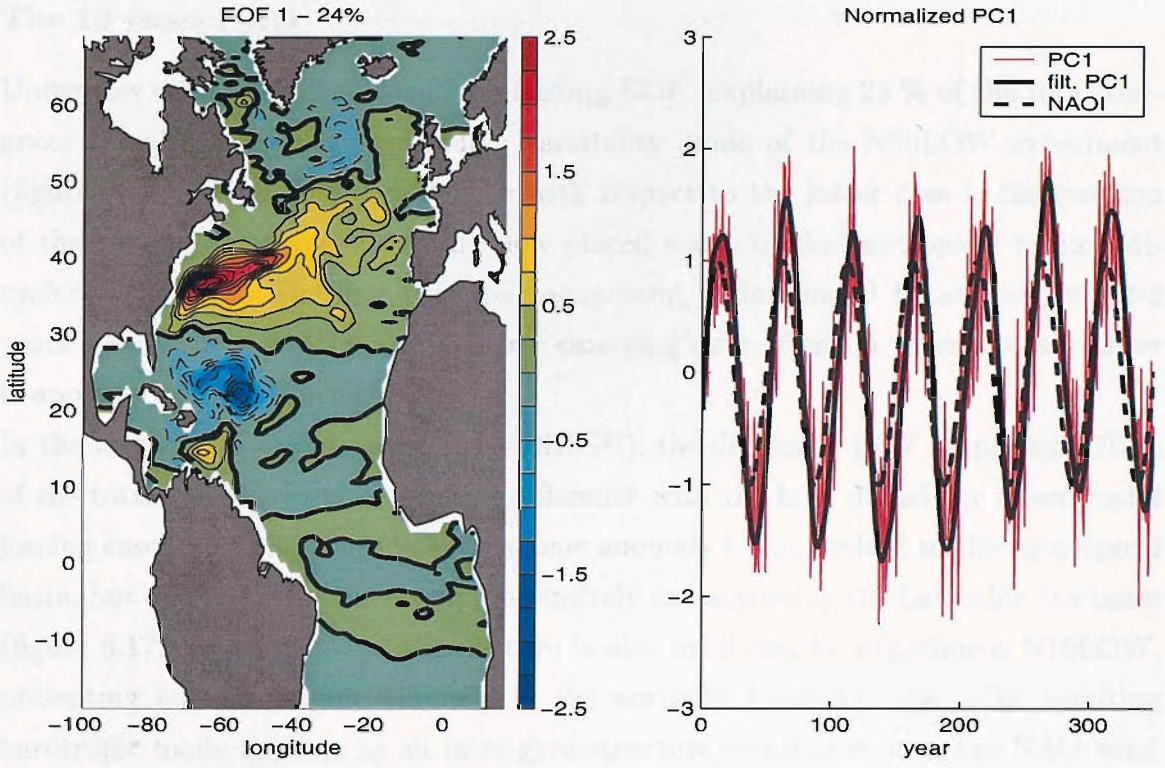

Figure 6.14: (left) Leading EOF of the annually averaged barotropic streamfunction (Sv; contour interval = 0.25 Sv) for experiment N50LOW. The solid (dashed) lines denote positive (negative) values, whilst the thick solid line indicates the 0 value. (right) Normalized leading principal component of the barotropic streamfunction for experiment N50LOW (red). Low pass filtered values (with a 5 years cut-off period) are also shown (black solid), along with the normalized 50 years NAOI (black dashed).

figures 6.2). Enhanced anticyclonic vorticity in the windstress forcing at mid-to-polar latitudes drives a 2.5 Sv anticyclonic gyre in the ocean below. The overall effect is a northward shift of the time mean barotropic circulation pattern in the subtropical gyre, and a strengthening of the cyclonic circulation in the subpolar basin.

The leading EOF in the higher diffusivity experiment (N50HIGH) explains 77 % of the variance. The space structure of the first eigenmode shows no significant differences with respect to the weakly diffusive case, although the strength of the barotropic gyres is now considerably reduced (figure 6.15,left). The time evolution of the first EOF, given by the corresponding principal component (shown in figure 6.15, right) lags the NAOI by 2 years with a 0.9 correlation index, significant at the 99 % level.

The 10 years NAO

Under low diffusivity conditions, the leading EOF (explaining 25 % of the total variance) broadly resembles the leading variability mode of the N50LOW experiment (figure 6.16,left). A major difference with respect to the latter case is the location of the centers of action, which are now placed south of the subtropical basin anticyclonic anomaly. The first principal component is dominated by an energetic 2-3 years signal, the NAO signature clearly emerging only after a 5 years low-pass filter is applied (figure 6.16, right).

In the high diffusivity experiment (N10HIGH), the dominant EOF (explaining 70 % of the total variance) shows a major difference with the high diffusivity interdecadal forcing case. The mid-latitude anticyclonic anomaly is not limited to the subtropical basin, but exhibits a northwestern lobe entirely encompassing the Labrador Sea basin (figure 6.17,left). A *hint* of this feature is also exhibited by experiment N10LOW, presenting an anticyclonic anomaly in the northern Labrador Sea. The resulting barotropic mode appears as an inter-gyre structure, consistent with the NAO wind curl pattern (positive NAO phase, shown in figure 6.2). The coherency between the

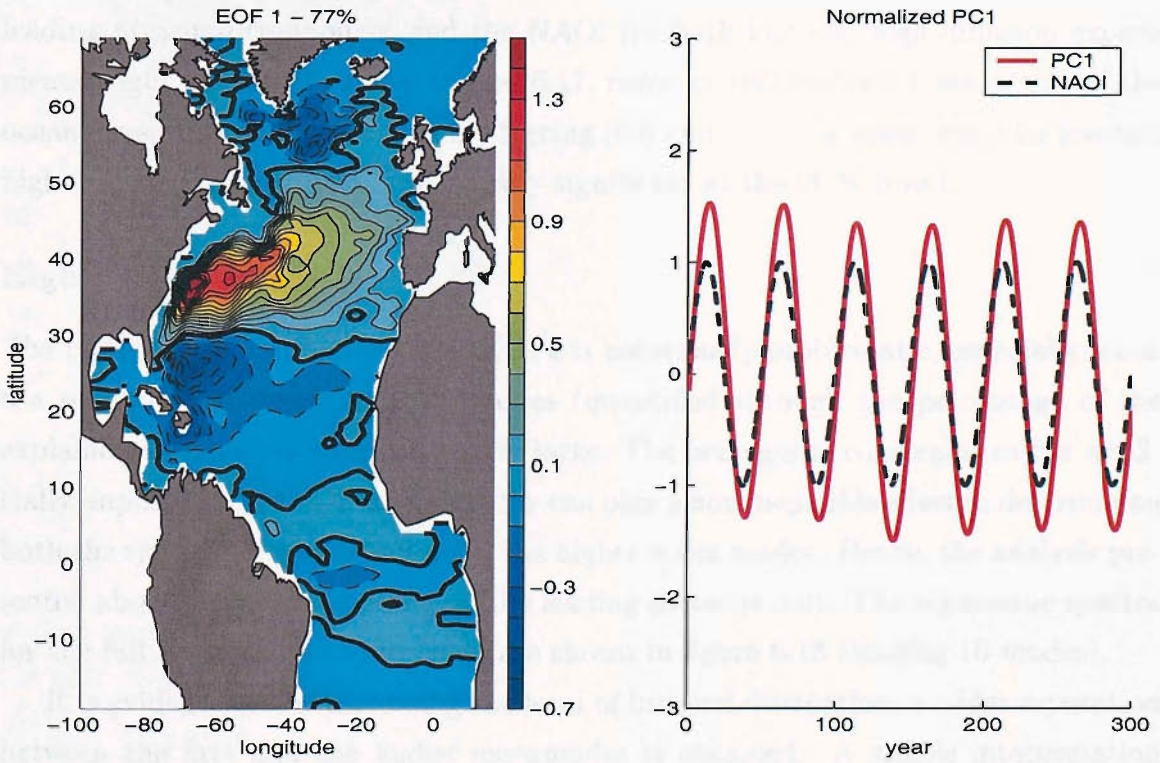

Figure 6.15: As in figure 6.14 but for experiment N50HIGH. Contour interval = 0.1 Sv. No low pass filtering has been applied to the principal component.

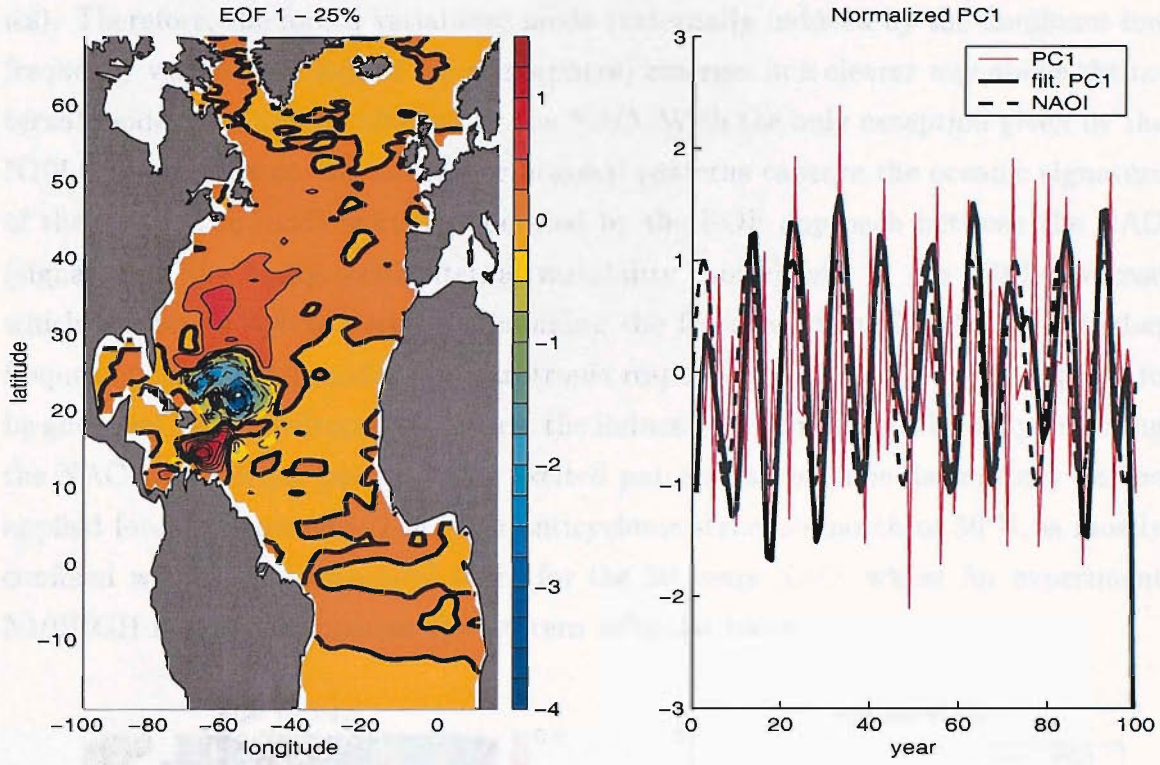

Figure 6.16: As in figure 6.14 but for experiment N10LOW. Contour interval = 0.25 Sv.

leading principal component and the NAOI for both low and high diffusion experiments (right panel in figures 6.16 and 6.17, respectively) shows a 1 year delay of the oceanic response to the atmospheric forcing (0.6 and 0.9 correlation index for low and high diffusion, respectively, statistically significant at the 99 % level).

Higher order modes

The interpretation of higher order EOFs is notoriously problematic, especially when the separation between the eigenmodes (quantified through the percentage of the explained variance) is not particularly large. The orthogonal constraint rather artificially imposed by the EOF methodology can play a non negligible effect in determining both the space and time structure of the higher order modes. Hence, the analysis presented above has been focussing on the leading patterns only. The eigenvalue spectra for the full set of NAO experiments are shown in figure 6.18 (leading 10 modes).

It is evident that by increasing the level of internal dissipation, a wider separation between the first and the higher eigenmodes is obtained. A simple interpretation of this feature can be provided. Eddy mixing has a damping effect on the system's internal variability (namely, the variability arising from the ocean's internal dynam-

ics). Therefore, the forced variability mode (externally induced by the dominant low frequency variability mode of the atmosphere) emerges in a clearer way above the internal modes not directly affected by the NAO. With the only exception given by the N10LOW experiment, the leading orthogonal patterns capture the oceanic signature of the NAO. The mode splitting operated by the EOF approach between the NAO (signal) and the background internal variability (noise) fails in the N10LOW case which exhibits a *hybrid* pattern, combining the features of the NAO with a higher frequency interannual mode. The barotropic response to the NAO forcing appears to be governed by a Sverdrup-like balance, the induced gyre circulation broadly reflecting the NAO wind torque pattern. The excited patterns show some dependency on the applied forcing frequency. The main anticyclonic structure north of 30°N, is mostly confined within the subtropical basin for the 50 years NAO, whilst for experiment N10HIGH it also encompasses the western subpolar basin.

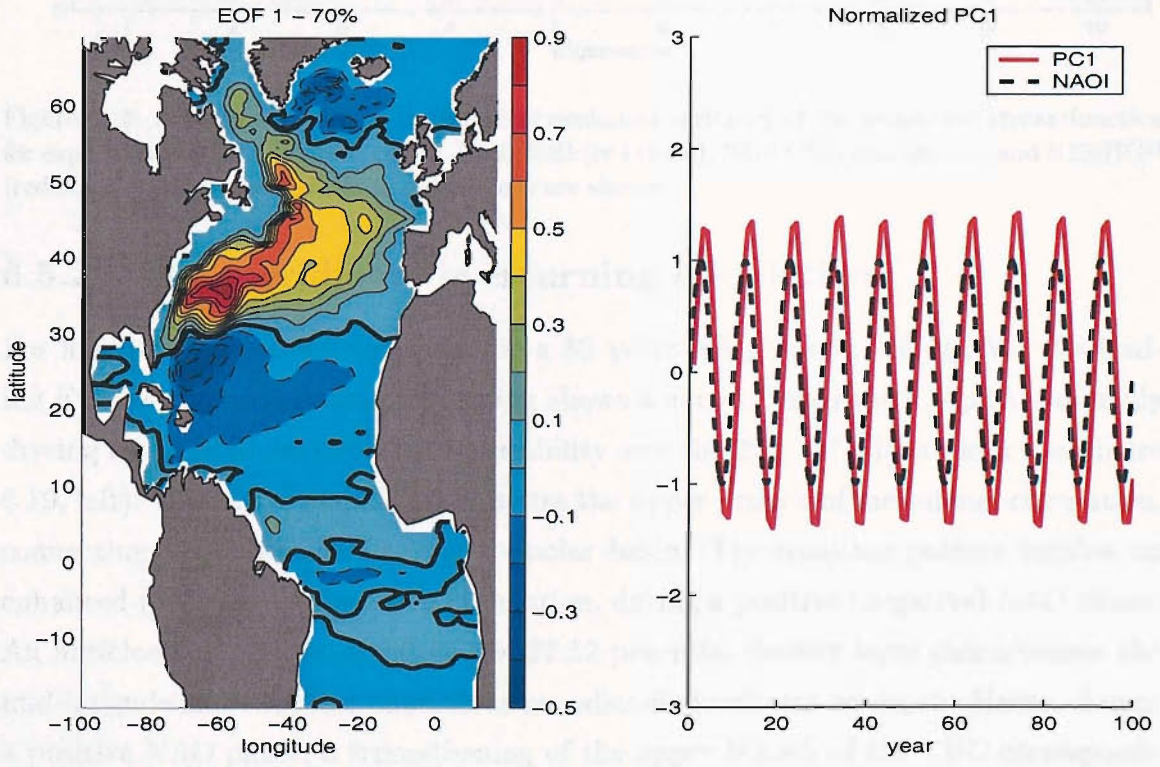

Figure 6.17: As in figure 6.14 but for experiment N10HIGH. Contour interval = 0.1 Sv.No low pass filtering has been applied to the principal component.

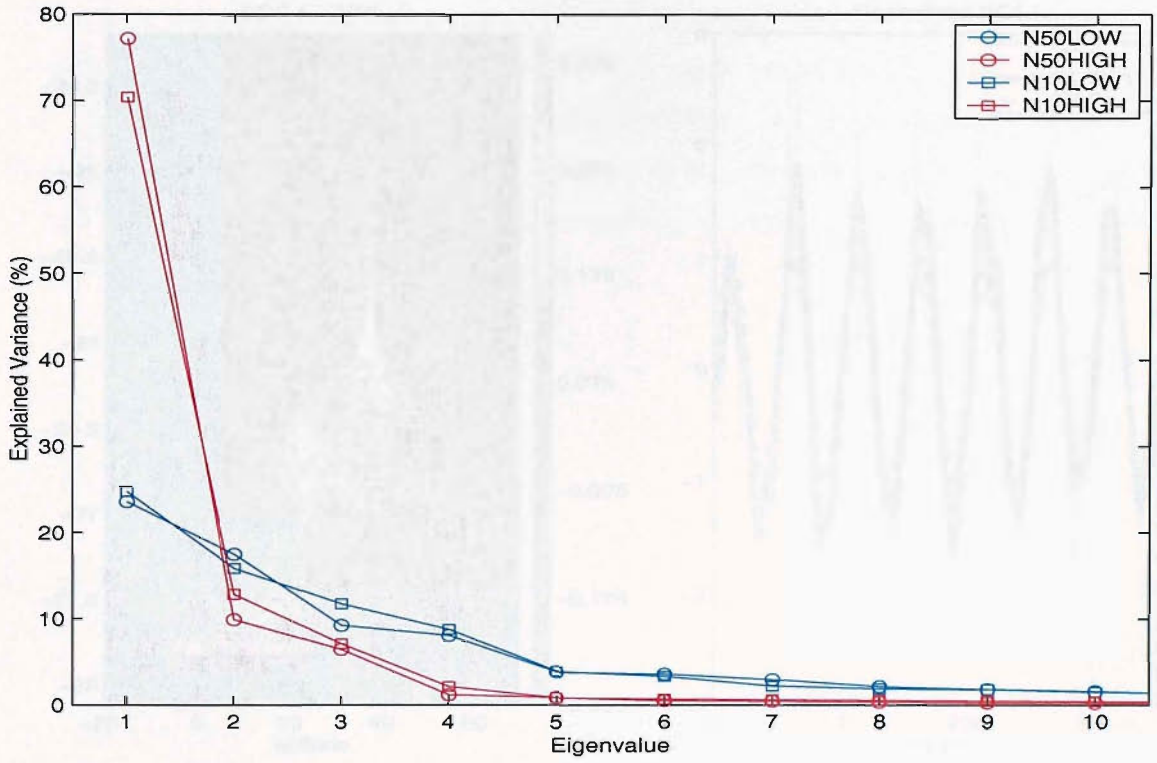

Figure 6.18: Eigenvalue spectra (in percent of explained variance) of the barotropic streamfunction for experiments N50LOW (blue circle), N50HIGH (red circle), N10LOW (blue square) and N10HIGH (red square). Only the leading 10 eigenvalues are shown.

6.5.2 The meridional overturning circulation

For low diffusivity conditions and for a 50 years NAO period (N50LOW) the leading EOF of the meridional overturning shows a surface intensified negative anomaly driving the meridional circulation variability over the $20-30°$N latitude range (figure 6.19, left). A positive anomaly dominates the upper branch of meridional circulation, connecting the subtropical to the subpolar basin. The resulting pattern implies an enhanced (decreased) interbasin circulation, during a positive (negative) NAO phase. An anticlockwise cell centered on the 27.52 potential density layer characterizes the mid-latitude and subpolar anomalous meridional circulation at depth. Hence, during a positive NAO phase, a strengthening of the upper branch of the THC corresponds to a weakening of the lower limb of the meridional circulation. The principal component of the leading eigenmode is dominated by the multidecadal NAO signature and shows an in phase response with respect to the NAOI (figure 6.19, right).
After increasing the diffusivity (N50HIGH), the space and time structure of the leading variability mode show no essential differences with respect to the weakly dissipa-

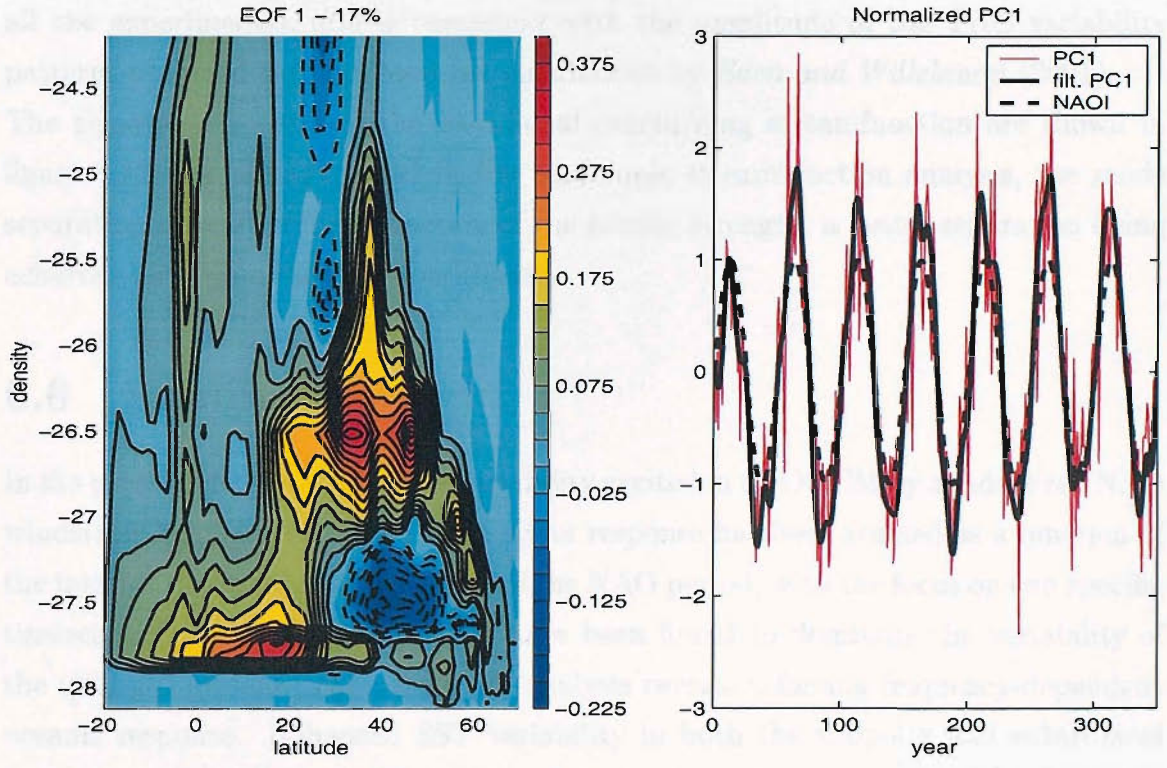

Figure 6.19: (left) Leading EOF of the annually averaged meridional overturning streamfunction (Sv; contour interval = 0.025 Sv) for experiment N50LOW. The solid (dashed) lines denote positive (negative) values. (right) Normalized leading principal component of the meridional overturning streamfunction for experiment N50LOW (red). Low pass filtered values (with a 5 years cut-off period) are also shown (black solid), along with the normalized 50 years NAOI (black dashed).

tive case, apart from the increase in the fraction of explained variance (41 %; figure 6.20). Also, the subpolar extension of the major positive anomaly appears to be stronger.

Under low diffusivity conditions and for a 10 years NAO forcing period (N10LOW) the leading EOF of the meridional overturning streamfunction (explaining 17 % of the total variance) is dominated by a dipole structure with the centers of action located on the 26.52 and 27.38 potential density layers for the positive and negative anomaly, respectively (figure 6.21, left). The dipole drives a cross-isopycnal flow occurring at 40°N. This pattern is modulated by the decadal NAO signal, as shown by the leading principal component (figure 6.21, right). No phase shift between the NAOI and the oceanic response is detected. Enhanced mixing does not induce any sensible changes in the space and time structure of the leading eigenmode (figure 6.22), apart from the percentage of explained variance, which increases to 57 %.

The strength of the anomalous meridional circulation patterns is about 0.3 Sv (for

all the experiments), and is consistent with the amplitude of the THC variability patterns obtained through hindcast simulations by *Eden and Willebrand* (2001). The eigenvalue spectra of the meridional overturning streamfunction are shown in figure 6.23. As already noted in the barotropic streamfunction analysis, the mode separation appears to be a function of the mixing strength, a better separation being achieved for high diffusivity conditions.

6.6 Summary

In the present chapter, the forced variability excited in an OGCM by an idealized NAO windstress has been described. The ocean response has been studied as a function of the internal dissipation strength and of the NAO period, with the focus on two specific timescales (10 and 50 years) which have been found to dominate the variability of the unforced system. The performed analysis reveals a forcing frequency-dependent oceanic response. Enhanced SST variability in both the subpolar and subtropical region is detected when a 50 years modulation is applied to the NAO-like pattern. However, the subtropical gyre adjusts almost istantaneously to the NAO, in contrast

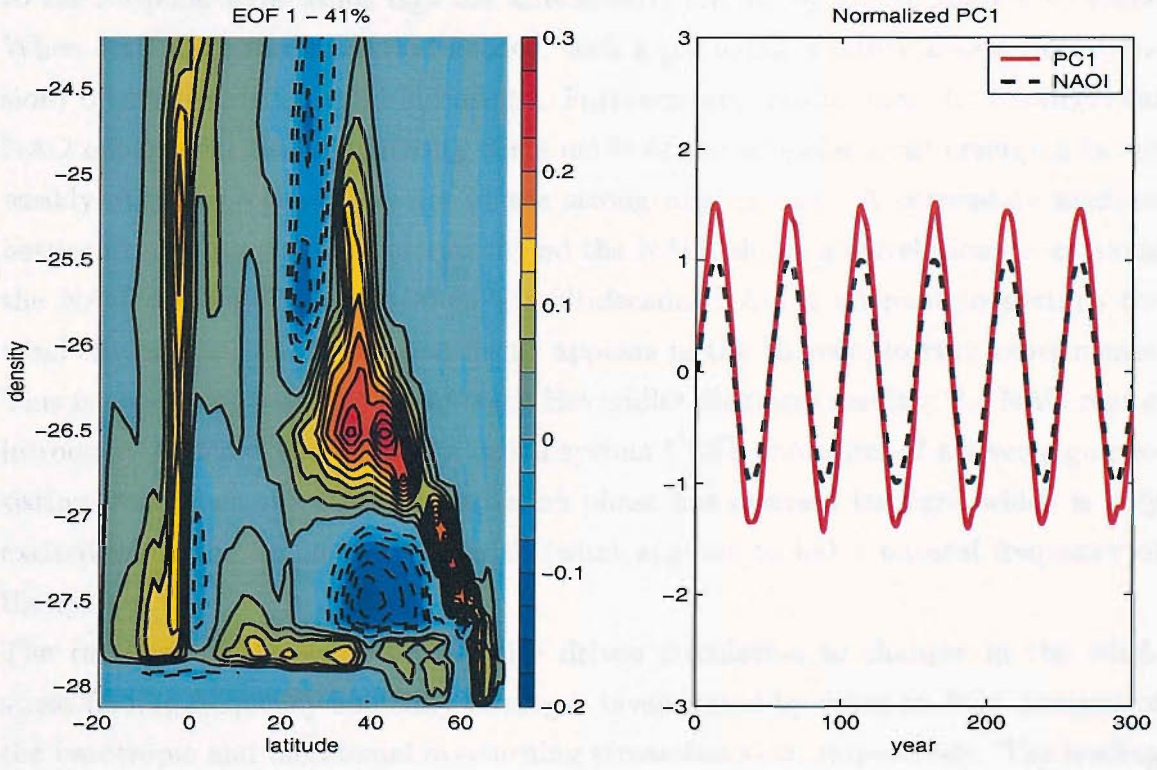

Figure 6.20: As in figure 6.19 but for experiment N50HIGH. Contour interval = 0.025 Sv

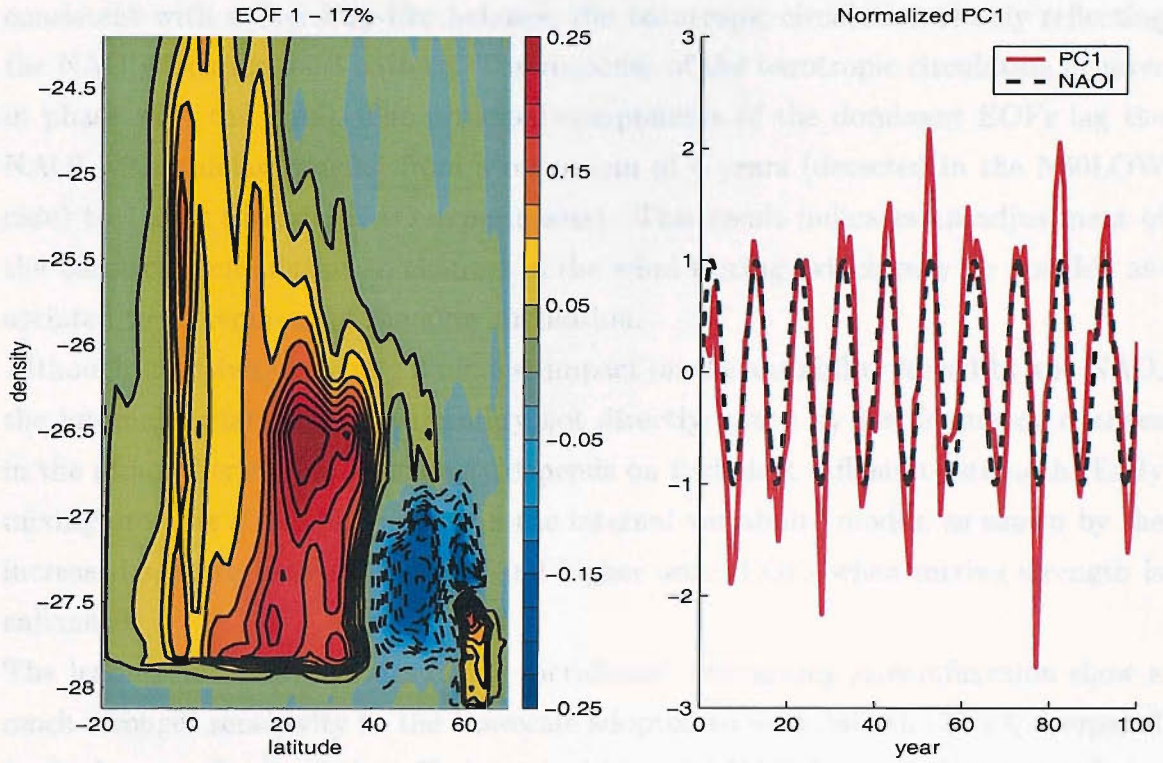

Figure 6.21: As in figure 6.19 but for experiment N10LOW. Contour interval = 0.025 Sv.

to the subpolar gyre which lags the atmospheric forcing by approximately 10 years. When a 10 years forcing period is used, such a phase-lag is either absent (low diffusion) or much reduced (high diffusion). Furthermore, results from the multidecadal NAO experiment reveal a century scale mode of the subpolar front emerging in the weakly diffusive regime, but not in the strong mixing case. A correlation analysis between the upper layer temperature and the NAOI shows a correlation decay along the NAC pathway at lag 0, when a multidecadal NAO is adopted to perturb the wind climatology. No correlation decay appears in the 10 years forcing experiments. This is consistent with the along-track Hovmüller diagrams results: the NAC region introduces a memory effect in the ocean system (SST anomalies of a given sign persisting even when the NAO perturbation phase has reversed its sign) which is only excited when the ocean is forced with (what appears to be) a natural frequency of the system.

The response of the wind and density driven circulation to changes in the wind-stress forcing frequency and eddy mixing is investigated by using an EOF analysis of the barotropic and meridional overturning streamfunction, respectively. The leading variability modes of the barotropic streamfunction show a space structure which is

consistent with a Sverdrup-like balance, the barotropic circulation closely reflecting the NAO windstress curl pattern. The response of the barotropic circulation is never in phase with the NAO. The principal components of the dominant EOFs lag the NAOI with a delay ranging from a maximum of 4 years (detected in the N50LOW case) to 1 year (decadal NAO experiments). This result indicates an adjustment of the barotropic circulation to changes in the wind forcing, which may be possibly associated to the spin-up of the gyre circulation.

Although diffusivity has only a modest impact on the variability forced by the NAO, the internal variability (i.e.,variability not directly forced by low frequency changes in the atmospheric forcing) strongly depends on turbulent diffusivity strength. Eddy mixing provides a damping effect on the internal variability modes, as shown by the increased spacing between the first and higher order EOFs when mixing strength is enhanced.

The leading variability modes of the meridional overturning streamfunction show a much stronger sensitivity to the timescale adopted to modulate the NAO, compared to the barotropic circulation. Under a multidecadal NAO forcing, a mid latitude interbasin mode is excited, in phase with the NAOI. During a positive NAO phase the

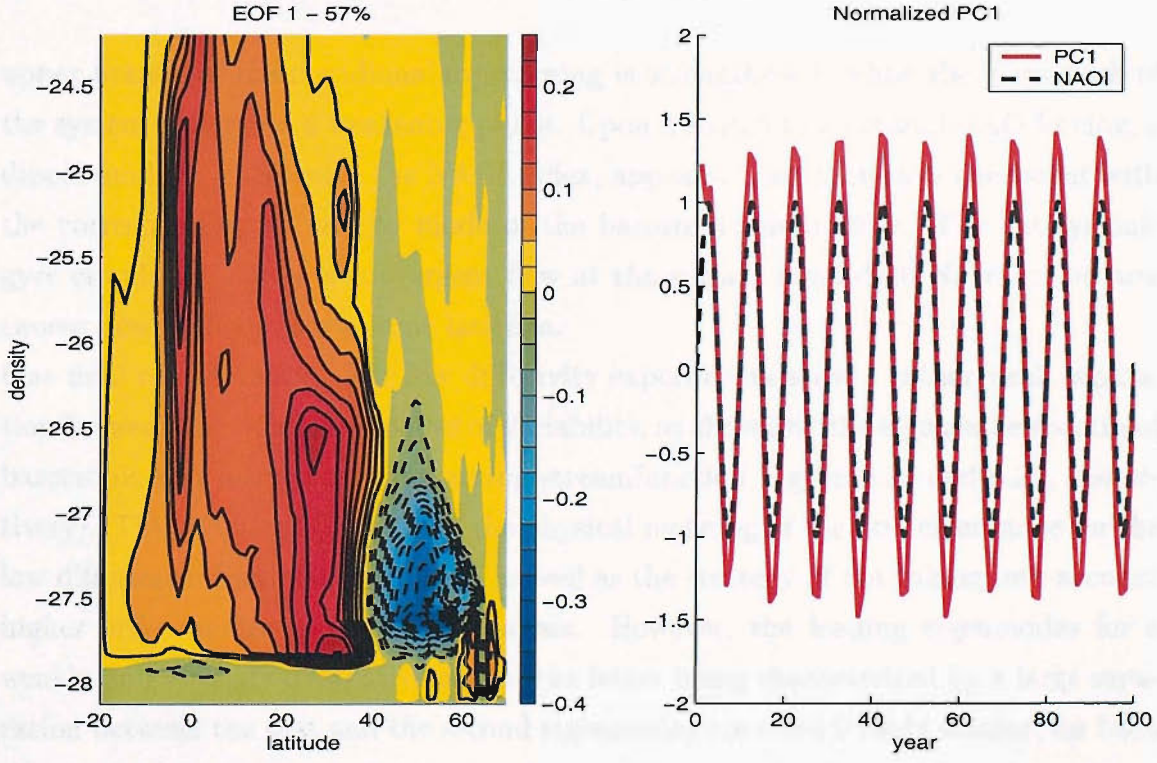

Figure 6.22: As in figure 6.19 but for experiment N10HIGH. Contour interval = 0.025 Sv.

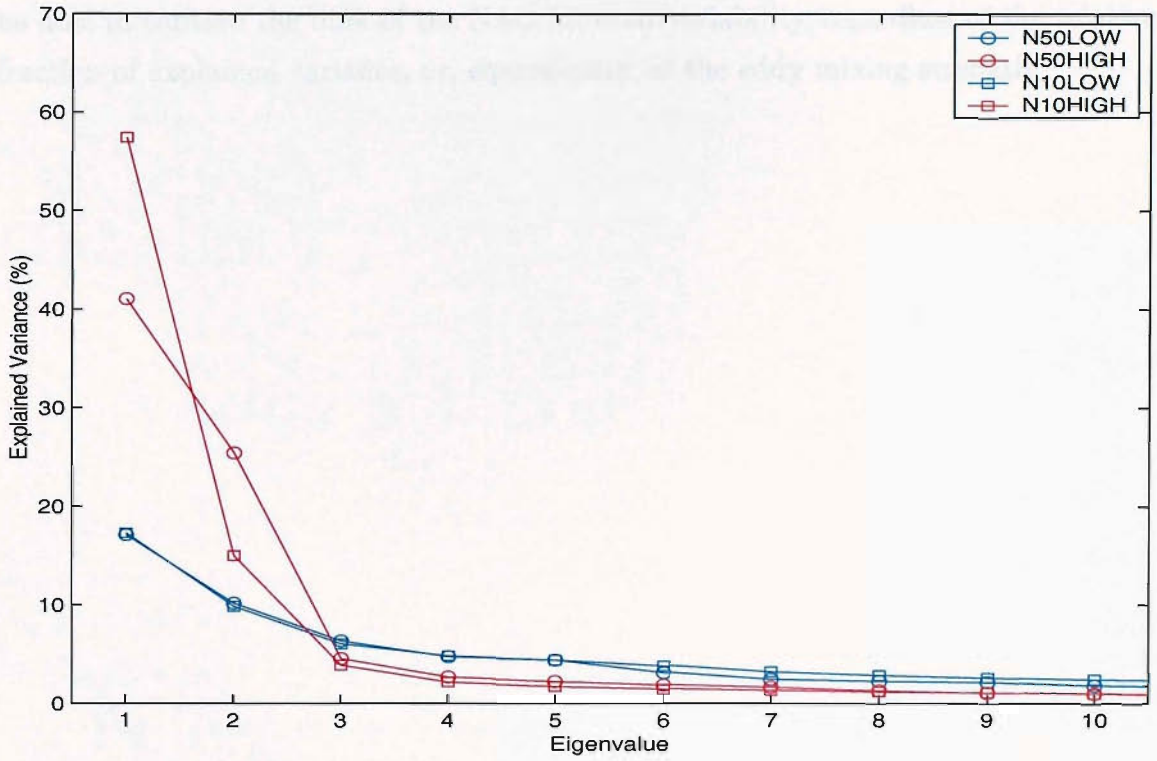

Figure 6.23: Eigenvalue spectra (in percent of explained variance) of the meridional overturning streamfunction for experiments N50LOW (blue circle), N50HIGH (red circle), N10LOW (blue square) and N10HIGH (red square). Only the leading 10 eigenvalues are shown.

upper branch of the meridional overturning is strengthened, while the lower limb of the system undergoes a weakening phase. Upon a switch to a decadal NAO forcing, a dipole mode in phase with the NAOI index, appears. This pattern is consistent with the corresponding variability mode of the barotropic circulation. The anticyclonic gyre circulation drives a convergent flow at the surface around 40°N, which in turn causes downwelling at the same latitude.

One final consideration. The low diffusivity experiments show a rather weak separation between the dominant modes of variability, as shown by the eigenvalue spectra of barotropic and meridional overturning streamfunction (figure 6.18 and 6.23, respectively). This may lead to question the physical meaning of the first eigenmode for the low diffusion subset of experiments, as well as the strategy of not taking into account higher order modes in the EOF analysis. However, the leading eigenmodes for a weakly and strongly dissipative ocean (the latter being characterised by a large separation between the first and the second eigenmode) are considerably similar, for both the spatial structure and the time evolution. Thus, the leading eigenmode seems to

be able to capture the bulk of the NAO induced variability, regardless of the relative fraction of explained variance, or, equivalently, of the eddy mixing strength.

Chapter 7

Discussion and conclusions

In the present work, the internal and forced low frequency variability in an OGCM of the North Atlantic have been investigated. Evidence has been provided that critical thresholds exist in the parameter space of the employed OGCM, setting the transition of the system from a steady state to an interdecadal oscillatory solution. In the dynamical systems theory, this feature is referred to as a Hopf bifurcation (*Drazin*, 1992).

The oscillatory mode emerges for low levels of internal dissipation and high MO. By increasing the MO, while keeping the thickness diffusivity fixed, the meridional overturning rate increases, becoming unstable. The transition occurs for a thickness diffusivity $K_{th} = 150m^2/s$, and for a meridional overturning rate exceeding 16 Sv.

This regime diagram bears strong analogies with the results of *te Raa and Dijkstra* (2002) who showed the stabilizing (destabilizing) effect of enhanced lateral (vertical) mixing on an interdecadal mode emerging in a simplified primitive equation model. Increasing the vertical diffusion produces the same strengthening effect on the meridional overturning as an increase of the MO. Hence, the experiments here described are roughly comparable to *te Raa and Dijkstra* (2002) results, although caution is needed in identifying the thickness diffusivity with lateral mixing, as the latter may induce spurious diapycnal mixing which is absent in the parameterised diffusion of thickness.

The authors identify a supercritical Hopf bifurcation for a lateral diffusion $K_h = 1670m^2/s$, the steady states being linearly stable for $K_h > 1670m^2/s$, and unstable for lower diffusivities. Although a rigorous comparison is not possible, as the two compared systems are characterized by different geometries and flow regimes (or,

equivalently, by well distinct Peclet numbers), it is worth to notice some encouraging consistency.

The stabilizing effect of the horizontal mixing on an interdecadal unstable mode of the THC has also been suggested by the experiments of *Chen and Ghil* (1995) and CVH. The existence of a narrow range of values of the meridional overturning strength, whereby the THC exhibits an unstable behavior has also been shown by *Rahmstorf* (1995), in a global ocean model coupled to a very simple atmosphere. The author identifies a critical range of the freshwater fluxes where the North Atlantic overturning enters a limit cycle with a 22 years period.

The work presented here extends that of the above mentioned authors, who have considered simplified frameworks, by considering a more realistic geometry and forcing. The existence of a Hopf bifurcation appears to be a robust feature of the oceanic dynamical system.

The extensive analysis of the interdecadal oscillatory mode exhibited by the ocean under a climatological forcing, provides some insights on the dynamics behind the system internal low frequency variability. The interplay between poleward propagating surface thermal anomalies and deep convection in the Irminger basin drives an irregular oscillation of the meridional overturning circulation, with a typical 50 years timescale. SST anomalies appear to slowly migrate along the NAC path. The periodic sign reversal of the SST anomalies in the subpolar basin, modulates the formation of LSW, which feeds the lower limb of the model THC. The timescale of the oscillation and the nature of the feedback between high-latitude density anomalies and the overturning strength, bear strong similarities with the advective-convective mechanism identified by *Greatbatch and Zhang* (1995). As in the experiments performed by *Greatbatch and Zhang* (1995), the oscillation is thermally driven, the high latitude density anomalies being modestly affected by salinity. This is essentially different from the mechanism suggested by DMS93 for the interdecadal mode in the GFDL model, where salinity is claimed to play a crucial role in driving the oscillation. The occurrence of deep convection and the consequent formation of LSW thickness anomalies in the model Irminger Sea is consistent with recent observational evidence (*Pickart et al.*, 2003), which identifies this region of the subpolar basin as a significant source of LSW.

The self sustained oscillation is maintained by two delays. The approximately decadal adjustment of the THC to changes occurring in the deep convection region, involves

the DWBC route. This result supports the slow advective mechanism of *Marotzke and Klinger* (2000) against the rapid timescale implied by the propagation of Kelvin waves as suggested by *Kawase* (1987) and, more recently, by *Johnson and Marshall* (2002).

The other fundamental delay is associated with the travel time of a density anomaly along the upper limb of the THC. The causes of the detected discrepancy between the typical velocities in the NAC, and the effective propagation speed featured by the SST anomalies, are unclear. Slow planetary waves dynamics (also invoked, among the others, by CVH and *te Raa and Dijkstra* (2002)), represent a possible alternative to mean flow advection. However, an involvement of baroclinic Rossy waves turns out to be unlikely, due to the direction of propagation and the high latitude character featured by the thermal signatures.

The ocean response to a NAO-like windstress perturbation, reveals a rather strong dependency on the specific frequency used to modulate the intensity of the anomalous windstress, while the ocean mixing strength plays a relatively minor role, mostly affecting the amplitude of the ocean response. The analysis of the SST variability, reveals that the upper ocean rapidly adjusts to decadal NAO-driven windstress changes, in contrast with the delayed response exhibited under a multidecadal NAO. The memory of the system resides in the NAC, which lags the 50 years NAO forcing by approximately 10 years, leading to thermal anomalies which persist after the NAO has reversed its sign. The subtropical gyre, on the other hand, shows an instantaneous adjustment to windstress changes (with the only exeception for experiment N10HIGH, lagging the NAO by 1 year), regardless of the specific forcing frequency.

The sign of the thermal anomalies in the upper layer is apparently consistent with a local wind forcing, driving anomalous velocities in the Ekman layer. Windstress anomalies force the isotherms to depart from the climatological position, which in turn generates the detected SST anomalies. However, Ekman dynamics can only be invoked to explain the in phase ocean response, occurring in the subtropical/GS region (with the only exception for experiment N10HIGH; see figure 6.9). Slower dynamics are needed in order to justify the delayed response in the subpolar region. The absence of propagating signals along the NAC path (figures 6.7,6.8 and 6.9) suggests that the lateral advection by the mean currents does not affect the SST variability. The absence of poleward propagating SST anomalies is strikingly in contrast with the results from experiment H01 (figure 5.3). As the NAO experiments are characterised

by a weaker MO (which in turn implies a weaker meridional overturning rate; see figure 4.3) with respect to experiment H01 (all other parameters being identical), the overturning strength appears to be essential for the propagation of thermal anomalies. *Visbeck et al.* (1998) and *Krahmann et al.* (2001) find propagation of SST anomalies along the NAC, in an OGCM of the North Atlantic. The rather coarse resolution employed by the authors (2^o by 2^o) is likely to have required high levels of dissipation in the model, which might have caused a stronger meridional overturning rate (compared to the present NAO experiments), although this information is not available in the mentioned works. There is a broad agreement between the NAO-induced SST variability diagnosed in the present work, and *Visbeck et al.* results. In particular, the detection of enhanced variance in the subpolar region and the finding of a memory effect associated with the GS extension, are both consistent with the set of results presented in this work. However, *Visbeck et al.* find a variance peak in the decadal NAO forcing frequency band, while in this study the maximum response is found under a 50 years NAO modulation. The matching between the internal variability timescale of the unforced system, and the maximum response timescale of the (NAO-)forced system, suggests that the ocean possesses a preferred variability timescale which can be externally excited by an atmosphere varying over a similar period. In *Visbeck et al.* (1998) a prior evaluation of the system internal variability (i.e., without the NAO perturbation) is missing. It is interesting to speculate that the reason why the present model and that of *Visbeck et al.* have largest responses at different NAO frequencies is that the underlying ocean models have different natural frequencies. To test such a speculation would require further numerical experimentation.

Another essential difference lies in the mechanism underlying the memory introduced in the system by the GS extension, which, as previously mentioned, *Visbeck et al.* identify in the northeastward migration of SST anomalies along the NAC path. Such a process is absent in the results presented here. A delayed meridional displacement of the subpolar front, characterised by tightly packed isotherms, appears to be a likely candidate to explain the large amplitude SST anomalies diagnosed in the NAC region. The NAC marks the boundary between the subtropical and subpolar gyres. Hence, changes in the position of the GS extension can be traced back to variations in the geometry of the double gyre structure.

The response of the wind-driven gyre circulation to decadal and multidecadal oscillations of the NAO amplitude has been inspected through an EOF analysis of the

annually averaged barotropic streamfunction. The horizontal circulation displays a Sverdrup-like linear response to the anomalous NAO wind torque. Northern latitudes are dominated by an anticyclonic anomalous gyre (during a NAO positive phase), which closely reproduces the inter-gyre gyre (IGG) postulated by *Marshall et al.* (2001) (see also figure 3 in *Visbeck et al.*, 2003). The IGG exhibits a relatively modest sensitivity to the level of dissipation in the ocean. The NAO forcing frequency, on the other hand, affects the northern boundary of the IGG in a noticeable way. Under a 10 years NAO forcing, the northernmost 0-line of the IGG encircles the Labrador basin (this is particularly evident in the high diffusivity experiment) while for a 50 years NAO period the IGG is mostly confined south of 55^{o}N. Similar variability patterns of the barotropic circulation in the North Atlantic, emerge in a hindcast experiment performed by *Eden and Willebrand* (2001). The authors force a state-of-the-art OGCM of the North Atlantic with an interannually varying wind-stress and climatological heat and freshwater fluxes. A canonical correlation analysis between the wind stress curl and the barotropic streamfunction, at lags 0 and 3 years (the atmosphere leading the ocean) reveals two distinct patterns (figure 8 in *Eden and Willebrand*, 2001). At lag zero, maximum correlation is obtained between a NAO-like wind curl pattern and a barotropic circulation pattern which closely resembles the IGG obtained in the present work under a 10 years NAO forcing (i.e., the IGG encompasses the Labrador Sea basin). The delayed response of the barotropic circulation, on the other hand, features a slightly southward shifted IGG, which reproduces the leading barotropic mode here obtained under a 50 years NAO forcing.

The coherency between the NAO and the principal components of the barotropic streamfunction also shows some consistency with *Eden and Willebrand* (2001) results. The response of the barotropic circulation exhibits a larger delay (2 and 4 years, for high and low diffusivity, respectively) when a 50 years NAO period is used, compared to the 1 year lagged response obtained under a 10 years NAO forcing. Hence, the *northward-shifted* IGG seems to reflect a weakly delayed response compared to the *southward-shifted* IGG, exhibiting a larger delay.

The presence of a delay in the anomalous barotropic streamfunction suggests that a baroclinic adjustment of the barotropic mode occurs. The coupling between the baroclinic and barotropic modes, taking place in presence of topography , leads to a lagged response of the barotropic circulation (sometimes also referred to as gyre spinup). The delay depends on the propagation timescale of the more energetic baro-

clinic mode, and it is of the order of a few years (*Anderson et al.*, 1979; *Visbeck et al.*, 2003).

The existence of a delay, particularly evident for a multidecadal NAO, is also consistent with the results from the analysis of the SST variability. This suggests the possible involvement of the barotropic circulation in the diagnosed NAC lagged response. Changes in the geometry of the subtropical/subpolar gyre boundary, forced by the anomalous IGG, cause the displacement of the NAC with respect to the climatological position, and the consequent generation of the detected surface thermal anomalies.

There is a clear mismatch between the time-lag exhibited by the leading EOF of the barotropic circulation (2-4 years), and the delay characterizing the SST in the NAC (of the order of a decade). However, caution is needed in the interpretation of the principal component. The latter describes the time evolution of the dominant barotropic mode *as a whole*, and does not exclusively capture a particular sub-structure (the IGG). Hence, the detected time lag, grossly refers to the spin up of the double gyre system, which is likely to be largely affected (but not only) by the IGG.

An EOF analysis of the meridional overturning streamfunction reveals two distinct patterns dominating the variability of the meridional overturning circulation, depending on the forcing frequency of the NAO. A dipole mode, excited by a decadal NAO forcing, and an enhanced overturning pattern, emerging under a multidecadal NAO. Both patterns display an in phase response to changes in the NAO. The dipole mode is consistent with the leading EOF of the barotropic circulation. During a positive NAO phase, the anomalous IGG circulation drives an antyclonic flow, which causes convergence and downwelling at the surface around 40°N. Convergence in the upper layer is balanced by an opposite sign flow at depth. Thus, the dipole mode describes the contribution of Ekman-driven dynamics to the meridional overturning circulation. The enhanced overturning pattern, on the other hand, shows no consistency with the anomalous IGG circulation. The anomalous overturning excited under a 50 years NAO, forces a stronger (weaker) poleward mass transport in the upper limb of the meridional circulation cell, during a positive (negative) NAO phase.

The dipole pattern bears a striking similarity with the THC canonical correlation analysis pattern (correlated at lag 0 with a positive NAO-like SLP anomaly pattern) diagnosed by *Eden and Willebrand* (2001) (figure 10c in *Eden and Willebrand*, 2001). It is worth to notice that a purely decadal NAO is capable to excite the same THC

leading variability mode obtained with a fully resolved (i.e., including all the spectral components) NAO forcing. The time series length of the interannual momentum fluxes used by *Eden and Willebrand* (2001) is clearly not sufficient to resolve longer than decadal components of the NAO signal, which may explain why the enhanced overturning pattern does not emerge from the output of the hindcast experiments.

A few concluding remarks. It has been demonstrated that a large-scale variability pattern of the troposphere can excite distinct responses in an OGCM, depending on the timescale dominating the atmospheric forcing. Hints of enhanced ocean variability, emerging under an atmospheric forcing frequency matching the internal variability frequency of the ocean, have also been found. In the North Atlantic sector, time series analyses of NAO indicators reveal that changes in the spectral signature of the NAO have occurred in the past. In particular, a progressive reddening of the NAO spectrum during the 20th century (characterised by a switch from a quasi-biennial to a quasi-decadal dominant spectral signature) has been documented by *Hurrell and van Loon* (1997). Evaluating the impact of these changes on the ocean circulation and SST patterns, may help in the interpretation of past records of oceanic variability and in estimating the effects of possible evolutions of the atmosphere on the ocean state.

In the broader context of the coupled system, the present results suggest that coupled ocean-atmosphere variability modes are more likely to arise under a primarily multi-decadal NAO forcing, as the latter is able to excite a delayed SST response, which is essential for sustaining oscillations involving both fluids.

In the performed experiments, only the effects of low frequency changes of momentum fluxes have been analysed. This study represents a first step towards a full assessment of the NAO impact on the North Atlantic Ocean variability. A complete analysis requires a twin set of forced experiments, accounting for the NAO-induced modulation of buoyancy fluxes. Moreover, the dependency of the oceanic response upon the NAO forcing frequency has been only partially tackled, and more experiments are needed, particularly in the interannual tail. These issues will be the subject of future work.

Bibliography

Anderson, D., K. Bryan, A. Gill, and R. Pacanowski, The transient response of the North Atlantic: some model studies, *Journal of Geophysical Research*, *84*, 4795–4815, 1979.

Baringer, M., and J. Price, Mixing and spreading of the mediterranean outflow, *Journal of Physical Oceanography*, *27*, 1654–1677, 1997.

Barnier, B., L. Siefridt, and P. Marchesiello, Thermal forcing for a global ocean circulation model using a three-year climatology of ECMWF analyses, *Journal of Marine Systems*, *6*, 363–380, 1995.

Bjerknes, J., Atlantic air sea interaction, *Advances in Geophysics*, *10*, 1–82, 1964.

Bleck, R., Ocean modeling in isopycnic coordinates, in *Ocean modeling and parameterisation*, edited by E.P.Chassignet and J.Verron, pp. 423–448, Kluwer Academic Publishers, 1998.

Bleck, R., An oceanic general circulation model framed in hybrid isopycnic-Cartesian coordinates, *Ocean Modelling*, *37*, 55–88, 2002.

Bleck, R., and D. Boudra, Initial testing of a numerical ocean circulation model using a hybrid (quasi-isopycnic) vertical coordinate, *Journal of Physical Oceanography*, *11*, 755–770, 1981.

Bleck, R., and D. Boudra, Wind driven spin-up in eddy resolving ocean models formulated in isopycnic and isobaric coordinates, *Journal of Geophysical Research*, *91*, 7611–7621, 1986.

Bleck, R., and L. Smith, A wind-driven isopycnic coordinate model of the North and Equatorial Atlantic Ocean. 1. Model development and supporting experiment, *Journal of Geophysical Research*, *95*, 3273–3285, 1990.

Bleck, R., H. Hanson, D. Hu, and E. Kraus, Mixed layer-thermocline interaction in a three-dimensional isopycnal coordinate model, *Journal of Physical Oceanography*, *19*, 1417–1439, 1989.

Bleck, R., C. Rooth, D. Hu, and L. Smith, Salinity-driven thermocline transients in a wind- and thermohaline-forced isopycnic coordinate model of the North Atlantic, *Journal of Physical Oceanography*, *22*, 1486–1505, 1992.

Böning, C., W. Holland, F. Bryan, G. Danabasoglu, and J. McWilliams, An overlooked problem in model simulations of the thermohaline circulation and heat transport in the Atlantic Ocean, *Journal of Climate*, *8*, 515–523, 1995.

Bryan, F., High-latitude salinity effects and interhemispheric thermohaline circulations, *Nature*, *323*, 301–304, 1986.

Bryan, F., Parameter sensitivity of primitive equation ocean general circulation model, *Journal of Physical Oceanography*, *17*, 970–985, 1987.

Bryan, K., A numerical method for the study of the circulation of the world ocean, *Journal of Computational Physics*, *4*, 347–376, 1969.

Cayan, D., Latent and sensible heat flux anomalies over the northern oceans: the connection to monthly atmospheric circulation, *Journal of Physical Oceanography*, *5*, 354–369, 1992.

Chen, F., and M. Ghil, Interdecadal variability of the thermohaline circulation and high-latitude surface fluxes, *Journal of Physical Oceanography*, *25*, 2547–2568, 1995.

Colin de Verdière, A., On mean flow instabilities within planetary geostrophic equations, *Journal of Physical Oceanography*, *16*, 1981–1984, 1986.

Colin de Verdière, A., and T. Huck, Baroclinic instability: an oceanic wavemaker for interdecadal variability, *Journal of Physical Oceanography*, *29*, 893–910, 1999.

Cook, E., R. D'Arrigo, and K. Briffa, A reconstruction of the North Atlantic Oscillation using tree-ring chronologies from North America and Europe, *The Holocene*, *8*, 9–17, 1998.

Cox, M., A primitive equation, three-dimensional model of the ocean, *GFDL Ocean Group Technical Report No. 1*, 1984.

Cullen, H., R. D'Arrigo, E. Cook, and M. Mann, Multiproxy reconstructions of the North Atlantic Oscillation, *Paleoceanography*, *16*, 27–39, 2001.

Curry, R., and M. McCartney, Ocean gyre circulation changes associated with the North Atlantic Oscillation, *Journal of Physical Oceanography*, *31*, 3374–3400, 2001.

Curry, R., M. McCartney, and T. Joyce, Oceanic transport of subpolar climate signals to mid-depth subtropical waters, *Nature*, *391*, 575–577, 1998.

Czaja, A., A. Robertson, and T. Huck, The role of Atlantic ocean-atmosphere coupling in affecting North Atlantic Oscillation variability, in *The North Atlantic Oscillation: climatic significance and environmental impact*, edited by J. Hurrell, Y. Kushnir, G. Ottersen, and M. Visbeck, American Geophysical Union, Geophysical Monograph 134, 2003.

Delworth, T., and R. Greatbatch, Multidecadal thermohaline circulation variability driven by atmospheric surface flux forcing, *Journal of Climate*, *13*, 1481–1495, 2000.

Delworth, T., and M. Mann, Observed and simulated multidecadal variability in the northern hemisphere, *Climate Dynamics*, *16*, 661–676, 2000.

Delworth, T., S. Manabe, and R. Stouffer, Interdecadal variations of the thermohaline circulation in a coupled ocean-atmosphere model, *Journal of Climate*, *6*, 1993–2011, 1993.

Deser, C., and M. Blackmon, Surface climate variations over the North Atlantic ocean during winter: 1900-1989, *Journal of Climate*, *6*, 1743–1753, 1993.

Dickson, R., J. Lazier, J. Meincke, P. Rhines, and J. Swift, Long-term coordinated changes in the convective activity of the North Atlantic, *prog*, *38*, 241–295, 1996.

Drazin, P. G., *Nonlinear Systems*, Cambridge Texts in Applied Mathematics, Cambridge University Press, 1992.

DYNAMO Group, Final Scientific Report, *Berichte aus dem Institut für Meereskunde an der Universitat Kiel, Technical Report No. 294*, 1997.

Eden, C., and T. Jung, North Atlantic interdecadal variability: oceanic response to the North Atlantic Oscillation, *Journal of Climate*, *14*, 676–691, 2001.

Eden, C., and J. Willebrand, Mechanism of interannual to decadal variability of the North Atlantic circulation, *Journal of Climate*, *14*, 2266–2280, 2001.

Frankignoul, C., and K. Hasselmann, Stochastic climate models: Part II. Application to sea-surface temperature variability and thermocline variability, *Tellus*, *29*, 289–305, 1977.

Gent, P., and J. McWilliams, Isopycnal mixing in ocean circulation models, *Journal of Physical Oceanography*, *20*, 150–155, 1990.

Goodman, J., and J. Marshall, A model of decadal middle-latitude atmosphere-ocean coupled modes, *Journal of Climate*, *12*, 621–641, 1999.

Greatbatch, R., and K. Peterson, An interdecadal oscillation in an idealized ocean basin forced by constant heat flux, *Journal of Geophysical Research*, *101*, 20,467–20,482, 1996.

Greatbatch, R., and S. Zhang, An interdecadal oscillation in an idealized ocean basin forced by constant heat flux, *Journal of Climate*, *8*, 81–91, 1995.

Greatbatch, R., K. Peterson, and H. Roth, Interdecadal variability in a coarse resolution model with north atlantic bottom topography, *Tech. rep.*, Dalhousie University, Halifax, Canada, 1997.

Griffies, S., and E. Tzipermann, A linear thermohaline oscillator driven by stochastic atmospheric forcing, *Journal of Climate*, *8*, 2440–2453, 1995.

Häkkinen, S., Variability of the simulated meridional heat transport in the North Atlantic for the period 1951-1993, *Journal of Geophysical Research*, *104*, 10,991–11,007, 1999.

Haney, R., Surface thermal boundary condition for ocean circulation models, *Journal of Physical Oceanography*, *1*, 156–167, 1971.

Hansen, D., and H. Bezdek, On the nature of decadal anomalies in North Atlantic sea surface temperature, *Journal of Geophysical Research*, *101*, 8749–8758, 1996.

Hasselmann, K., Stochastic climate models: Part I. Theory, *Tellus*, *28*, 473–485, 1976.

Houghton, R., Subsurface quasi-decadal fluctuations in the North Atlantic, *Journal of Climate*, *9*, 1363–1373, 1996.

Huang, R., and R. Chou, Parameter sensitivity study of the saline circulation, *Climate Dynamics*, *9*, 391–409, 1994.

Huck, T., A. Colin de Verdière, and A. Weaver, Interdecadal variability of the thermohaline circulation in box-ocean models forced by fixed surface fluxes, *Journal of Physical Oceanography*, *29*, 865–892, 1999.

Huck, T., G. Vallis, and A. Colin de Verdière, On the robustness of the interdecadal modes of the thermohaline circulation, *Journal of Climate*, *14*, 940–963, 2001.

Hurrell, J., Decadal trends in the North Atlantic Oscillation: Regional temperatures and precipitation, *Science*, *269*, 676–679, 1995.

Hurrell, J., and H. van Loon, Decadal variations in climate associated with the North Atlantic Oscillation, *Climatic Change*, *36*, 301–326, 1997.

Iselin, C., The influence of vertical and lateral turbulence on the characteristics of the waters at mid-depths, *EOS, Trans. AGU*, *20*, 414–417, 1939.

Jia, Y., Formation of an azores current due to mediterranean overflow in a modeling study of the north atlantic, *Journal of Physical Oceanography*, *30*, 2342–2358, 2000.

Johnson, H., and D. Marshall, A theory for the surface Atlantic response to thermohaline variability, *Journal of Physical Oceanography*, *32*, 1121–1132, 2002.

Joyce, T., C. Deser, and M. Spall, The relation between decadal variability of subtropical mode water and the North Atlantic Oscillation, *Journal of Climate*, *13*, 2550–2569, 2000.

Kawase, M., Establishment of deep ocean circulation driven by deep-water production, *Journal of Physical Oceanography*, *17*, 2294–2317, 1987.

Killworth, P., Time interpolation of forcing fields in ocean models, *Journal of Physical Oceanography*, *26*, 136–143, 1996.

Killworth, P., D. Chelton, and R. de Szoeke, The speed of observed and theoretical long extratropical planetary waves, *Journal of Physical Oceanography*, *27*, 1946–1966, 1997.

Kondo, J., Air-sea bulk transfer coefficients in diabatic conditions, *Boundary-Layer Meteorology*, *9*, 91–112, 1975.

Krahmann, G., M. Visbeck, and G. Reverdin, Formation and propagation of temperature anomalies along the North Atlantic Current, *Journal of Physical Oceanography*, *31*, 1287–1303, 2001.

Kraus, E., and J. Turner, A one-dimensional model of the seasonal thermocline: II. The general theory and its consequences, *Tellus*, *19*, 98–106, 1967.

Kushnir, Y., Interdecadal variations in north atlantic sea surface temperature associated and associated atmospheric conditions, *Journal of Climate*, *7*, 141–157, 1994.

Kushnir, Y., W. Robinson, I. Blade, N. Hall, S. Peng, and R. Sutton, Atmospheric GCM response to extratropical SST anomalies: Synthesis and evaluation, *Journal of Climate*, *15*, 2233–2256, 2002.

Latif, M., and T. Barnett, Causes of decadal climate variability over the North Pacific and North America, *Science*, *266*, 634–637, 1994.

Levitus, S., Climatological Atlas of the World Ocean, *NOAA Professional Paper*, *13*, 173, 1982.

Levitus, S., Interpentadal variability of temperature and salinity at intermediate depths of the North Atlantic ocean, 1970-1974 versus 1955-1959, *Journal of Geophysical Research*, *94*, 6091–6131, 1989.

Mann, M., R. Bradley, and M. Hughes, Global-scale temperature patterns and climate forcing over the past six centuries, *Nature*, *392*, 779–787, 1998.

Marotzke, J., Influence of convective adjustment on the stability of the thermohaline circulation, *Journal of Physical Oceanography*, *21*, 903–907, 1991.

Marotzke, J., Boundary mixing and the dynamics of three-dimensional thermohaline circulation, *Journal of Physical Oceanography*, *27*, 1713–1728, 1997.

Marotzke, J., and B. Klinger, The dynamics of equatorially asymmetric thermohaline circulation, *Journal of Physical Oceanography*, *30*, 955–970, 2000.

Marotzke, J., and J. Willebrand, Multiple equilibria of the global thermohaline circulation, *Journal of Physical Oceanography*, *21*, 1372–1385, 1991.

Marshall, J., H. Johnson, and J. Goodman, A study of the interaction of the North Atlantic Oscillation with ocean circulation, *Journal of Climate*, *14*, 1399–1421, 2001.

Mesinger, F., and A. Arakawa, Numerical methods used in atmospheric models, *GARP Publications Series*, *17*, 64 pp., 1976.

Molinari, R., D. Meyer, J. Festa, and H. Bedzek, Multiyear variability in the near-surface temperature structure of the midlatitude western North Atlantic Ocean, *Journal of Geophysical Research*, *102*, 3267–3278, 1997.

Montgomery, R., The present evidence on the importance of lateral mixing in the ocean, *Bull. Amer. Meteor. Soc.*, *21*, 87–94, 1940.

Pickart, R., F. Straneo, and G. Moore, Is Labrador Sea Water formed in the Irminger Basin?, *Deep-Sea Research*, *50*, 23–52, 2003.

Preisendorfer, R., *Principal component analysis in meteorology and oceanography*, Elsevier, Amsterdam, 1988.

Rahmstorf, S., Bifurcations of the atlantic thermohaline circulation in response to changes in the hydrological cycle, *Nature*, *378*, 145–149, 1995.

Rahmstorf, S., Decadal variability of the the thermohaline ocean circulation, in *Beyond El Niño: decadal and interdecadal variability*, edited by A. Navarra, Springer-Verlag, 1999.

Redi, M., Oceanic isopycnal mixing by coordinate rotation, *Journal of Physical Oceanography*, *12*, 1154–1158, 1982.

Rodwell, M., D. Rowell, and C. Folland, Oceanic forcing of the wintertime north atlantic oscillation and european climate, *Nature*, *398*, 320–323, 1999.

Römmich, D., and C. Wunsch, Two transatlantic sections: Meridional circulation and heat flux in the subtropical North Atlantic, *Deep-Sea Research*, *33*, 619–664, 1985.

Saravanan, R., and J. McWilliams, Stochasticity and spatial resonance in interdecadal climate fluctuations, *Journal of Climate*, *10*, 2299–2320, 1997.

Saravanan, R., and J. McWilliams, Advective ocean-atmosphere interaction: an analytical stochastic model with implications for decadal variability, *Journal of Climate*, *11*, 165–188, 1998.

Saravanan, R., G. Danabasoglu, S. Doney, and J. McWilliams, Decadal variability and predictability in the midlatitude ocean-atmosphere system, *Journal of Climate*, *13*, 1073–1097, 2000.

Selten, F., R. Haarsma, and J. Opsteegh, On the mechanism of North Atlantic decadal variability, *Journal of Climate*, *12*, 1956–1973, 1999.

Stommel, H., Determination of water mass properties of water pumped down from the Ekman layer to the geostrophic flow below, *Proc. Natl. Acad. Sci. USA*, *76*, 3051–3055, 1979.

Stratton, R. A., A high resolution AMIP run using the Hadley Centre model HadAM2b, *Tech. rep.*, Met. Office, Bracknell, UK, 1996, clim. Res. Tech. Note 77.

Sutton, R., and M. Allen, Decadal predictability of North Atlantic sea surface temperature and climate, *Nature*, *388*, 563–567, 1997.

Taylor, A., and J. Stephens, The North Atlantic Oscillation and the latitude of the Gulf Stream, *Tellus*, *50A*, 134–142, 1998.

te Raa, L., and H. Dijkstra, Instability of the thermohaline circulation on interdecadal time scales, *Journal of Physical Oceanography*, *32*, 138–160, 2002.

Tourre, Y., B. Rajagopalan, and Y. Kushnir, Dominant patterns of climate variability in the atlantic over the last 136 years, *Journal of Climate*, *12*, 2285–2299, 1999.

Trenberth, K., and A. Solomon, The global heat balance: heat transport in the atmosphere and ocean, *Climate Dynamics*, *10*, 107–134, 1994.

Veronis, G., The role of models in tracer studies, in *Numerical models of the ocean circulation*, pp. 133–146, National Academy of Sciences, 1975.

Visbeck, M., H. Cullen, G. Krahmann, and N. Naik, An ocean model's response to north atlantic oscillation-like wind forcing, *Geophysical Research Letters*, *25*, 4521–4524, 1998.

Visbeck, M., E. Chassignet, R. Curry, T. Delworth, R. Dickson, and G. Krahmann, The ocean's response to North Atlantic Oscillation variability, in *The North Atlantic Oscillation: climatic significance and environmental impact*, edited by J. Hurrell, Y. Kushnir, G. Ottersen, and M. Visbeck, vol. Geophysical Monograph 134, American Geophysical Union, 2003.

Walker, G., and E. Bliss, World Weather V, *Mem. Roy. Meteor. Soc.*, *4*, 53–84, 1932.

Wallace, J., and D. Gutzler, Teleconnections in the geopotential height field during the Northern Hemisphere winter, *Monthly Weather Review*, *109*, 784–812, 1981.

Weaver, A., Millennial timescale variability in ocean/climate models, in *Mechanisms of global climate change at millennial time scales*, edited by R. Webb, P. Clark, and L. Keigwin, American Geophysical Union, Geophysical Monograph 112, 1999.

Weaver, A., and E. Sarachik, Evidence for decadal variability in an ocean general circulation model: an advective mechanism, *Atmosphere-Ocean*, *29*, 197–231, 1991a.

Weaver, A., and E. Sarachik, The role of mixed boundary conditions in numerical models of the ocean's climate, *Journal of Physical Oceanography*, *21*, 1470–1493, 1991b.

Weaver, A., and S. Valcke, On the variability of the thermohaline circulation in the gfdl coupled model, *Journal of Climate*, *11*, 759–767, 1998.

Weaver, A., E. Sarachik, and J. Marotzke, Freshwater flux forcing of decadal and interdecadal oceanic variability, *Nature*, *353*, 836–838, 1991.

Weaver, A., J. Marotzke, P. Cummins, and E. Sarachik, Stability and variability of the thermohaline circulation, *Journal of Physical Oceanography*, *22*, 39–60, 1993.

Welander, P., On the oscillatory instability of a differentially heated fluid loop, *Journal of Fluid Mechanics*, *29*, 17 30, 1967.

Welander, P., Thermohaline effects in the ocean circulation and related simple models, in *Large-scale transport processes in oceans and atmosphere*, edited by J.Willebrand and D. Anderson, Reidel, 1986.

Weng, W., and J. Neelin, On the role of ocean-atmosphere interaction in midlatitude interdecadal variability, *Geophysical Research Letters*, *25*, 167–170, 1998.

Winton, M., The role of horizontal boundaries in parameter sensitivity and decadal-scale variability of coarse-resolution ocean general circulation models, *Journal of Physical Oceanography*, *26*, 289–304, 1996.

Winton, M., The damping effect of bottom topography on internal decadal-scale oscillations of the thermohaline circulation, *Journal of Physical Oceanography*, *27*, 203–208, 1997.

Wüst, G., On the vertical circulation of the Mediterranean Sea, *Journal of Geophysical Research*, *66*, 3261–3271, 1961.

Yin, F., and E. Sarachik, Interdecadal thermohaline oscillations in a sector ocean general circulation model: advective and convective processes, *Journal of Physical Oceanography*, *25*, 2465–2484, 1995.

Zalesak, S., Fully multidimensional flux-corrected transport algorithms for fluids, *Journal of Computational Physics*, *31*, 335–362, 1979.

Zhang, J., R. Schmitt, and R. Huang, The relative influence of diapycnal mixing and hydrologic forcing on the stability of the thermohaline circulation, *Journal of Physical Oceanography*, *29*, 1096–1108, 1999.